UDK 62

MACHINERY & ENERGETICS

Publisher:
National University of Life and Environmental Sciences of Ukraine

Year of foundation: 2010
Frequency of issue: Four times per year

Recommended for printing and distribution
via the Internet by the Academic Council
of National University of Life and Environmental Sciences of Ukraine
(Minutes No. 9 of February 26, 2026)

State Registration:
Media identifier R30-02298.
Decision of the National Council
of Television and Radio Broadcasting of Ukraine
No. 1795, Minutes No. 31, dated 21.12.2023.

The journal is included in the list of Professional Scientific Publications of Ukraine
Category "B". Branch of sciences – Technical.
Specialties: 0715 – Mechanics and Metal Trades, 0716 – Motor Vehicles, Ships and Aircraft,
0713 – Electricity and Energy, 0714 – Electronics and Automation
(Order of the Ministry of Education and Science of Ukraine of December 23, 2025, No. 1693)

The journal is presented international scientometric databases, repositories
and scientific systems:
Google Scholar, Professional Publications of Ukraine, Vernadsky National Library of Ukraine,
BASE, J-Gate, Dimensions, Cambridge University Library, Leipzig University Library,
European University Institute, SOLO - Search Oxford Libraries Online, University of Hull Library,
University of Oslo Library, EBSCO, UCSB Library, Ulrichsweb Global Serials Directory,
OUCI (Open Ukrainian Citation Index), WorldCat, Litmaps, CABI

Editors office address:
National University of Life and Environmental Sciences of Ukraine
03041, 15 Heroiv Oborony, Kyiv, Ukraine
Tel.: +38(044)-258-42-63
E-mail: me@technicalscience.com.ua
https://technicalscience.com.ua/en

УДК 62

ТЕХНІКА ТА ЕНЕРГЕТИКА

Видавець:
Національний університет біоресурсів і природокористування України

Рік заснування: 2010
Періодичність випуску: 4 рази на рік

Рекомендовано до друку та поширення
через мережу Інтернет Вченою радою
Національного університету біоресурсів і природокористування України
(протокол № 9 від 26 лютого 2026 р.)

Державна реєстрація:
Ідентифікатор медіа R30-02298.
Рішення Національної ради України
з питань телебачення і радіомовлення
№ 1795, протокол № 31 від 21.12.2023 р.

Журнал входить до переліку наукових фахових видань України

Категорія «Б». Галузь наук – Технічні.
Спеціальності: 131 – «Прикладна механіка», 133 – «Галузеве машинобудування»,
141 – «Електроенергетика, електротехніка та електромеханіка»,
174 – «Автоматизація, комп'ютерно-інтегровані технології та робототехніка»
(Наказ Міністерства освіти і науки України від 23 грудня 2025 року № 1693)

Журнал представлено у міжнародних наукометричних базах даних,
репозитаріях та пошукових системах:
Google Scholar, Фахові видання України, Національна бібліотека України імені
В. І. Вернадського, BASE, J-Gate, Dimensions, Cambridge University Library,
Leipzig University Library, European University Institute, SOLO - Search Oxford Libraries Online,
University of Hull Library, University of Oslo Library, EBSCO, UCSB Library, Ulrichsweb Global
Serials Directory, OUCI (Open Ukrainian Citation Index), WorldCat, Litmaps, CABI

Адреса редакції:
Національний університет біоресурсів і природокористування України
03041, вул. Героїв Оборони, 15, м. Київ, Україна
Тел.: +38(044)-258-42-63
E-mail: me@technicalscience.com.ua
https://technicalscience.com.ua/uk

Editorial Board

CONTENTS

ЗМІСТ

Machinery & Energetics
Vol. 17, No. 1. 2026

Journal homepage:
https://technicalscience.com.ua/en

UDC 631.362:004.94
DOI: 10.31548/machinery/1.2026.09

ISSN 2663-1334
e-ISSN 2663-1342

Elchyn Aliiev*
Doctor of Technical Sciences, Senior Researcher
Dnipro State Agrarian and Economic University
49600, 25 Serhii Efremov Str., Dnipro, Ukraine
https://orcid.org/0000-0003-4006-8803

Olha Aliieva
PhD in Agricultural Sciences
Institute of Oilseed Crops of the National Academy of Agrarian Sciences of Ukraine
69055, 1 Institutska Str., Soniachne, Zaporizhzhia region, Ukraine
https://orcid.org/0000-0002-2766-7548

Petro Bezverkhniy
PhD in Technical Sciences
Association of Farm Enterprises "Olvia"
74000, Vysokopillya village, Beryslav district, Kherson region, Ukraine
https://orcid.org/0009-0000-0368-7870

Pavlo Luts
PhD in Technical Sciences
Vinnytsia National Agrarian University
21008, 3 Sonyachna Str., Vinnytsia, Ukraine
https://orcid.org/0000-0002-3776-8940

Simulation of an improved seed delivery system for a pneumatic grain seeder

Abstract. The objective of this research was to enhance the precision of seed placement in the John Deere pneumatic planter by improving the design of its seed delivery system within the seeding section. The upgraded seeding section incorporated several key components: an upper and lower seed sensor, a seed retarder composed of a perforated cylinder with holes, upper and lower narrowing nozzles, a cylindrical shutter with a rigidly mounted curved toothed rack, and a servo drive with a gear wheel. These modifications aimed to improve seed distribution uniformity and optimise planting accuracy. Numerical simulations of the seed retarder, conducted using the Simcenter Star-CCM+ software package, allowed for the visualisation of both seed movement and airflow dynamics within the working area of the retarder. Regression equations of the second order were formulated based on numerical simulations and data processing in the Wolfram Cloud software package. These equations, refined by removing insignificant coefficients in accordance with the Student's t-test, described the dependencies of key parameters: the air velocity at the seed retarder's outlet (V_a^{out}), the seed velocity at the outlet (V_p^{out}), and the seed rate change coefficient (η) as functions of the inlet air velocity (V_a^{in}) and the ratio of the outlet area to the inlet area (ε). According to agronomic standards, the permissible seed rate deviation should not exceed 1%. Comparative numerical simulations were performed for both the standard and modified designs of the John Deere 90 Series pneumatic seeder's seeding section. The results indicated that the improved design yielded superior performance, ensuring more uniform seed placement. The spacing between seeds in the modified version ranged from 0.0404 m to 0.0493 m, with a coefficient of variation of 0.223, corresponding to an average spacing of

Article's History: Received: 17.10.2025; Revised: 22.01.2026; Accepted: 26.02.2026; Published: 30.03.2026.

Suggested Citation:
Aliiev, E., Aliieva, O., Bezverkhniy, P., & Luts, P. (2026). Simulation of an improved seed delivery system for a pneumatic grain seeder. *Machinery & Energetics,* 17(1), 9-19. doi: 10.31548/machinery/1.2026.09.

*Corresponding author

0.0448 ± 0.004 m. These findings confirmed that the enhanced seeding section meets the required precision standards for optimal seeding accuracy, leading to improved crop establishment and yield potential. The research results can be used for further optimisation of pneumatic seeders to improve seeding accuracy and reduce yield losses

Keywords: retarder; parameters; sowing accuracy; speed; air flow

INTRODUCTION

Optimisation of agricultural machinery helps preserve soil structure, enhancing aeration and water permeability, which is essential for maintaining soil fertility. Bionic colters, designed based on natural analogs, minimise soil erosion and contribute to sustainable agricultural practices. By tailoring the design to different soil types, these colters can be used more effectively in various agro-climatic conditions. Implementing such advanced technologies in farming not only increases productivity but also reduces environmental impact, promoting more sustainable and eco-friendly agricultural practices.

To achieve these goals, new machine designs are being developed that take into account the requirements for precision, multifunctionality, energy efficiency, and structural durability. The study by D. Xiong *et al.* (2021) focused specifically on seed delivery systems in universal precision pneumatic planters, as existing systems require further refinement. Many pneumatic planters struggle to retain seeds in the seedbed, particularly under no-till, strip-till, or mini-till conditions. This issue becomes even more pronounced when operating at high speeds, with shallower seeding depths on compacted or harder soils. A closer examination of the key issues related to the seeding section of this type of planter is warranted, with possible solutions being explored based on both practical experience. According to the studies by K. Li *et al.* (2023), the precision of seeding in a pneumatic planter is primarily determined by the process of seed movement from the metering device to the point where they are deposited into the furrow created by the opener in the soil.

Seeds, having high initial velocity, travel a relatively long distance through the seed tube and the seed boot channel. Previous work by M. Wei *et al.* (2022) showed that airflow-assisted seed delivery can reduce variation in plant spacing caused by collisions with seed tube walls, but accelerated seeds may still bounce and lead to uneven spacing. Specifically, in precision seeding devices based on airflow-assisted seed delivery, seeds were observed to contact surfaces and bounce, resulting in uneven plant spacing at higher speeds, demonstrating that controlling seed velocity and trajectory remained an open challenge. Research by H. Tang *et al.* (2023) has also highlighted issues in pneumatic high-speed seed metering for maize, where traditional pneumatic systems, while effective for carrying seeds, did not fully prevent irregularities in seeding quality as operating speeds increased, indicating limitations in controlling seed placement under high dynamic conditions.

Developments by H.-T. Lin & Y.-H. Lee (2023) in precision pneumatic seeding devices, such as a precision pneumatic plug tray seeder with real-time trajectory tracking, addressed trajectory control via adaptive feedback systems, improving single-seeding accuracy but still focusing on tray systems rather than in-row transport dynamics in field planters. Seeding uniformity was determined along three spatial coordinates: the distance between seeds along the planting row, the seed dispersion perpendicular to the row, and planting depth. The distance between seeds along the row primarily determines the seeding rate. For each crop, under specific soil-climatic conditions, the seeding rate had an optimal value, as confirmed by numerous agronomists, including G.S. Dhillon *et al.* (2022). Uneven seed spacing leads to irregular seeding rates, which can reduce yield by up to 7%. Seed dispersion perpendicular to the row decreases the free space between rows. As a result, during inter-row cultivation, plants may be cut, which also lowers yield. Analysis of research by G. Dozet *et al.* (2020) showed that planting depth plays a crucial role in the uniformity of seedling emergence and consistent plant development during the growing season. Such unevenness can reduce yield by up to 9% and pose challenges during harvesting. Despite these advances, problems remained unresolved in prior studies: (1) effective reduction of seed velocity fluctuations within seed tubes of field pneumatic planters, (2) comprehensive understanding of how seed-wall interactions influence three-axis distribution in high-speed planting, and (3) integration of airflow design with seeding unit geometry to minimise "skips" and "doubles" under field conditions.

The aim of this article is to improve the seeding accuracy of the John Deere pneumatic planter by investigating the impact of airflow parameters and structural modifications to the seed retarder on seed velocity and distribution uniformity, as well as developing regression models to assess these effects.

MATERIALS AND METHODS

The improved seeding system of the pneumatic planter (Fig. 1) included an upper seeding sensor mounted on the seed tube, a lower seeding sensor placed on the seeding boot, and a seed retarder located between the seed tube and the seeding boot. The seed retarder consisted of a perforated cylinder with holes, an upper narrowing nozzle, a lower narrowing nozzle, a cylindrical curtain with a rigidly attached curved toothed rack, and a servo drive with a toothed wheel. The control unit was connected by electrical wiring to the upper and lower seeding sensors, as well as the servo drive.

Based on research by E. Aliiev (2019; 2023), a model of the seed retarder was constructed in the Simcenter

STAR-CCM+ software package to achieve the stated goal. The design and generated mesh of the internal area of the seed retarder, along with the geometric dimensions, were presented in Figure 2.

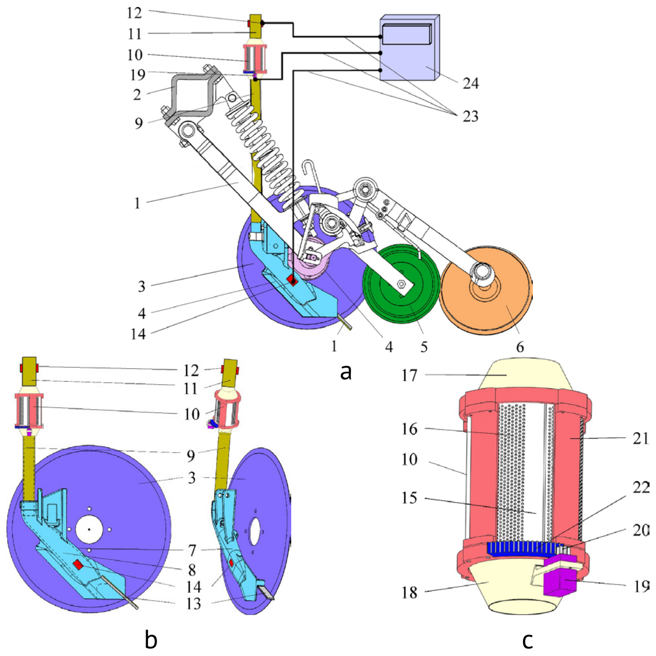

Figure 1. Structural-technological scheme of the improved seeding section of the pneumatic planter
Note: 1 – frame; 2 – clamp; 3 – single-disc furrow opener; 4 – bearing assembly; 5 – gauge wheel; 6 – closing wheel; 7 – seeding boot; 8 – seed channel; 9 – seed tube; 10 – seed retarder; 11 – seed conduit; 12 – upper seeding sensor; 13 – seed agitator; 14 – lower seeding sensor; 15 – perforated cylinder; 16 – perforations; 17 – upper narrowing nozzle; 18 – lower narrowing nozzle; 19 – servo drive; 20 – toothed wheel; 21 – cylindrical curtain; 22 – curved toothed rack; 23 – electrical wires; 24 – control unit
Source: compiled by the authors

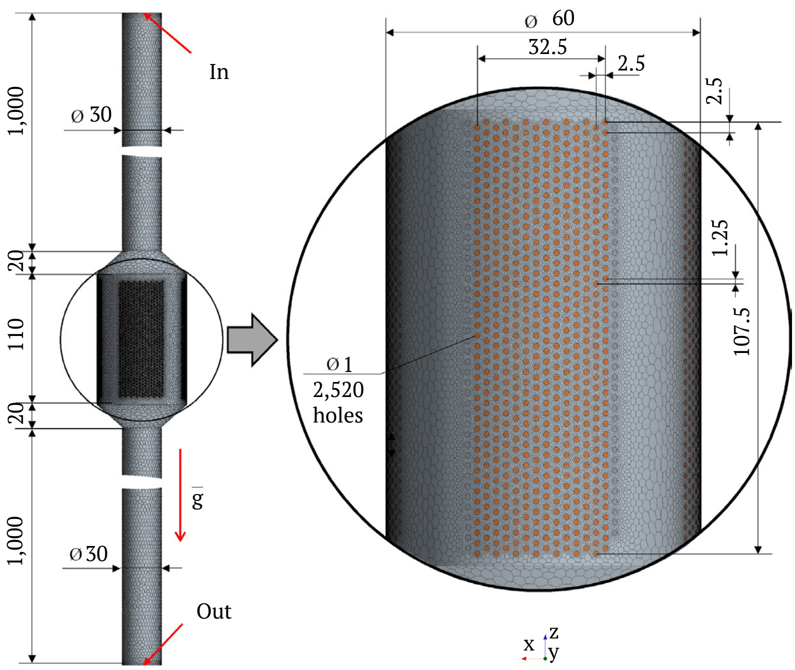

Figure 2. Design and generated mesh of the inner region of the seed retarder
Note: all sizes are in mm; g – free fall acceleration, m/s^2
Source: compiled by the authors

The geometric dimensions of the seed retarder were determined considering its possible placement and the structural features of the John Deere pneumatic planter. The following volume mesh generation models were applied in the Simcenter STAR-CCM+ software package: polyhedral mesh generator, surface mesh generator, extruder. The supporting parameters of these generators were set as follows: base size – 0.004 m; surface growth rate – 1.3; relative minimum size for cell decomposition – 10 %; minimum acceptable quality of facets – 0.001 m. The following physical models were applied for numerical simulation: real gas (air) Van der Waals model; *k-ε* turbulence model; segregated flow model; Lagrangian multiphase model, specifically the discrete element method (DEM) accounting for multiphase interaction. The simulation was conducted in a three-dimensional space with a non-stationary implicit solver. For air, the following physico-mechanical properties were assigned: dynamic viscosity – 1.85508×10^{-5} Pa · s; turbulent Prandtl number – 0.9; molecular mass – 28.9664 kg/kmol.

Pea seeds were selected as DEM particles, assuming a spherical shape. The physico-mechanical properties of the seeds were determined based on laboratory studies of pea seeds in accordance with M. Paksoy & C. Aydin (2006), İ. Yalçın *et al.* (2007), and K.M. Mahawar *et al.* (2018): effective diameter – 0.008 m; true density – 1,180 kg/m³; Poisson's ratio – 0.32; Young's modulus – 70 MPa. The following values were applied for particle-particle interactions: static friction coefficient – 0.62, normal and tangential coefficient of restitution – 0.3, absence of linear cohesion. The gravitational force vector according to Figure 2 had coordinates (0; 0.0; –9.81) m/s². The following boundary conditions were applied (according to Fig. 2): "In" boundary (diameter – 30 mm) – air velocity inlet model (V_{in}); "Out" boundary (diameter – 30 mm) – implicit outlet model; "holes" boundary (diameter – 1 mm, total quantity – 2520 pcs) – implicit outlet model; other boundaries – wall model. All boundaries except "Out" were impermeable to DEM particles (seeds). An injector of DEM particles (seeds) with 100 points was placed on the "Inlet" boundary. The probability of using a point for seed generation was set to 0.5. According to studies by S.I. Popov *et al.* (2022), the seeding rate of peas using conventional technology was 1.2 million seeds/ha. Considering the row spacing of 0.19 m, this gave 22.8 seeds/m or a seed spacing in the row of 0.044 m. The planter's seeding speed was assumed to be 1.5 m/s in accordance with V. Salo *et al.* (2022). Then, the injection speed of seeds at the top of the seed tube was calculated as 34.09 seeds/s. The initial seed velocity was assumed equal to the flow velocity.

The timestep of the solver was set to 0.01 s, with a maximum internal iterations value of 10, and an exposure time of 10 s. As research factors, the following were applied: the inlet air flow velocity V_a^{in} (5-25 m/s, step – 5 m/s), the ratio of the area of the outlet holes to the inlet area ε, defined as:

$$\varepsilon = \frac{S_h N_h}{S_{in}}, \tag{1}$$

where S_h – the area of the outlet hole (mm²), S_{in} – the inlet area (mm²), N_h – number of holes. By varying the number of outlet holes, the range of the $\boldsymbol{\varepsilon}$ factor was obtained: $\varepsilon = 0$ ($N_h = 0$), $\varepsilon = 0.4$ ($N_h = 360$), $\varepsilon = 0.8$ ($N_h = 720$), $\varepsilon = 1.2$ ($N_h = 1{,}080$), $\varepsilon = 1.6$ ($N_h = 1{,}440$), $\varepsilon = 2$ ($N_h = 1{,}800$), $\varepsilon = 2.4$ ($N_h = 2{,}160$), $\varepsilon = 2.8$ ($N_h = 2{,}520$). By sequentially assigning factor values, 40 experiments were conducted (8 × 5). The criteria for the experiments included the outlet air flow velocity V_a^{out}, the seed velocity at the outlet V_p^{out}, and the coefficient of seeding rate change η, defined as:

$$\eta = \frac{Q_{out}}{Q_{in}}, \tag{2}$$

where Q_{out} was defined the seeding rate at the outlet (seeds/s) and Q_{in} as the seeding rate at the inlet (seeds/s).

The second phase of the numerical modeling process used the Simcenter STAR-CCM+ software suite to develop 3D models of the key components of the precision seed section of the John Deere 90 Series pneumatic planter (Fig. 3), based on the data from M. Johnston (2003).

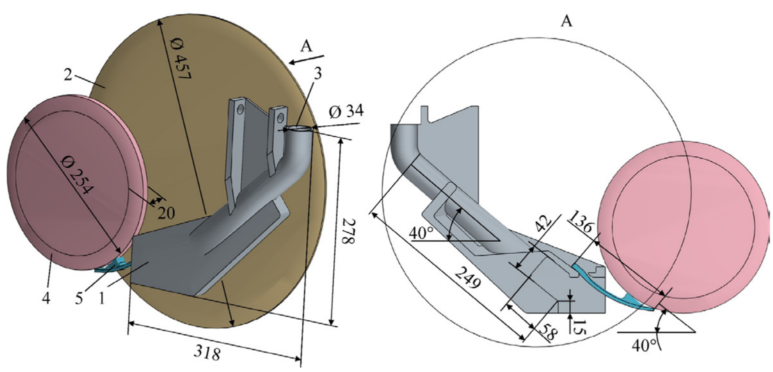

Figure 3. Geometric dimensions of the 3D model of the precision seed section of the John Deere 90 Series pneumatic planter

Note: all sizes are in mm; A – projection; 1 – seed boot; 2 – single disc furrow opener; 3 – seed tube; 4 – seedlock wheel; 5 – seed flap

Source: compiled by the authors

As the Lagrangian phase of the soil, DEM particles were applied with the following models: spherical particle, solid, constant density. The physico-mechanical properties of the soil particles were adopted according to research I. Shevchenko (2016) and had the following values: density – 1,100 kg/m^3, Poisson's ratio – 0.41, Young's modulus – 1.5 × 10^7. The interaction between seeds with each other and with the impermeable walls of the seed retarder was governed by the Hertz-Mindlin contact model. The static friction coefficient was assumed to be 0.61, the normal coefficient of restitution was 0.5, and the tangential coefficient of restitution was 0.3. According to research I. Shevchenko (2016), the particle size distribution of the soil followed a normal Gaussian distribution ranging from 10 mm to 36 mm. The distribution of soil particles in the study area (overseed, seeding, and undersowing layers) by size was shown in Figure 4. The soil depth was divided into 10 layers with a thickness of 0.02 m. The parameters of the non-stationary implicit solver Simcenter STAR-CCM+ were set as follows: time interval between steps – 0.01 s; maximum number of iterations per step – 5; time discretisation – first-order accuracy; minimum and maximum values of the Courant number for Lagrangian multiphase – 0.2 and 0.5, respectively; the total simulation time was 10 s.

A cross-section of the soil model area where the seed boot and single disc furrow opener of the precision seed section of the pneumatic planter passed was shown in Figure 4. In Figure 4, seeds that entered the tillage horizon of the soil consisting of the overseed (0-0.04 m), seeding (0.04-0.08 m), and undersowing (0.08-0.24 m) layers were marked.

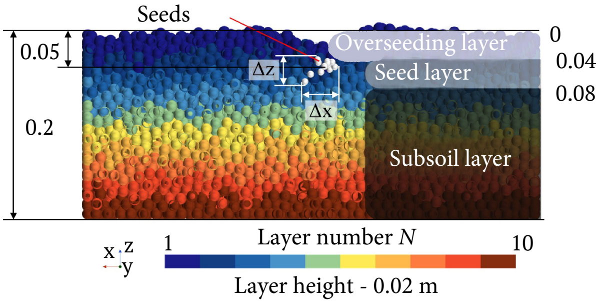

Figure 4. Cross-section of the soil model area
Note: all sizes are in m; N – layer number; Δx, Δz – deviation of the location of seeds in the soil along the x and z axes, respectively, m
Source: compiled by the authors

As a research factor, two variants were applied: the basic and improved (with seed retarder) designs of the seed section. The presence of the seed retarder in the seed section design was represented by changing the initial seed and air feed velocities. The quality criteria for seeding included the uniformity of seed distribution along the seeding line $\varepsilon_{\Delta y}$ and the dispersion of seeds in the depth Δz and width Δx of seeding. Data processing of numerical modelling was performed in the Wolfram Cloud software package.

RESULTS AND DISCUSSION

As a result of the first stage of numerical modelling, visualisations of the seed movement process in the seed retarder were obtained (Fig. 5).

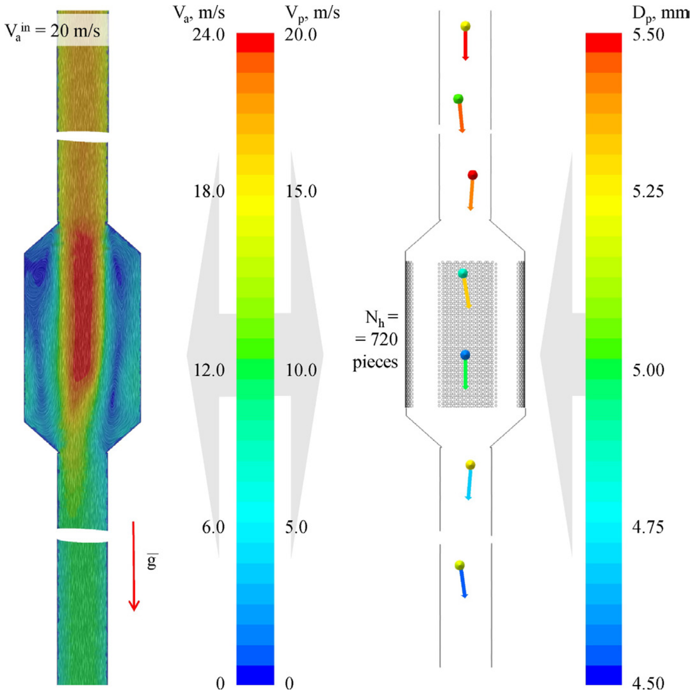

Figure 5. Visualisation of seed movement process in the seed retarder at $V_a^{in} = 20$ m/s, $\varepsilon = 0.8$
Note: V_a^{in} – inlet air flow velocity, m/s; V_a – air flow velocity, m/s; V_p – seed velocity, m/s; N_h – is number of holes; D_p – seed diameter, mm
Source: compiled by the authors

Based on the results of numerical modelling and processing of the obtained data, regression equations of the third order $V_a^{out}(V_a^{in}, \varepsilon)$ were obtained in decoded form without considering insignificant coefficients using the t-Student criterion (Fig. 6):

$$V_a^{out} = 0.4622 + 0.9319\, V_a^{in} - 2.558\, \varepsilon - 0.5134\, V_a^{in}\, \varepsilon + 2.436\, \varepsilon^2 + 0.1010\, V_a^{in}\, \varepsilon^2 - 0.5795\, \varepsilon^3. \quad (3)$$

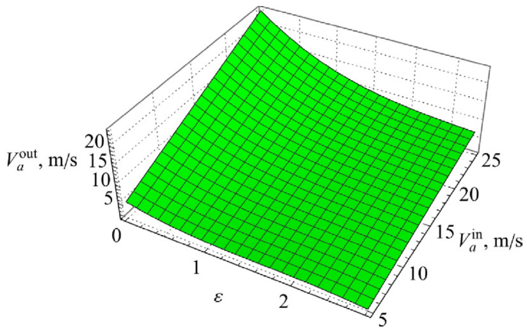

Figure 6. Dependence of outlet air flow velocity V_a^{out} of the seed retarder on the inlet air flow velocity V_a^{in} and the ratio of outlet hole area to inlet area ε
Note: V_a^{in} – inlet air flow velocity, m/s; ε – ratio of outlet hole area to inlet area; V_a^{out} – outlet air flow velocity, m/s
Source: compiled by the authors

Validation of the obtained equation using the Pearson correlation coefficient ($r = 0.95$) confirmed the adequacy of equation (3) within the investigated range of factor variation. Similarly, third-order regression equations $V_p^{out}(V_a^{in}, \varepsilon)$ were derived in decoded form without insignificant coefficients using the t-Student criterion (Fig. 7):

$$V_p^{out} = 0.5722 + 0.9093\, V_a^{in} - 3.747\, \varepsilon - 0.6304\, V_a^{in}\, \varepsilon + 3.566\, \varepsilon^2 + 0.1383\, V_a^{in}\, \varepsilon^2 - 0.8478\, \varepsilon^3. \quad (4)$$

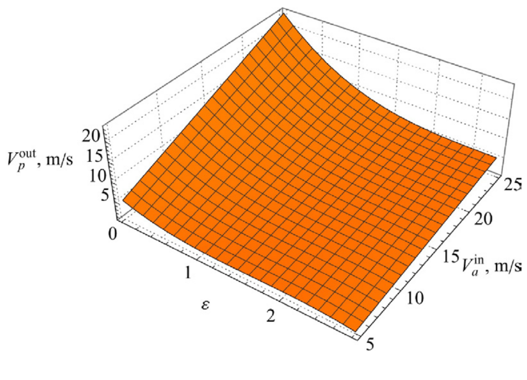

Figure 7. Dependence of seed velocity at the outlet V_p^{out} of the seed retarder on the inlet air flow velocity V_a^{in} and the ratio of outlet hole area to inlet area ε
Note: V_a^{in} – inlet air flow velocity, m/s; ε – the ratio of outlet hole area to inlet area; V_p^{out} – seed velocity at the outlet, m/s
Source: compiled by the authors

Validation of equation (4) using the Pearson correlation coefficient ($r = 0.94$) confirmed its adequacy within the investigated factor range. Similarly, a third-order regression equation $\eta(V_a^{in}, \varepsilon)$ was obtained in decoded form without insignificant coefficients using the t-Student criterion (Fig. 8):

$$\eta = 0.9795 + 0.000099\, V_a^{in} + 0.07435\, \varepsilon - 0.00341\, V_a^{in}\, \varepsilon - 0.0687\, \varepsilon^2 + 0.00238\, V_a^{in}\, \varepsilon^2 + 0.0165\, \varepsilon^3. \quad (5)$$

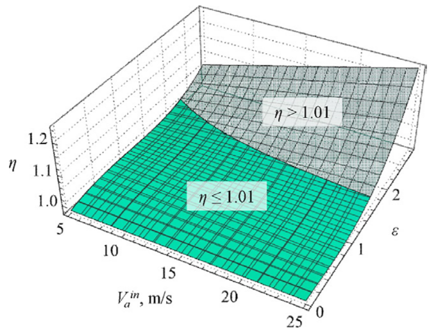

Figure 8. Dependence of the seeding rate change coefficient η on the inlet air flow velocity V_a^{in} and the ratio of outlet hole area to inlet area ε of the seed retarder
Note: V_a^{in} – inlet air flow velocity, m/s; ε – the ratio of outlet hole area to inlet area; η – seeding rate change coefficient
Source: compiled by the authors

Validation using the Pearson correlation coefficient ($r = 0.92$) confirmed the adequacy of equation (5) within the investigated range. Since optimal factor values differed for individual research criteria, a compromise optimisation problem was formulated as:

$$\begin{cases} V_p^{out}(V_a^{in}, \varepsilon) \rightarrow min, \\ \eta(V_a^{in}, \varepsilon) \leq 1{,}01. \end{cases} \quad (6)$$

Problem (6) was solved using the Wolfram Cloud software package. A graphical interpretation of the solution of equation (6) together with equations (4) and (5) was presented in Figure 9. The boundary separating the two regions determined the relationship between ε and V_a^{in}, expressed as:

$$\varepsilon = 0.567137 + 0.172935\, V_a^{in} + 0.00344297\, (V_a^{in})^2 - 0.0000296843\, (V_a^{in})^3. \quad (7)$$

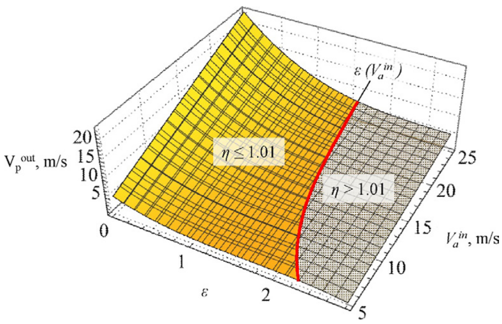

Figure 9. Graphical interpretation of the solution to equations (6) together with (5) and (4)
Note: V_a^{in} – inlet air flow velocity, m/s; ε – the ratio of outlet hole area to inlet area; V_p^{out} – seed velocity at the outlet, m/s; η – seeding rate change coefficient
Source: compiled by the authors

Substitution of equation (7) into equations (3), (4), and (5) made it possible to determine the following ranges of variation of the research criteria: $V_a^{out} \in [1.8; 9.4]$ m/s, $V_p^{out} \in [1.5; 6.6]$ m/s, $\varepsilon \in [1.60; 2.26]$. Equation (7) described the dependence of ε on V_a^{in} under condition (6). Within the specified range of V_a^{in}, ε was adjusted from 1.60 to 2.26.

As a result of the second stage of numerical modelling of the operation of the precision seed section of the John Deere 90 Series pneumatic planter, visualisations of soil aggregate distribution and velocity fields were obtained (Fig. 10). The maximum velocity of soil aggregates was 1.5 m/s. Based on the visualisation, the distribution of seeds within the tillage horizon and the furrow formed by the rolling of the seedlock wheel was clearly observed.

Visualisation of seed distribution along the seeding line (y-axis) and in depth (z-axis) was presented in Figure 11. The spatial distribution of seeds within the tillage horizon was illustrated in Figures 11 and 12. Based on these figures, the main statistical indicators of seeding accuracy were determined, including minimum, maximum, and average values, range, root-mean-square deviation, and coefficient of variation. The obtained indicators were summarised in Table 1.

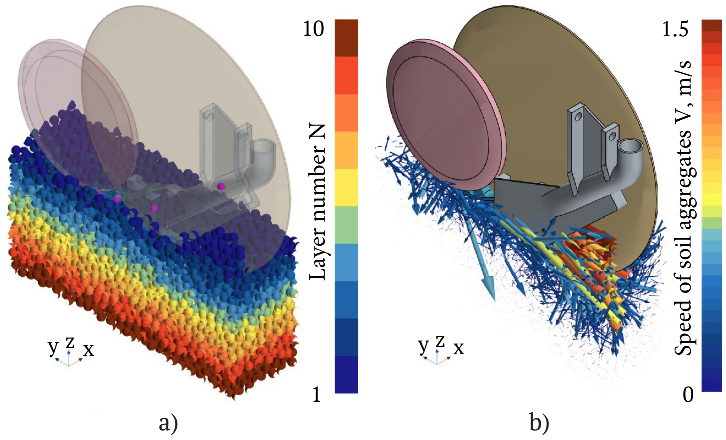

Figure 10. Visualisation of soil aggregates distribution (a) and their velocities (b) under the action of the precision seed section of the pneumatic planter
Source: compiled by the authors

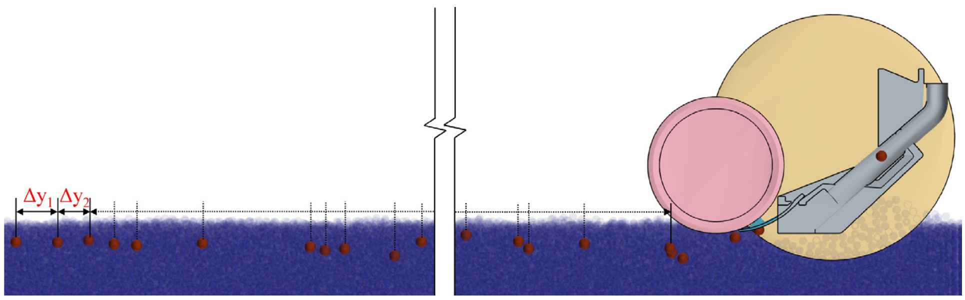

Figure 11. Visualisation of seed distribution resulting from seeding by the pneumatic planter
Note: Δy_1, Δy_2 – distance between seeds in the soil, m
Source: compiled by the authors

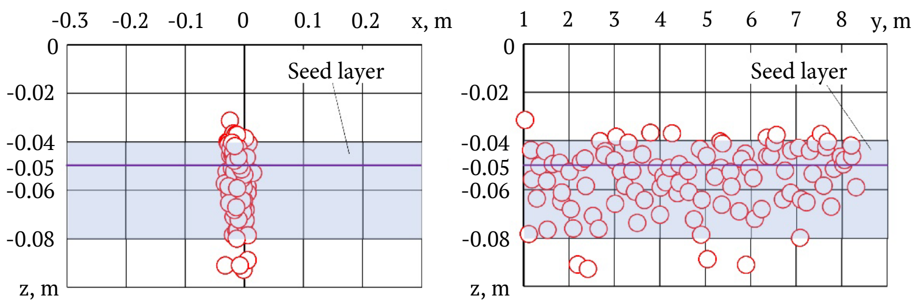

Figure 12. Seed distribution in the tillage horizon of the soil during seeding by the John Deere 90 Series planter
Note: x, z – coordinates, m
Source: compiled by the authors

Table 1. Results of numerical modelling of the seeding process by the John Deere 90 Series pneumatic planter for basic and improved designs

Indicator	*x, m*	*Δy, m*	*z, m*
Basic construction: $V_a^{out}=20$ m/s, $V_p^{out}=19.4$ m/s, $\varepsilon=0$			
Minimum value	– 0.03308	0.001752	– 0.09262
Maximum value	0.014296	0.119157	– 0.03118
Limit	0.023688	0.058703	0.030719
Mean square deviation	0.009868	0.029303	0.013423
Average value	– 0.00851	0.043593	– 0.04164
Coefficient of variation	– 1.15896	0.672183	– 0.32239
Improved design (with seed retarder): $V_a^{out}=9.4$ m/s, $V_p^{out}=6.6$ m/s, $\varepsilon=2.26$			
Minimum value	– 0.02977	0.040433	– 0.04631
Maximum value	0.01286	0.049324	– 0.04011
Limit	0.02131	0.004445	0.003101
Mean square deviation	0.005052	0.010627	0.00953
Average value	– 0.00827	0.044878	– 0.04973
Coefficient of variation	– 0.61091	0.223679	– 0.21306
Requirements for sowing accuracy			
Normalized value	± 0.025	0.044 ± 0.015	– 0.05 ± 0.01

Note: V_a^{out} – outlet air flow velocity, m/s; V_p^{out} – seed velocity at the outlet, m/s; ε – the ratio of outlet hole area to inlet area; *x*, *y*, *z* – seed placement coordinate, m
Source: compiled by the authors

Comparison of the obtained indicators with standardised values demonstrated that seed distribution along the x-axis met the specified requirements for both variants. Along the *z*-axis (seeding depth), the basic design exceeded standardised limits, with an average seeding depth of 0.041 ± 0.03 m, compared to 0.0497 ± 0.003 m for the improved design, while the standardised value was 0.05 ± 0.01 m. Visual analysis showed that some seeds in the basic design did not reach the seeding layer (0.04-0.08 m). For the basic design, a high unevenness of seeding along the seeding line was identified, with seed spacing ranging from 0.0017 m to 0.1192 m and a coefficient of variation of 0.672, compared to the standardized spacing of 0.044 ± 0.015 m. Only 47.5% of seeds met the standardised accuracy requirements. For the improved design, significantly better results were obtained, with seed spacing ranging from 0.0404 m to 0.0493 m and a coefficient of variation of 0.223, corresponding to 0.0448 ± 0.004 m. Thus, the improved design fully met the seeding accuracy requirements. The results of numerical modelling confirmed the effectiveness of incorporating a seed decelerator into the design of the pneumatic seeding unit. Adjustment of the decelerator parameters ensured stabilisation of seed outlet velocity and reduced seed dispersion in both depth and width of sowing. The obtained third-order regression equations confirmed the adequacy of the developed model and its compliance with real operating conditions. Thus, the improved seeding unit of the pneumatic seeder equipped with a seed decelerator ensured enhanced uniformity of seed distribution, which contributed to increased yield potential and improved efficiency of agricultural operations. The obtained results represent an important step toward the development of advanced precision farming technologies aimed at optimising seed use and increasing productivity.

The obtained results confirm the importance of improving the design of the sowing unit of the John Deere 90 Series pneumatic seeder. Numerical modelling and experimental studies demonstrated that the proposed technical solution with a seed decelerator significantly improves the uniformity of seed distribution in the seedbed. According to the studies by L.J. Liu *et al.* (2016), the main issue affecting the seeding accuracy of pneumatic seeders is the high velocity of seeds during transportation. The present study confirms this finding, as the uneven seed distribution is caused by significant velocity fluctuations during seed movement through the seed tube. However, unlike previous studies, the improved design incorporating a seed decelerator allows these effects to be minimised. The findings of K. Li *et al.* (2023) indicated that the accuracy of pneumatic seeders largely depended on the trajectory of seed movement, which is influenced by airflow conditions and interactions between seeds and internal surfaces of the seeding system. In the study by Y. Li *et al.* (2016), a global review of precision maize planters showed that pneumatic seeding systems provide high metering accuracy but suffer from unstable seed trajectories during transportation through the seed tube. High seed velocities and turbulent airflow were identified as the main causes of uneven seed spacing and depth variation. However, the study did not propose specific technical solutions to reduce seed velocity or seed-wall collisions. The work of A. Boiko *et al.* (2018) focused on structural improvements of precision seeders aimed at increasing efficiency and reducing resource consumption. While improved metering performance was demonstrated, the influence of airflow and seed dynamics inside the seed tube on three-dimensional seed distribution was not sufficiently analysed, leaving the problem of seed motion stabilisation unresolved. In the study by A.A. Koller *et al.* (2005), the importance of controlling seed trajectory and orientation to improve planting accuracy was emphasised. The authors showed that uncontrolled seed motion and impacts with internal surfaces reduced placement precision. However, airflow-assisted seed transport and methods for reducing seed velocity in pneumatic systems were not addressed. Thus, despite these contributions, unresolved issues remained regarding excessive seed velocity, seed-wall collisions, and trajectory instability in pneumatic seed tubes. The present study addressed these gaps by proposing a seed decelerator that reduced seed velocity before reaching the seedbed, thereby improving seeding uniformity in spacing, depth, and lateral distribution.

As stated in the works of J. Turan *et al.* (2015), seeding uniformity is determined in three dimensions: seed spacing within the row, lateral seed distribution perpendicular to the row, and seeding depth. The results of this study show a significant improvement in uniformity across all three parameters. This is confirmed by a reduction in the standard deviation of seed spacing and increased stability of seed placement depth. An analysis of the studies by H.Y. Cao *et al.* (2015), A. Özköse (2017), and G. Dozet *et al.* (2020) showed that sowing depth was a key factor affecting seedling emergence uniformity and subsequent plant development. In the study by H.Y. Cao *et al.* (2015), it was demonstrated that deviations from the optimal sowing depth of maize resulted in delayed emergence and uneven root development. Excessive depth limited oxygen availability, while shallow sowing increased sensitivity to soil moisture variability. However, technical factors related to seeding mechanisms were not considered. The work of A. Özköse (2017) confirmed that uniform sowing depth significantly improved emergence and yield stability of pea genotypes, whereas depth variability led to uneven plant development. The causes of this variability associated with seed delivery dynamics were not analysed. According to G. Dozet *et al.* (2020), non-uniform sowing depth negatively affected soybean stand establishment and optimal plant density. Although the agronomic consequences were clearly identified, the influence of pneumatic seeding parameters on depth stability was not addressed. Thus, previous studies highlighted the importance of stable sowing depth but did not investigate the role of airflow conditions and seed motion control in pneumatic seeders. The present research addressed this limitation by establishing relationships between airflow velocity, seed decelerator configuration, and seeding depth stability, contributing to more uniform seed placement in the soil.

The proposed improvement in the design of the sowing unit of the John Deere 90 Series pneumatic seeder significantly enhances seeding uniformity by reducing "skips" and "doubles." Compared to existing seeder designs, the incorporation of a seed decelerator reduces seed velocity prior to entering the furrow, thereby minimising seed scattering and increasing seeding accuracy. The obtained results have practical significance, as their implementation can reduce yield losses caused by uneven seeding. Further research is planned to refine the decelerator control algorithm to adapt it to different seeder operating speeds and variations in soil structure.

CONCLUSIONS

The numerical simulation of the seed decelerator in the John Deere pneumatic seeder, performed in the Simcenter Star-CCM+ software package, provided a visualisation of seed motion and airflow within the working area of the decelerator. Based on numerical modeling and subsequent data processing in the Wolfram Cloud software package, second-order regression equations were derived in decoded form, excluding insignificant coefficients according to Student's t-test. These equations described the dependencies of the outlet airflow velocity V_a^{out}, the outlet seed velocity V_p^{out}, and the seeding rate change coefficient η on the inlet airflow velocity V_a^{in} and the ratio of the outlet area to the inlet area ε. According to agronomic requirements, the deviation of the seeding rate was required not to exceed 1%. The derived equation expressed the dependence of the outlet-to-inlet area ratio ε on the inlet airflow velocity V_a^{in}, ensuring that $\eta \leqslant 1.01$. Within the specified range of inlet airflow velocities, ε was adjusted within the range of 1.60 to 2.26.

Numerical modelling of both the baseline and improved designs of the John Deere 90 Series pneumatic seeder's planting unit revealed key indicators of seeding uniformity. For the baseline design, the seed spacing along the row varied between 0.0017 m and 0.1192 m, with a coefficient of variation of 0.672. The standard spacing was 0.044 ± 0.015 m. Distances below 0.029 m indicated "double seeding," while distances above 0.059 m indicated "skips." The depth distribution of seeds was highly variable, exceeding standardised values. The average planting depth was 0.041 ± 0.03 m, while the required depth was 0.05 ± 0.01 m, with 52.5% of seeds failing to reach the target planting layer (0.04-0.08 m) in the cultivated soil horizon. The improved planting unit design demonstrated significantly better results. The seed spacing ranged from 0.0404 m to 0.0493 m, with a coefficient of variation of 0.223, resulting in an achieved spacing of 0.0448 ± 0.004 m. This confirmed that the improved design fully met the required seeding precision standards.

Further research may focus on the experimental verification of the obtained results under field conditions, allowing for a refinement of the decelerator parameters for different types of seeders and soil conditions. Additionally, studying the impact of other design modifications on seed distribution uniformity is promising, particularly in terms of variations in the geometry of the outlet openings and the materials used in the decelerator's construction. The potential for further development includes the integration of intelligent monitoring and adjustment systems for the seeding process based on real-time sensor data. This will enhance seeding accuracy and automate the adjustment of seeding unit parameters in real time. Moreover, further improvements may facilitate adaptation of the design to different crops, increasing the versatility of the technological solution.

ACKNOWLEDGEMENTS

None.

FUNDING

None.

CONFLICT OF INTEREST

None.

REFERENCES

[1] Aliiev, E.B. (2019). *Physical and mathematical models of the processes of precision separation of sunflower seed material*. Zaporizhzhia: STATUS.

[2] Aliiev, E.B. (2023). *Numerical modeling of agro-industrial production processes*. Kyiv: Agrarian Science. doi: 10.31073/978-966-540-584-9.

[3] Boiko, A., Popyk, P., Gerasymchuk, I., Bannyi, O., & Gerasymchuk, N. (2018). Application of the new structural solutions in the seeders for precision sowing as a resource saving direction. *Eastern-European Journal of Enterprise Technologies*, 5(1(95)), 46-53. doi: 10.15587/1729-4061.2018.142023.

[4] Cao, H.Y., Wang, D.B., Shi, J.G., Zhu, K.L., Dong, S.T., Liu, P., Zhao, B., & Zhang, J.W. (2015). Effects of sowing depth on seedling traits and root characteristics of summer maize. *Ying Yong Sheng Tai Xue Bao*, 26(8), 2397-2404.

[5] Dhillon, G.S., Baarda, L., Gretzinger, M., & Coles, K. (2022). Effect of precision planting and seeding rates on canola plant density and seed yield in southern Alberta. *Canadian Journal of Plant Science*, 102(3), 698-709. doi: 10.1139/cjps-2020-0186.

[6] Dozet, G., Đukić, V., Miladinov, Z., Cvijanović, G., & Ranđelović, P. (2020). Sowing depth – a significant factor for establishing the optimal number of plants per unit area of soybean. *Journal of Agronomy, Technology and Engineering Management*, 3(6), 516-522.

[7] Johnston, M. (2003). *Seed boot for a seeding machine (U.S. Patent No. US7168376B2)*. Retrieved from https://patents.google.com/patent/US7168376B2/en.

[8] Koller, A.A., Taylor, R.K., Weckler, P.R., Buser, M.D., & Raun, W.R. (2013). Design, performance prediction, and validation of a seed orienting corn planter. In *2013 ASABE annual international meeting* (Paper No. 131620580). Kansas City: American Society of Agricultural and Biological Engineers. doi: 10.13031/aim.20131620580.

[9] Li, K., Li, S., Ni, X., Lu, B., & Zhao, B. (2023). Analysis and experimental of seeding process of pneumatic split seeder for cotton. *Agriculture*, 13(5), article number 1050. doi: 10.3390/agriculture13051050.

[10] Li, Y., Bingxin, Y., Yiming, Y., Xiantao, H., Quanwei, L., Zhijie, L., Yin, X., Zhang, D., & Cui, T. (2016). Global overview of research progress and development of precision maize planters. *International Journal of Agricultural and Biological Engineering,* 9(1), 9-26.

[11] Lin, H.-T., & Lee, Y.-H. (2023). Implementing a precision pneumatic plug tray seeder with high seeding rates for Brassicaceae seeds via real-time trajectory tracking control. *Actuators*, 12(9), article number 340. doi: 10.3390/act12090340.

[12] Liu, L.J., Yang, H., & Ma, S.C. (2016). Experimental study on performance of pneumatic seeding system. *International Journal of Agricultural and Biological Engineering*, 9(6), 84-90. doi: 10.3965/j.ijabe.20160906.2129.

[13] Mahawar, M.K., Samuel, D.V.K., Sinha, J.P., & Jalgaonkar, K. (2018). Moisture-dependent physical and physiological properties of accelerated aged pea (*Pisum sativum* L.) seeds. *Current Science*, 114(4), 909-915. doi :10.18520/cs/v114/i04/909-915.

[14] Özköse, A. (2017). Effect of sowing depth on yield and some yield components of pea genotypes. *Sakarya University Journal of Science*, 21(6), 1188-1200. doi: 10.16984/saufenbilder.306457.

[15] Paksoy, M., & Aydin, C. (2006). Determination of some physical and mechanical properties of pea (*Pisum sativum* L.) seeds. *Pakistan Journal of Biological Sciences*, 9(1), 26-29. doi: 10.3923/pjbs.2006.26.29.

[16] Popov, S.I., Hlubokyi, O.M., & Avramenko, S.V. (2022). Sowing rate effect on the performance and seed quality of pea cultivars in the eastern Forest-steppe of Ukraine. *Selection and Seed Breeding*, 121, 94-104. doi: 10.30835/2413-7510.2022.261001.

[17] Salo, V., Leshchenko, S., Loozan, P., & Salo, L. (2022). *Machines for sowing, planting, and crop care*. Kropyvnytskyi: CNTU.

[18] Shevchenko, I.A. (2016). *Management of the agro-physical condition of the soil environment*. Kyiv: Vinichenko Publishing House.

[19] Tang, H., Xu, F., Guan, T., Xu, C., & Wang, J. (2023). Design and test of a pneumatic type of high-speed maize precision seed metering device. *Computers and Electronics in Agriculture*, 211, article number 107997. doi: 10.1016/j.compag.2023.107997.

[20] Turan, J., Višacki, V., Sedlar, A., Pantelić, S., Findura, P., Máchal, P., & Mareček, J. (2015). Seeder with different seeding apparatus in maize sowing. *Acta Universitatis Agriculturae et Silviculturae Mendelianae Brunensis,* 63(1), 137-141. doi: 10.11118/actaun201563010137.

[21] Wei, M., Diao, P., & Wang, W. (2022). Design and experiment of the seed delivery device with a rotating brush wheel for precision seeder. *Engenharia Agrícola*, 42(6). doi: 10.1590/1809-4430-eng.agric.v42n6e20220089/2022.

[22] Xiong, D., Wu, M., Xie, W., Liu, R., & Luo, H. (2021). Design and experimental study of the general mechanical pneumatic combined seed metering device. *Applied Sciences*, 11(16), article number 7223. doi: 10.3390/app11167223.
[23] Yalçın, İ., Özarslan, C., & Akbaş, T. (2007). Physical properties of pea (*Pisum sativum*) seed. *Journal of Food Engineering*, 79(2), 731-735. doi: 10.1016/j.jfoodeng.2006.02.039.

Ельчин Алієв
Доктор технічних наук, старший дослідник
Дніпровський державний аграрно-економічний університет
49600, вул. Сергія Єфремова, 25, м. Дніпро, Україна
https://orcid.org/0000-0003-4006-8803

Ольга Алієва
Доктор філософії
Інститут олійних культур Національної академії аграрних наук України
69055, вул. Інститутська, 1, м. Сонячне, Запорізька обл., Україна
https://orcid.org/0000-0002-2766-7548

Петро Безверхній
Доктор філософії
Асоціація фермерських господарств «Ольвія»
74000, с. Високопілля, Бериславський р-н, Херсонська обл., Україна
https://orcid.org/0009-0000-0368-7870

Павло Луц
Кандидат технічних наук
Вінницький національний аграрний університет
21008, вул. Сонячна, 3, м. Вінниця, Україна
https://orcid.org/0000-0002-3776-8940

Симуляція удосконаленої системи подачі насіння пневматичної зернової сівалки

Анотація. Метою цього дослідження було підвищення точності розміщення насіння в пневматичному сівалці John Deere шляхом покращення конструкції системи подачі насіння в висівній секції. Удосконалена висівна секція включала кілька основних компонентів: верхній та нижній датчики норми висіву, сповільнювач насіння, що складається з перфорованого циліндра з отворами, верхні та нижні вузькі розтруби, циліндричне забрало з жорстко змонтованою вигнутою зубчастою рейкою та сервоприводом із зубчастим колесом. Ці удосконалення були спрямовані на поліпшення рівномірності розподілу насіння та оптимізацію точності посадки. Чисельні моделювання сповільнювача насіння, проведені за допомогою програмного пакету Simcenter Star-CCM+, дозволили візуалізувати як рух насіння, так і динаміку повітряного потоку в робочій зоні сповільнювача. Регресійні рівняння другого порядку були сформульовані на основі чисельних моделювань та обробки даних у програмному пакеті Wolfram Cloud. Ці рівняння, уточнені шляхом видалення незначних коефіцієнтів відповідно до t-тесту Стьюдента, описали залежності основних параметрів: швидкість повітря на виході зі сповільнювача насіння (V_a^{out}), швидкість насіння на виході (V_p^{out}) та коефіцієнт зміни норми висіву (η) як функції швидкості вхідного повітря (V_a^{in}) та співвідношення площі виходу до площі входу (ε). Згідно з агрономічними вимогами, допустиме відхилення норми висіву не повинно перевищувати 1 %. Для стандартної та удосконаленої конструкцій висівної секції пневматичної сівалки John Deere 90 Series були проведені порівняльні чисельні моделювання. Результати показали, що поліпшена конструкція забезпечує кращу ефективність, забезпечуючи більш рівномірне розміщення насіння. Відстань між насінинами в удосконаленій конструкції варіюється від 0,0404 м до 0,0493 м, при коефіцієнті варіації 0,223, що відповідає середньому розміру відстані 0,0448 ± 0,004 м. Ці результати підтверджують, що удосконалена висівна секція відповідає необхідним вимогам точності, що веде до підвищення потенціалу урожайності. Результати дослідження можуть бути використані для подальшої оптимізації пневматичних сівалок з метою підвищення точності висіву та зменшення втрат врожаю

Ключові слова: сповільнювач; параметри; точність висіву; швидкість; потік повітря

Machinery & Energetics
Vol. 17, No. 1. 2026

Journal homepage:
https://technicalscience.com.ua/en

UDC 621.791.7:669.14
DOI: 10.31548/machinery/1.2026.20

ISSN 2663-1334
e-ISSN 2663-1342

Mothanna Taha Mohammed Fattah Agha*
College of Agriculture
Al-Qasim Green University
51001, Babylon, Iraq
https://orcid.org/0000-0002-7957-3404

Evaluation of thermo-mechanical response of components by rotary friction welding technique

Abstract. Rotary friction welding (RFW) is one of the most important processes for bonding metal together, either alike or unlike. RFW has gained acceptance among many manufacturing sectors because it reduces thermal distortion, produces fewer heat affected zone areas, provides for increased production rates, and eliminates the need for filler metals. The focus of this investigation was the mechanical properties of welds with an emphasis placed upon the relationship of spindle speed with the quality of the welds for three different types of materials that are bonded; i.e., aluminium-aluminium, steel-aluminium, and steel-steel. These welds were fabricated utilising the rotary friction welding technique at a lathe. Tensile tests were performed to measure how well the welds would perform under stress. Ultrasonic inspections were completed to find any cracks or holes inside the welds. Micro measurements were taken to assess the weld zone. Hardness tests were performed to determine the amount of resistance the material could withstand. Finally, metallographic analysis was conducted to examine the micro structural characteristics of the welds. The tests revealed that as the spindle speed increased so did the loss of elastic resistance of the welds. It was determined that this loss of elastic resistance resulted from the high temperatures produced by the high spindle speeds causing micro-structure softening. At 1,250 RPM, the optimal (mechanical) performance was found as well as the highest level of mechanical properties such as strength and hardness. Furthermore, through ultrasonic testing, it was confirmed that all weld seams produced by RFW were completely free of defects. Therefore, these results clearly demonstrate that RFW can produce weld seams with high mechanical properties and no defects if optimum process conditions exist, especially if the spindle speed is adjusted to match the respective materials

Keywords: solid-state joining; thermo-mechanical analysis; heat-affected zone; metallographic characterisation; dissimilar metal welding

INTRODUCTION

Rotary friction welding (RFW), a process that does not melt the original material of two metal parts which are joined together through friction heat generated by a rotating spindle is capable of producing high-strength welds between very different types of metals. A significant advantage of RFW over other processes is that it produces minimal heat input thereby creating little or no thermal distortion and/or a heat-affected zone, therefore RFW eliminates the need for filler materials or shielding gases. However, although there are many advantages to using RFW, the process has some limitations, specifically, it requires the proper selection of the metal to be welded and proper operating conditions including spindle speed and pressure to produce a high-quality weld. The applications of drill pipe, truck axle and hydraulic cylinder rod are examples of the versatility and efficiency of the RFW process.

Researchers H. Ghari *et al.* (2024) conducted a detailed literature review on rotary friction welding (RFW) as it relates to aluminium steel weldments; however, they focused their discussion primarily on the metallurgical transformations occurring during the RFW process at the weld interface, specifically those associated with the development and management of brittle intermetallic compounds (IMCs). They also used artificial neural networks to develop relationships between RFW process variables and mechanical properties. N. Gangil *et al.* (2025) have reviewed linear

Article's History: Received: 09.10.2025; Revised: 05.01.2026; Accepted: 26.02.2026; Published: 30.03.2026.

Suggested Citation:
Agha, M.T.M.F. (2026). Evaluation of thermo-mechanical response of components by rotary friction welding technique. *Machinery & Energetics,* 17(1), 20-27. doi: 10.31548/machinery/1.2026.20.

*Corresponding author

friction welding (LFW) and focused specifically on how LFW is used to join different types of materials (both similar and dissimilar). The study provided a detailed overview of the LFW process, characteristics of the welds formed, microstructural changes that occur during LFW and the impact of various parameters on the quality of the welds formed. It identified potential applications of LFW in aerospace and transportation industries and outlines the major areas of research that will be important in the future for the development of LFW. J. Wang *et al.* (2021) were able to analyse the formation of joints between Fe-Al and the mechanism of evolution for IMCs using Laser Weld/Braze processes as opposed to Friction Welding, which provided an additional understanding of the mechanisms involved in solid-state and fusion-assisted joining. Researchers M. Farbakhti *et al.* (2025) studied the joining of both the same materials (e.g., steel) and different materials (e.g., steel-aluminium, aluminium-copper) through RFW. The study examined how the various process parameters used during RFW can impact the microstructural evolution; grain size reduction; carbide dissolution; and redistribution of inclusions, while at the same time relating these changes to the mechanical characteristics of the weld and addressing problems associated with the welds, such as residual stresses and the development of brittle phase(s). Overall, these studies demonstrates that processing conditions have a significant effect on the interfacial microstructure and mechanical characteristics of welds formed using RFW and other similar processes, with the primary constraint on dissimilar joints (i.e., steel/aluminium and aluminium/copper) being due to the brittleness induced by IMCs, requiring either optimisation of parameters; use of interlayers; or application of post weld heat treatment. There have been studies into advancements in rotary and inertia friction welding (RFW/IFW) processes for like and unlike metals. These are looking into how the process parameters can influence the microstructure and mechanical behaviour. X. Xu *et al.* (2020) studied inertia friction welding of 1045 carbon steel and 30CrMnSiNi2A high strength low alloy (HSLA) Steel, with results indicating that the optimal mechanical properties were achieved at a speed of 2,200 rpm, with 713 MPa ultimate tensile strength and 97% joint efficiency, due to refinement of martensitic and bainitic microstructures. EN1A mild steel joints welded in both dry and wet conditions were examined by V.V. Kulkarni & P.C. Kulkarni (2021). The authors indicated the advantages of the process; particularly the EN1A mild steel joints had superior joint strength when compared to dry joints and there was no distortion as a result of the process. Samples of stainless steel types code (SS316-SS304-SS202) were illustrated for performance by J.S. Chatha *et al.* (2021). The results showed that SS316-SS304 performed better than all of their other test samples. They reported that the SS316-SS304 samples had a tensile strength of 3,920 kgf and a hardness of 278 HV. L.F. Malau *et al.* (2025) studied AA6061 aluminium alloy joints and found that an increase in welding time resulted in increased strength, with the greatest strength being observed after 10 seconds (223.2 MPa). With further increases in welding time, excessive flash developed. The importance of compression test in forming good metallurgical bonds in Al-Cu dissimilar joints was emphasised by R. Ariyansah *et al.* (2025); they demonstrated that the application of 20 kg/cm^2 resulted in the most optimal metallurgical bonding with high strength and low levels of intermetallic compounds (IMCs). Ultimately, N. Gotawala & A. Shrivastava (2021) investigated Al6061-mild steel joints; they found that the highest tensile strength (136 MPa), was achieved when using an intermediate welding rate (20 mm/min). This increased tensile strength was obtained as a result of reduced intermetallic compound (IMC) layer thicknesses and enhanced dynamic recrystallisation. In general, all the above mentioned studies demonstrated that optimising the welding process through varying speed, time and/or pressure are key factors in producing high-quality solid-state welds without defects from various materials. The purpose of this study was to investigate the stiffness and mechanical properties of cylindrical joints manufactured using rotary friction welding on a parallel lathe machine.

MATERIALS AND METHODS

The basis materials were 15 mm diameter cylindrical bars. Their chemical compositions were assessed using a Thermo Fisher Scientific analyser (USA) in compliance with ASTM E18 guidelines (ASTM International, 2025). and are summarised in Tables 1 and 2. Material 1 corresponds to steel grade A60, predominantly composed of iron (approximately 97.972 wt%) with minor alloying elements such as Mn, Cu, Ni, Cr, Mo, Co, and Sn. Material 2 is aluminium alloy AA 6063, consisting mainly of aluminium (approximately 99.25 wt%) with small quantities of Fe, Cr, Ti, V, Sn, Pb, and Zn. The mechanical behavior of both materials was evaluated through tensile testing. For this purpose, five specimens were machined to a diameter of 12 mm as shown in Figure 1.

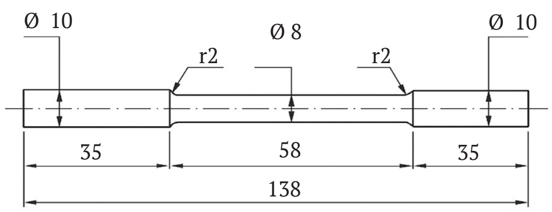

Figure 1. The dimensions of the specimen used for RFW

Source: developed by the author

Table 1. Chemical composition of material 1 (Steel)

Element	Sn	Mo	Ni	Co	Fe	Mn	Cr	Cu
Wt%	0.010	0.052	0.432	0.146	97.968	0.810	0.165	0.414
Error	±0.004	±0.002	±0.034	±0.062	±0.085	±0.031	±0.012	±0.026

Source: developed by the author

Table 2. Chemical composition of material 2 (AA 6063)

Element	Sn	Pb	Zn	Al	Fe	Ti	Cr	V
Wt%	0.011	0.004	0.011	99.237	0.326	0.025	0.072	0.030
Error	±0.005	±0.001	±0.002	±0.021	±0.013	±0.003	±0.005	±0.006

Source: developed by the author

To minimise machining effects, the gauge sections were ground parallel to the specimen axis using abrasive papers. Rotary friction welding was performed on a parallel lathe equipped with a universal carriage and threading system (model E3N-01), which provided all necessary tooling for specimen preparation as shown in Figure 2.

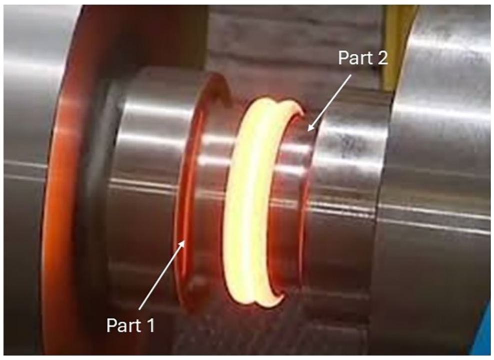

Figure 2. Test tube specimen prior to sectioning after soldering

Source: photo by the author

Tensile tests were conducted using a WP310 GUNT HAMBURG hydraulic testing machine (Gerätebau GmbH, Germany) with a 50 kN load cell and a displacement speed ranging from 0 to 425 mm/min. Ultrasonic inspection was carried out based on the transmission, reflection, and absorption of ultrasonic waves within the material. The emitted pulse was reflected from the specimen boundaries or internal discontinuities and returned to the transducer, serving as both transmitter and receiver. A D10+ ultrasonic device (United Kingdom) operating at 3 MHz was used for surface examination as shown in Figure 3.

Figure 3. D10+ ultrasonic detector

Source: photo by the author

Microhardness tests were carried out on a 24i hardness tester (Germany) that was modified to allow the microhardness to be tested on welds; an example is shown in Figure 4. The composition of the two materials used in this investigation are detailed in Tables 1 and 2. Steel grade A60 material 1 contained approximately 97.972wt% iron and trace amounts of other alloying elements, manganese, copper, nickel, chromium, molybdenum, cobalt, tin, as indicated by the relative measurement uncertainties. Aluminium alloy AA 6063, material 2, had a major constituent of aluminium at approximately 99.25wt%, with lesser amounts of iron, chromium, titanium, vanadium, lead, tin and zinc. The mechanical properties of both materials were evaluated through tensile testing, and were summarised in Tables 3 and 4.

Table 3. Characteristics of test tube in steel

Variance	R_e(N/mm²)	R_m(N/mm²)	A%	Hardness
A 60	336	590-710	14.5	HV = 171-204

Source: developed by the author

Table 4. Characteristics of test tube in AA 6063

Variance	R_e(N/mm²)	R_m(N/mm²)	A%	Hardness
AA 6063	24	50	48	HV = 15

Source: developed by the author

Steel A60 exhibited a yield strength of 336 N/mm², a tensile strength between 590-710 N/mm², elongation of 14.5%, and hardness in the range of HV171-204, indicating high strength and moderate ductility. The AA 6063 alloy, on the other hand, has significantly less strength than does steel, with a yield strength of 24 N/mm² and tensile strength of 50 N/mm², but very much greater elongation (48%), and very much lower hardness (HV15), which suggests that it is softer and more ductile than steel.

RESULTS AND DISCUSSION

The basis of ultrasonic testing is the behaviour of sound traveling through materials as a result of wave propagation; where in the case of specimens, the specimen receives high frequency acoustic energy which then travels through it and is absorbed and reflected by the interior structure of the specimen. When the returned waveform comes from either the opposite side of the weld or the subsurface defect, the waveform will go back through the same transducer (transmits and receives), thereby enabling the detection and description of possible defects. Analysis of the ultrasonic signals collected from the welded joint found that the joints demonstrated adequate strength; there were no large variations in the ultrasonic pulse that returned, which indicated there were no ultrasonic reflections due to defects and therefore the transmitted waves had not encountered any obstructions. This evidence supports the premise that bonding was uniform over the entire area of contact rather than only at the edges of the weld. Table 5 shows the elastic resistance of the three different types of welds as a function of the spindle speed.

Table 5. Elastic resistance of welded specimens at different spindle rotational speeds

Welded test pieces	Steel-Steel	Aluminium- Aluminium	Steel- Aluminium
900 tr/min	456.72 N/mm²	88.66 N/mm²	187.88 N/mm²
1,250 tr/min	304.88 N/mm²	69.83 N/mm²	159.55 N/mm²
1,800 tr/min	225.34 N/mm²	27.76 N/mm²	146.77 N/mm²

Source: developed by the author

The results clearly show that, regardless of type of joint (aluminium/aluminium, aluminium/steel, or steel/steel), the elastic resistance of the welds decreased as the spindle speed was increased. In terms of actual values: (i) The elastic limit of steel/steel welds decreased from 456.72 N/mm² at a spindle speed of 900 tr/min to an elastic limit of 225.34 N/mm² at a spindle speed of 1,800 tr/min; (ii) For aluminium/aluminium welds, the elastic limit dropped from 88.66 N/mm² to 26.86 N/mm²; and (iii) The elastic limit of aluminium/steel welds decreased from 187.88 N/mm² to 146.77 N/mm² over the same speed interval. These results suggest that an increase in spindle speed during welding will generally lower the elastic resistance of the weld metal, presumably due to the higher temperatures generated during high-speed welding causing some degradation of the microstructure of the weld metal and thus lowering its elastic modulus, and ultimately, its elastic resistance. The variation of Vickers microhardness in the welded joints due to the spindle rotation at 900, 1,250, and 1,800 rpm is shown in Figure 4.

The hardness profiles from this figure will help understand the effect of the rotational speed on the mechanical properties of the welded zones. The peaks of the hardness value (near the weld interface) in Figure 4a, representing the steel-aluminium weld, are higher on the aluminium side. The hardness peak is due to the formation of IMCs, which are harder but also brittle in nature. The highest hardness is observed at 900 rpm due to lower heat input and finer microstructural features, while increasing the speed to 1,250 rpm and 1,800 rpm results in reduced hardness caused by greater heat input and coarser IMC formation. Figure 4b, representing the steel/steel joint, shows relatively uniform hardness on both sides of the weld, with a slight peak at the thermos-mechanically affected zone (TMAZ). Similar to the previous case, the highest hardness occurs at 900 rpm, while higher speeds lead to reduced hardness as a result of increased heat generation and microstructural softening. Hardness values for the aluminium-aluminium joint are, on average, the lowest of all three cases (Fig. 4c). The maximum hardness was also found to occur at a spindle speed of 900 rpm; the hardness decreased with each increase in spindle speed, as a result of increased grain size and the dissolution of strengthening precipitates.

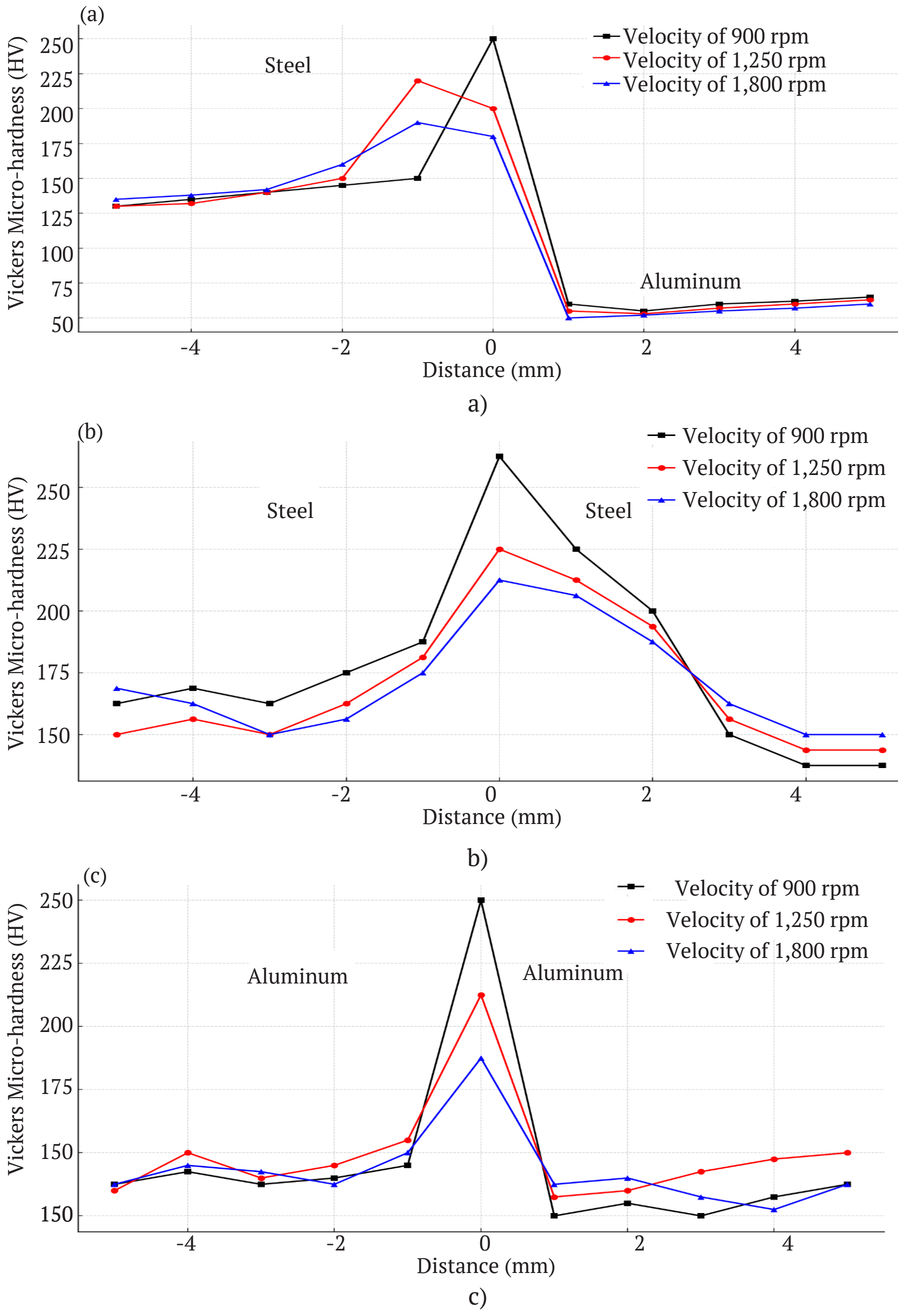

Figure 4. Microhardness test at three rotational speeds for
Note: a – steel-aluminium; b – steel-steel; c – aluminium-aluminium
Source: developed by the author

H. Miao *et al.* (2024) analysed factors influencing fatigue life in linear friction welded (LFW) joints of low-carbon steel, finding that fatigue life is controlled by stress concentration, weld toe geometry, residual stress, and microstructural evolution. They emphasised the importance of post-oscillation pressure in improving mechanical performance H. Miao *et al.* (2023) investigated fatigue strength improvement through pressurisation after oscillation, highlighting its positive effects on joint properties. The two studies are relevant to this study due to their identification of spindle speed as an important variable affecting elastic resistance, hardness and micro-structure. The results from the current study show that higher spindle speeds (i.e., 1,800 RPM) will reduce microstructural hardness and resistance while lower spindle speeds (i.e., 1,250 RPM) produce the most favourable mechanical properties. The studies provide further justification for the need to optimise process parameters to achieve welds with good mechanical properties, durability and surface finish. P. Geng *et al.* (2021) performed computational models to investigate plastic deformation and interfacial self-cleaning of the weld zone in linear friction welding of super alloys. As a result, they were able to develop a greater understanding of the mechanisms involved in producing micro structural changes and the joint strength in terms of the optimisation of processing parameters including weld speed and pressure. They found that plastic deformation and heat generated during the welding process have a great impact on the weld interface quality and therefore a major factor to be considered when optimising process parameters to achieve superior mechanical properties. Similar to the conclusions made by H. Miao *et al.* (2024; 2023), the study showed that the quality of the weld interface was primarily affected by heat input and plastic deformation which is a critical aspect in producing strong and defect free welds. H. Benkherbache *et al.* (2020), investigated the mechanical behaviour properties of a parts joined (similar and dissimilar) through the process of RFW, emphasising the criticality of thermal conditions and welding parameters for the microstructure and weld properties. The authors studied the heat generated during the process and how it affected the inter-metallic compounds (IMC's) in the case of dissimilar joint types such as steel-aluminium; they concluded that an increase in heat input results in a coarse-grained structure, micro-structurally softer, and lower hardness. This is consistent with the current research study, which demonstrated that an increase in heat input will have a negative effect on weld quality. In addition, C. Saib *et al.* (2025) performed a thermal, metallurgical, and mechanical analysis of single pass INC 738 welded parts and emphasised the influence of heat input on the formation of intermetallic phases, which may result in reduced weld strength. The conclusions from their study are consistent with those presented in this paper, and further emphasise the need to optimise the thermal conditions for achieving strong, defect free joints.

E. Maleki *et al.* (2021) illustrated the effects on the fatigue strength of welded steel caused by shot peening, and showed the effect on residual stresses in AISI 1060 Steel. Based upon the results of their study, shot peening was shown to have an impact on the residual stress state of weldments, to increase the fatigue strength, and to lower the probability of crack initiation, which are consistent with the stress relaxation associated with high speed friction welding. The thermal softening that takes place at high rotational speeds will also cause the elastic resistance and hardness to be lowered through stress relaxation mechanisms; as was determined in a study by H. Li *et al.* (2023) who analysed the effects of residual stress relaxation of a EA4T axle steel treated with ultrasonic surface rolling on the corrosion bending fatigue resistance of the steel. The study determined that the effects of residual stress relaxation were beneficial for improving the corrosion and fatigue resistance of the steel, similar to the study currently being discussed, which states that the thermal softening that occurs at high rotational speeds will lower the elastic resistance of the steel. Both of these studies emphasised the importance of controlling the thermal input during the manufacturing process to produce materials with long-term performance. X. Yang *et al.* (2025) have investigated the interrelation between the initial microstructure of GH4169 Superalloy weldments produced by linear friction welding and the mechanical properties and corrosion behaviour of these weldments. They determined that both thermal softening and microstructure modification affect the physical properties of the material, as was shown by the study and the effects of higher rotational speed to cause an excess of heat into the weld causing a loss of hardness due to microstructure softening and elastic resistance. In a study regarding low-temperature friction stir welding of TA5 titanium alloy joint microstructural development and mechanical behaviour, Y. Su *et al.* (2025) examined the effect of different cooling rates. The study demonstrated that the quality of the weld will be affected by the temperature of the weld, as stated by this study's results. A study showed that too much heat into the weld caused microstructural changes to the metal, reducing its strength and hardness. Therefore, thermal softening and stress relaxation occur at high spindle speed to produce the mechanical properties of the weld.

CONCLUSIONS

This research has shown that RFW is a viable and reliable solid state welding method for both similar and dissimilar metals provided that optimal processing conditions have been achieved. NDE tests using ultrasonic techniques confirmed the formation of defect free welds and thus, the structural integrity and metallurgical soundness of the weld regions. Based on this research it can be concluded that the spindle speed is the major control variable for determining the thermal energy transferred into the workpiece during RFW, as well as the resultant microstructures formed and the mechanical behaviour of the weldments. For example, increasing the rotational speed from 900 to 1800 rpm resulted in a decrease in elastic resistance in the weld region that can be attributed to over heating, thermal softening and undesirable microstructural changes. Conversely, the intermediate speed of 1250 rpm produced the best thermo-mechanical balance producing the best weld quality and mechanical performance. In addition, based on the mechanical testing, it was determined that the mechanical behaviour of the welded joints were dependent on the base metal composition. Welded steel to steel specimens had the best mechanical behaviour (i.e., the highest tensile strength and hardness), and this was attributed to the good plastic flow, fine microstructure and strong metallurgical bonding in the weld region. Aluminium to aluminium welded joints had the poorest mechanical performance, primarily due to grain growth and thermal softening in the weld region. Finally, steel to aluminium dissimilar welded joints had mechanical properties between those of the other two sets of specimens and had localised hardness peaks formed at the weld interface as a result of the formation of intermetallic compounds (IMCs). Therefore, the mechanical behaviour of these weldments were the result of the complex interactions between diffusion, heat input and phase transformations.

Overall, the results provide strong evidence that rotary friction welding (RFW) is an efficient and robust industrial weld process that can create high integrity welds in various material configurations; however, the study provides clear evidence that optimising the RFW process; especially the rotational speed will be required to prevent excessive thermal input and produce uniform microstructures as well as superior mechanical properties. Future studies should focus on a quantitative residual stress analysis, detailed characterisation of intermetallic phases present within RFW joints, as well as evaluating fatigue and fracture properties of both similar and dissimilar RFW joints. In addition, integrating numerical thermo-mechanical modelling with experimental validation would enable predictive optimisation of welding parameters for advanced structural and multi-material engineering applications.

ACKNOWLEDGEMENTS

None.

FUNDING

None.

CONFLICT OF INTEREST

None.

REFERENCES

[1] Ariyansah, R., Prabowo, A.R., Muhayat, N., Nugroho, B.A., & Triyono. (2025). The role of pressure in improving the properties of friction welded aluminum-copper dissimilar joints. *Journal of Advanced Joining Processes,* 12, article number 100329. doi: 10.1016/j.jajp.2025.100329.

[2] ASTM International. (2025). *ASTM E18-25: Standard test methods for Rockwell hardness of metallic materials*. West Conshohocken, PA: ASTM International. doi: 10.1520/E0018-25.

[3] Benkherbache, H., Amroune, S., Zaoui, M., Mohamad, B., Silema, M., & Saidani, H. (2020). Characterization and mechanical behaviour of similar and dissimilar parts joined by rotary friction welding. *Engineering Solid Mechanics,* 9(1), 23-30. doi: 10.5267/j.esm.2020.6.002.

[4] Chatha, J.S., Handa, A., & Bedi, T.S. (2021). Strength analysis of rotary friction welded joints of dissimilar steel grades. *Materials Today: Proceedings,* 38, 242-247. doi: 10.1016/j.matpr.2020.07.090.

[5] Farbakhti, M., Elmi Hosseini, S.R., Mousavi Mohammadi, S.A., Sadatabhari, S., Yuan-ming, H., & Li, R. (2025). Similar and dissimilar rotary friction welding of steels: A review of microstructural evolution and mechanical properties. *Journal of Materials Research and Technology,* 36, 8777-8803. doi: 10.1016/j.jmrt.2025.05.079.

[6] Gangil, N., Mishra, A., Lone, N.F., Bajaj, D., Chen, D., Haider, J., Chen, X., Konovalov, S., & Siddiquee, A.N. (2025). Linear friction welding of similar and dissimilar materials: A review. *Metals and Materials International,* 31(1), 1-21. doi: 10.1007/s12540-024-01738-1.

[7] Geng, P., Qin, G., Ma, H., Zhou, J., Zhang, C., & Ma, N. (2021). Numerical modelling on the plastic flow and interfacial self-cleaning in linear friction welding of superalloys. *Journal of Materials Processing Technology*, 296, article number 117198. doi: 10.1016/j.jmatprotec.2021.117198.

[8] Ghari, H., Taherizadeh, A., Sadeghian, B., Sadeghi, B., & Cavaliere, P. (2024). Metallurgical characteristics of aluminum-steel joints manufactured by rotary friction welding: A review and statistical analysis. *Journal of Materials Research and Technology*, 30, 2520-2550. doi: 10.1016/j.jmrt.2024.03.089.

[9] Gotawala, N., & Shrivastava, A. (2021). Investigation of interface microstructure and mechanical properties of rotatory friction welded dissimilar aluminum-steel joints. *Materials Science and Engineering: A,* 825, article number 141900. doi: 10.1016/j.msea.2021.141900.

[10] Kulkarni, V.V., & Kulkarni, P.C. (2021). Experimental analysis of rotary friction joining process by EN1A bright mild steel under normal air and wet environment condition. *Materials Today: Proceedings,* 46, 6501-6506. doi: 10.1016/j.matpr.2021.03.690.

[11] Li, H., Zhang, J., Ao, N., Xu, J., & Ji, D. (2023). Influence of residual stress and its relaxation on the corrosion bending fatigue resistance of EA4T axle steel treated by ultrasonic surface rolling. *International Journal of Fatigue,* 170, article number 107561. doi: 10.1016/j.ijfatigue.2023.107561.

[12] Malau, L.F., Ilman, M.N., & Sasmito, A. (2025). Effect of welding time on microstructure and mechanical properties of rotary friction weld joints of AA6061. In A. El Kharbachi, I.D. Wijayanti, P. Suwarta & I. Tolj (Eds.), *Smart innovation in mechanical engineering* (pp. 249-258). Singapore: Springer Nature. doi: 10.1007/978-981-97-7898-0_28.

[13] Maleki, E., Farrahi, G.H., Reza Kashyzadeh, K., Unal, O., Gugaliano, M., & Bagherifard, S. (2021). Effects of conventional and severe shot peening on residual stress and fatigue strength of steel AISI 1060 and residual stress relaxation due to fatigue loading: Experimental and numerical simulation. *Metals and Materials International,* 27(8), 2575-2591. doi: 10.1007/s12540-020-00890-8.

[14] Miao, H., Tsutsumi, S., Yamashita, T., Morisada, Y., & Fujii, H. (2023). Fatigue strength improvement of linear friction welded butt joints of low carbon steel by pressurizing after oscillation. *Journal of Manufacturing Processes,* 102, 795-805. doi: 10.1016/j.jmapro.2023.08.004.

[15] Miao, H., Yamashita, T., Tsutsumi, S., Morisada, Y., & Fujii, H. (2024). Multiple analyses of factors influencing fatigue life of linear friction welded low carbon steel. *Journal of Advanced Joining Processes,* 9, article number 100201. doi: 10.1016/j.jajp.2024.100201.

[16] Saib, C., Amroune, S., Chebbah, M.-S., Belaadi, A., Zergane, S., & Mohamad, B. (2025). Thermal, metallurgical, and mechanical analysis of single-pass INC 738 welded parts. *Metals*, 15(6), article number 679. doi: 10.3390/met15060679.

[17] Su, Y., Zhou, M., Li, W., Yang, X., Shi, Q., Xiong, Y., Wang, P., & Chen, G. (2025). Microstructural evolution and mechanical behavior of TA5 titanium alloy joint in low-temperature friction stir welding with various cooling rates. *Engineering Failure Analysis,* 176, article number 109667. doi: 10.1016/j.engfailanal.2025.109667.

[18] Wang, J., Fu, X., Zhang, L., Zhang, Z., Liu, J., & Chen, S. (2021). A short review on laser welding/brazing of aluminum alloy to steel. *The International Journal of Advanced Manufacturing Technology,* 112, 2399-2411. doi: 10.1007/s00170-021-06607-4.

[19] Xu, X., You, G., Ding, Y., Tong, X., Zai, L., & Liu, Q. (2020). Microstructure and mechanical properties of inertia friction welded joints between high-strength low-alloy steel and medium carbon steel. *Journal of Materials Processing Technology,* 286, article number 116811. doi: 10.1016/j.jmatprotec.2020.116811.

[20] Yang, X., Meng, T., Su, Y., Xu, R., Guo, Z., Xu, Y., Ma, T., & Li, W. (2025). Effect of initial microstructure on performance and corrosion behavior of GH4169 superalloy joint produced by linear friction welding. *Chinese Journal of Aeronautics,* 38(3), article number 103226. doi: 10.1016/j.cja.2024.09.002.

Мотанна Таха Мохаммед Фаттах Ага

Факультет сільського господарства
Університет Аль-Касім Грін
51001, м. Вавилон, Ірак
https://orcid.org/0000-0002-7957-3404

Оцінка термо-механічної реакції компонентів за допомогою техніки ротаційного тертя при зварюванні

Анотація. Ротаційне термове зварювання (RFW) є одним з найважливіших процесів для з’єднання металів, як однакових, так і різних. RFW здобуло популярність серед багатьох виробничих секторів, оскільки зменшує теплові деформації, зменшує площу термічно уражених зон, забезпечує підвищені темпи виробництва та усуває потребу у заповнювальних матеріалах. Основною метою цього дослідження були механічні властивості зварних швів, з акцентом на взаємозв’язок швидкості шпинделя з якістю зварних швів для трьох різних типів матеріалів, що з’єднуються: алюміній-алюміній, сталь-алюміній та сталь-сталь. Ці зварювання були виготовлені за допомогою техніки ротаційного тертя на токарному верстаті. Проведено випробування на розтягування для оцінки того, як зварювання витримує навантаження. Здійснено ультразвукові перевірки для виявлення тріщин або пор в зварних швах. Проведено мікрометричні вимірювання для оцінки зони зварювання. Тести на твердість були проведені для визначення ступеня опору матеріалу. Нарешті, була проведена металографічна оцінка для дослідження мікроструктурних характеристик зварних швів. Тести показали, що з підвищенням швидкості шпинделя знижувався еластичний опір зварних швів. Було встановлено, що ця втрата еластичного опору виникає через високу температуру, яка утворюється при високих швидкостях шпинделя, що призводить до пом'якшення мікроструктури. Оптимальна механічна продуктивність була досягнута при швидкості шпинделя 1 250 об/хв, що забезпечило найвищий рівень механічних властивостей, таких як міцність і твердість. Крім того, через ультразвукові тести було підтверджено, що всі зварні шви, отримані за допомогою RFW, були повністю без дефектів. Отже, ці результати чітко демонструють, що RFW може створювати зварні шви з високими механічними властивостями та без дефектів, якщо існують оптимальні умови процесу, особливо якщо швидкість шпинделя налаштована відповідно до матеріалів

Ключові слова: з’єднання у твердому стані; термо-механічний аналіз; зона термічного впливу; металографічна характеристика; зварювання різнорідних металів

Machinery & Energetics
Vol. 17, No. 1. 2026

Journal homepage:
https://technicalscience.com.ua/en

UDC 621.3.013:004.942
DOI: 10.31548/machinery/1.2026.28

ISSN 2663-1334
e-ISSN 2663-1342

Larisa Vakhonina
PhD in Physical and Mathematical Sciences, Associate Professor
Mykolaiv National Agrarian University
54008, 9 Georgiy Gongadze Str., Mykolaiv, Ukraine
https://orcid.org/0000-0002-1668-2275

Volodymyr Martynenko*
PhD in Technical Sciences, Associate Professor
Mykolaiv National Agrarian University
54008, 9 Georgiy Gongadze Str., Mykolaiv, Ukraine
https://orcid.org/0000-0003-4067-3640

Andrii Rudenko
Postraduate Student, Assistant
Mykolaiv National Agrarian University
54008, 9 Georgiy Gongadze Str., Mykolaiv, Ukraine
https://orcid.org/0000-0002-5103-6412

Vitalii Mardziavko
Postraduate Student, Assistant
Mykolaiv National Agrarian University
54008, 9 Georgiy Gongadze Str., Mykolaiv, Ukraine
https://orcid.org/0000-0001-7327-9215

Integration of CAD electrical machines and apparatuses with multiphysical modelling: An approach to matching electromagnetic and thermal models

Abstract. Isolated use of electromagnetic or thermal calculations in the design of electrical machines and apparatuses is a significant source of engineering errors since operating modes are formed by interrelated field and thermal processes. The purpose of the study was to substantiate and formalise the approach to integrating automated design with multiphysical modelling by matching electromagnetic and thermal models in a single parametric controlled circuit. The methodology was based on normatively consistent modes, cooling conditions, and temperature limits with two-way iterative coupling and spatially consistent transfer of losses to a thermal model with temperature correction of material properties. As a result, a common parametric frame of inputs is formed, which provides a consistent interpretation of load, cooling, temperature acceptability and energy efficiency. A formalised two-way circuit with convergence criteria provided reproducible stabilisation of temperature maxima and total losses. It is shown that spatial mapping of composite losses preserves local overheating zones, while their reduced transfer smooths out the temperature field. Consistent modelling established the heating domain stratification: in the windings about 130-140°C, in the magnetic circuit 105-115°C, in the housing 85-95°C, in the cooling zone 60-70°C. Temperature corrections of electrical and magnetic parameters substantially change the distribution of losses, primarily due to an increase in the resistance of conductors. A comparison of four matching schemes in 40 scenarios showed a convergence of 26 out of 40 for one-way binding to 38 out of 40 for the integrated solution; a

Article's History: Received:13.10.2025; Revised: 14.01.2026; Accepted: 26.02.2026; Published: 30.03.2026.

Suggested Citation:
Vakhonina, L., Martynenko, V., Rudenko, A., & Mardziavko, V. (2026). Integration of CAD electrical machines and apparatuses with multiphysical modelling: An approach to matching electromagnetic and thermal models. *Machinery & Energetics,* 17(1), 28-42. doi: 10.31548/machinery/1.2026.28.

*Corresponding author

two-way iterative scheme provided 36 out of 40 with stabilisation in 4-7 cycles, while step-by-step co-modelling required 6-12 exchanges. Practical importance lies in the possibility of direct use of the approach to improve the accuracy of thermal checks, select load modes, and optimise design solutions for electrical products

Keywords: temperature field; two-way circuit; volume source; co-simulation; heat sources; vortex losses

INTRODUCTION

The design of electrical machines and apparatuses increasingly requires an integrated approach since the design of the product, operating modes and operational limitations are formed by interrelated processes, which is advisable to analyse within a single digital design environment. Modern computer-aided design (CAD) of electrical products are increasingly combined with numerical field and multiphysical approaches, which allows simultaneously considering electromagnetic and thermal processes and their mutual influence. For electrical machines and apparatuses, such integration is critical since electromagnetic losses are the primary source of heat generation, the temperature field changes the electrophysical and magnetic parameters of materials, and therefore affects the performance, efficiency and service life of the product. In this context, the results of O. Kostin *et al*. (2022) demonstrated that the analysis of the regime stability of electrical processes requires a formalised approach to the estimation of dynamic modes since even local process instabilities can determine the limits of permissible operating modes and the requirements for calculated reproducibility. The authors stressed that the correctness of engineering conclusions is achieved only if a methodically consistent description of the mode parameters and stability criteria can be included in the digital design circuit. The effect of the electromagnetic system configuration on active losses in static electromagnetic devices is highlighted by O. Sadovoy *et al*. (2022), which showed the dependence of the loss level on the structural organisation of the magnetic path and excitation parameters. Their results indicate that electromagnetic losses should be described as a spatially and regime-dependent value suitable for further transfer to the thermal model as distributed heat sources. The development of the concept of digital doubles of technical objects forms the basis for matching simulation models with operational monitoring data. V. Pliuhin *et al*. (2024) described the implementation features of local and remote digital doubles, emphasising the role of integrating computational models, sensor data, and communication infrastructure to recreate the state of an object over time. This logic is fundamental for electrical machines and apparatuses, as it allows considering electromagnetic and thermal sub-models as interrelated components of a single digital representation of the product. Deepening this approach through algorithmic support and high-performance computing in automated design systems of electrical machines is presented by V. Pliuhin *et al*. (2025), who showed that combining machine learning methods with calculation modules enhances parametric optimisation capabilities and accelerates multi-dimensional multiphysical design iterations.

In applied works on electrical machines, the integration of electromagnetic and thermal analysis is considered as a necessary element of correct design. A. Młot *et al*. (2022) combined electromagnetic analysis, efficiency map, and thermal calculation for an 80 kW Interior Permanent Magnet motor, showing that temperature constraints and losses determine realistic operating modes and permissible loads. Similarly, J.F.D. Santos *et al*. (2022) demonstrated a digital twin induction motor approach using thermomagnetic finite element analysis, in which electromagnetic parameters and heating are consistent as interdependent computational domains for state monitoring and prediction. Methodological generalisations in the field of design automation emphasise that multidisciplinary integration into CAD is increasingly implemented as a link between electromagnetic, thermal, and mechanical sub-models in a single optimisation circuit. N. Umland *et al*. (2023), in a systematic review, demonstrate that the design automation of electric motors is based on the transition from "sequential" calculations to consistent operating flows, where loss sources, temperature limits, and efficiency criteria are accounted for together. An overview and case study of thermal design of cooling systems for a commercial synchronous motor with permanent magnets is provided by H.G. Usca-Gomez *et al*. (2025), which demonstrated the practical significance of integrating modelling, simulation, and thermal analysis for selecting rational cooling solutions and interpreting load modes. An alternative multiphysical methodology for strongly coupled electro-magneto-mechanical problems was proposed by F.M. Reato *et al*. (2023), justifying the feasibility of consistent numerical schemes in cases where electromagnetic effects give rise to mechanical and thermal effects and require joint formulation.

Thereby, applied descriptions of the use of Computer-Aided Design (CAD) electric drives using Finite Element Analysis (FEA) show that the technical integration of tools is already achievable, but the methodological scheme for matching electromagnetic and thermal models within a single parametrically controlled design circuit remains insufficiently formalised for reproducible applications in a wide class of electrical machines and apparatuses. A study by M. Manka *et al*. (2023) highlights the practical role of FEA instruments in the CAD design of electric drives, which actualises the need for a well-defined circuit for transferring electromagnetic losses to the thermal setting and returning temperature corrections to the electromagnetic model as a standard engineering procedure. A consistent analysis of these sources confirms that the effective integration of CAD with multiphysical modelling should be based on a formalised mechanism for two-way binding of electromagnetic and thermal sub-models, which provides a reproducible engineering interpretation of losses, temperature limits, and efficiency indicators in a single project cycle.

The study aimed to provide theoretical substantiation and methodological formalisation of the approach to integrating CAD of electrical machines and apparatuses with multiphysical modelling based on the Coordination of electromagnetic and thermal models in a single parametrically controlled design circuit. The main objectives of the study were: determine the principles and structure of two-way binding of electromagnetic and thermal sub-models through the chain "losses → heat sources → temperature field → temperature parameter corrections"; systematise the methods of model matching in the CAD environment (sequential-iterative binding, co-simulation, integrated multiphysical calculation) and establish the conditions for their correct application for electrical machines and apparatuses; clarify the set of design parameters and criteria that provide an engineering reproducible interpretation of the results of electromagnetic-thermal modelling in the problems of design optimisation, loss reduction and compliance with temperature restrictions.

MATERIALS AND METHODS

The study was performed as a theoretical one with elements of methodological formalisation and was aimed at building a reproducible approach to the coordination of electromagnetic and thermal models in the digital design circuit of automated design systems for electrical machines and apparatuses. The basic source of requirements for cooling methods and a unified description of heat sink schemes for rotating electric machines was the IEC 60034-6:1991 (1991), which was used for the normative correct setting of the IC code and matching the boundary conditions of thermal analysis with the type of cooling that determines the permissible temperature rises and the nature of heat exchange. Since the correct comparison of electromagnetic and thermal results depends on a consistent description of operating modes and passport characteristics, the regulatory basis for parameterisation of modes and operating indicators was formed by IEC 60034-1:2022 (2022), which provided uniform rules for interpreting nominal modes, load states, and related restrictions. IEC 60034-18-1:2022 (2022) provided a documentary basis for determining the requirements for insulation systems and the logic of their functional assessment for methodically correct inclusion of temperature restrictions in the design circuit and their connection with the stability and resource of electrical machines, which was used as a reference for substantiating permissible temperature limits and criteria for the acceptability of thermal regimes during engineering interpretation temperature fields. Since the key link between electromagnetic and thermal sub-models is the transfer of electromagnetic losses in the form of thermal sources, the basic regulatory source of methods for determining losses and efficiency from tests was IEC 60034-2-1:2024 (2024), which is used to unify the interpretation of composite losses to be reflected in the electromagnetic model and transferred to the heat setting.

IEC 60034-30-1:2025 (2025) was applied to ensure comparability of design solutions in terms of energy efficiency and to correctly assign results to efficiency classes, which was used as a framework for engineering interpretation of the impact of model matching on losses and efficiency improvement potential within the International Efficiency (IE) standard classification. The object of methodological analysis was generalised parametric models of electrical machines and electromagnetic apparatuses presented in the form of CAD structures with related material and mode parameters. The consideration covered geometric representations of the active part (magnetic circuit, windings, conductors, air gaps, structural shells) and sets of temperature-dependent electrophysical and thermophysical characteristics of materials necessary for the implementation of two-way binding of sub-models. For comparative analysis, four classes of calculation and model matching scenarios ($n = 40$) were formed, which differed in the structure of binding of electromagnetic and thermal sub-models: one-way schemes for transferring losses to a thermal problem; sequential-iterative schemes with temperature feedback; co-simulation statements for variable modes; integrated multiphysical statements with simultaneous problem solving. A set of scenarios was based on a partial multi-factor variation plan aimed at representative and uniform coverage of the parametric space without completely iterating through all possible combinations. There were six groups of factors that determine the electromagnetic-thermal interaction:

- the type of cooling system (two levels, in particular, different International Cooling (IC) codes);
- the convective heat transfer coefficient h (three levels within the characteristic engineering range for air cooling);
- thermal contact supports between structural layers (two levels-nominal and elevated);
- the temperature coefficient of electrical resistance of windings (two levels within the standard permissible deviations for copper);
- the load mode and power frequency (three levels: partial, nominal, and overload modes);
- the material of the magnetic circuit (two options with different specific losses).

Given the multidimensional nature of the problem, a complete factor plan would result in an excessive sample size, so a reduced balanced selection of 10 representative combinations was applied, including extreme and central levels of factors and ensuring that individual variables did not dominate. Each of these combinations was implemented in four matching schemes, which formed a common set of 40 scenarios. This structure of the research plan allowed correctly separating the influence of physical parameters from the influence of the binding algorithm and ensuring the methodological purity of the comparative analysis.

The methodological part was based on the system, structural-functional, and parametric analysis of multiphysical models and was implemented as a formalised two-way computational circuit "electromagnetic losses → equivalent heat sources → temperature field → temperature parameter corrections → refined electromagnetic calculation" with the specified convergence criteria. Within this circuit, the electromagnetic results were interpreted not as isolated fields but as design input data for a thermal sub-model: loss mapping was performed in a spatially distributed form with reduction to bulk heat sources and with control of the correctness of transfer between grids/geometric domains. Feedback was implemented through the return of the temperature field to the electromagnetic setting by updating the temperature-dependent properties of materials and winding parameters, which allowed reproducing the physically correct interaction "heating → parameter change → loss change" within the iterative process. The electromagnetic sub-model was considered in a field quasi-stationary formulation with the determination of distributed losses in conductors and magnetic materials, including Joule losses in windings and composite losses in the magnetic circuit, as well as, if necessary, additional vortex losses in structural elements.

The thermal sub-model was formed as a problem of heat transfer considering thermal conductivity in solids, convective heat exchange at boundaries, and contact thermal resistances in multilayer structures; the problem of boundary conditions provided for parameterisation of heat transfer coefficients and description of cooling paths as engineering heat exchange conditions. Parametric coupling was performed due to the temperature dependences of the electrical resistance of the conductors, specific losses, and magnetic characteristics, which ensured a consistent update of losses after each cycle of thermal calculation. Iterative matching was completed when convergence was achieved according to the stabilisation criteria of maximum temperatures and total losses, and in the absence of significant changes in critical local heating zones (winding parts, zones of increased losses in steel, areas of contact with the heat sink). For comparative evaluation of binding schemes, the convergence stability under changing cooling boundary conditions, the sensitivity of temperature maxima to changes in thermal resistances of layers, and the consistency of the energy balance between sub-models were additionally analysed. Numerical implementation of the generalised approach was performed in COMSOL Multiphysics 6.2, in Computer-Aided Design/Computer-Aided Engineering (CAD/CAE)-flow with heat exchange simulation in ANSYS Fluent, with specialised parameterisation of electrical machines in ANSYS Motor-CAD, and parametric run automation and post-processing – in MATLAB/Simulink R2024a and Python 3.12. The applied method provided reproducible and normatively interpreted matching of electromagnetic and thermal calculations in the CAD circuit, allowing comparing binding schemes in terms of convergence, sensitivity to limiting cooling conditions, and suitability for design optimisation accounting for temperature restrictions and losses.

RESULTS

Regulatory and parametric framework for matching electromagnetic and thermal sub-models

In the process of methodological formalisation of the initial conditions of multiphysical coordination, a systematic comparison of regulatory requirements for operating modes, cooling schemes, permissible temperature limits, and energy efficiency indicators was conducted. Based on this comparison, a consistent set of parameters is formed, which is used as a common input frame for electromagnetic and thermal statements, an interpretive basis for transferring losses to thermal sources and checking the permissibility of temperature regimes. The analysis of the generated parametric set revealed that the reproducibility of electromagnetic-thermal modelling in the design CAD circuit is determined precisely by the unified standard setting of load modes, cooling IC codes, insulation temperature limits, and interpretive efficiency criteria. Matching sub-models requires treating these values as interrelated computational constraints, rather than as independent reference characteristics (Table 1).

Table 1. Normatively agreed parameters of modes, cooling and temperature limits for electromagnetic-thermal modelling

Standard parameter block	What exactly is unified in the project circuit	Role in the electromagnetic sub-model	Role in the thermal sub-model	Engineering result of approval
Operating modes and passport parameterisation	Nominal mode, load conditions, interpretation of "rating and performance" as a single basis for comparing scenarios	Fixes basic operating states for calculating fields and losses (load/current/mode matching)	Provides a correct comparison of temperature fields with exactly the mode for which passport restrictions are defined	The only interpretation of "mode → loss → heat load", which eliminates discrepancies between the "electric" and "thermal" descriptions of the machine condition
Cooling type and IC code (cooling methods)	IC code as a standardised description of the heat sink scheme and heat exchange conditions	Sets an engineering-correct framework of assumptions for addressing thermal limitations in the selection of permissible loads and scenarios	Defines the type of boundary conditions: the nature of convection, the organisation of heat exchange, the consistency of "cooling – permissible temperature rise"	Normatively correct setting of the boundary conditions of the thermal problem, compatible with the passport mode and design type

Continued Table 1.

Standard parameter block	What exactly is unified in the project circuit	Role in the electromagnetic sub-model	Role in the thermal sub-model	Engineering result of approval
Temperature limits of thermal regime acceptability due to insulation requirements	Logic of functional evaluation of the insulation system and permissible temperature limits as an acceptability criterion	Determines the permissible temperature limits within which electromagnetic parameters are considered acceptable after temperature correction	Sets the temperature field acceptability criterion: T_{max} control in critical zones (winding/insulation)	Linking the thermal result to a clear "acceptable/ unacceptable" criterion in terms of insulation temperature endurance
Energy efficiency and IE classes as an interpretive framework	IE energy efficiency classes as a standardised field for interpreting the impact of losses and modes	Allows interpreting total losses and their changes when matching models in terms of energy efficiency	Indirectly fixes the requirement for thermal mode due to the permissibility of losses and operating states for a given IE class	Conversion of coordination results from the "temperature/loss" level to the standard comparable energy efficiency level for project solutions
Consistent set of output parameters for reproducible scripts (n-script input frame)	Uniform input assumptions for comparing matching schemes: mode → IC code → temperature limits → performance interpretation	Fixes comparable conditions for calculating losses between scenarios	Fixes comparable cooling conditions and temperature acceptability criteria between scenarios	Ensures that the results of different binding schemes are correctly compared as obtained under the same regulatory and parametric framework

Source: compiled by the authors according to IEC 60034-6:1991 (1991), IEC 60034-1:2022 (2022), IEC 60034-18-1:2022 (2022), IEC 60034-2-1:2024 (2024), IEC 60034-30-1:2025 (2025)

The analysis of the parameters summarised in Table 1 showed that the normative characteristics within the electromagnetic-thermal agreement perform the function of a common "parametric interface" between sub-models, setting the same logic for describing the mode, cooling, temperature acceptability, and energy efficiency. The operating modes unified in accordance with IEC 60034-1:2022 (2022) define the design states for which electromagnetic losses are formed as a mode-dependent value suitable for transfer to a thermal setting. The cooling IC code specified in IEC 60034-6:1991 (1991) specifies the type and structure of the heat sink as a normatively correct basis for forming the boundary conditions of heat exchange, which directly affects the permissible temperature rises and the nature of the temperature field. Temperature limits of acceptability, linked to the requirements for functional evaluation of insulation systems according to IEC 60034-18-1:2022 (2022), translate the thermal result from a descriptive level to a criterion verification level, as they allow temperature maxima to be interpreted not simply as calculated values, but as threshold limits that determine the acceptability of a design solution. The inclusion of energy efficiency classes according to IEC 60034-30-1:2025 (2025) provides a standardised context for interpreting the impact of model matching on losses, which allows comparing alternatives both for local temperature peaks and integral energy performance within the IE classification. The consistent application of these parameters eliminates the typical methodological discrepancy between sub-models when electromagnetic losses are calculated for conditions that do not correspond to the actual type of cooling, or when the thermal field is estimated without a formalised tolerance criterion from the point of view of insulation and passport regime. As a result, the formed normative-parametric framework provides reproducible initial conditions for further two-way binding along the chain "losses → heat sources → temperature field → temperature parameter corrections" since it makes unambiguous both the method of setting the mode and cooling, and the criteria for the acceptability of the obtained temperature and efficiency results.

Formalised two-way computational model matching circuit

In the course of the study, a generalised two-way computational circuit for matching electromagnetic and thermal sub-models is constructed, in which both calculations are combined by an iterative cycle with controlled feedback (Fig. 1). Within this circuit, standardised data exchange points are defined: transfer of distributed losses from the electromagnetic problem to the thermal problem in the form of equivalent volumetric heat sources and return of the temperature field to the electromagnetic setting through updating the temperature-dependent parameters of materials and windings. Parametric update rules and iterative process convergence criteria are formalised for each transfer point. Analysis of the obtained structure showed that reproducible matching in the CAD circuit requires not only the presence of two calculated domains but also a well-defined computational scheme of two-way binding with fixed data transfer points and formal conditions for completing iterations.

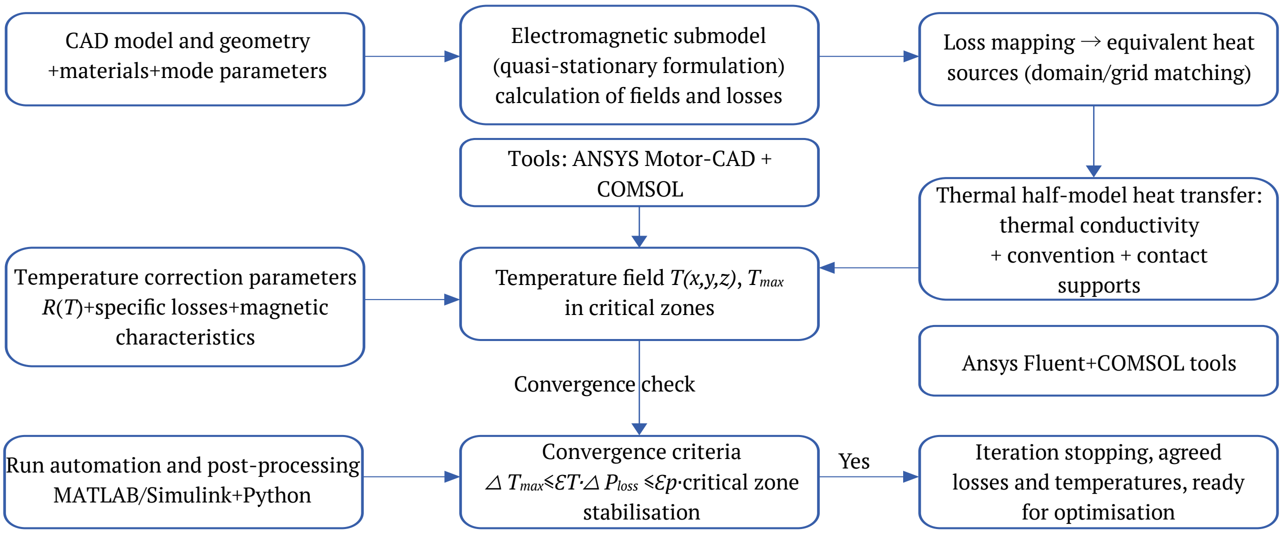

Figure 1. Formalised two-way scheme for matching electromagnetic and thermal sub-models in a CAD environment
Source: compiled by the authors according to the described computational scheme and matching procedures in COMSOL Multiphysics 6.2, ANSYS Fluent, ANSYS motor-CAD, MATLAB/Simulink R2024a

Figure 1 shows a block diagram of a two-way circuit in which the initial electromagnetic calculation forms a spatially distributed map of losses in conductors and magnetic materials. These losses go through the normalisation and spatial mapping stages and are converted into equivalent heat sources consistent with the geometric domains of the thermal model. After solving the heat transfer problem, a temperature field is formed with the allocation of local maxima and critical heating zones, which is then used for parametric updating of electrical resistance, specific losses, and magnetic characteristics. The updated set of parameters is returned to the electromagnetic sub-model, where an updated loss calculation is performed, after which the cycle is repeated. Analysis of the constructed circuit has shown that the fundamental condition for its reproducibility is not the fact of iterationism itself, but the formalisation of stopping criteria. The methodological scheme uses simultaneous stabilisation of three groups of indicators as convergence criteria: maximum temperatures in critical zones, total electromagnetic losses, and local loss densities in domains with increased heat dissipation. In particular, maximum temperatures in critical zones are considered stable if their change between iterations does not exceed ±2°C. The total losses are stabilised at a change of no more than ±1%, which corresponds, for example, to 2-5 W for a device with a total loss of about 500 W. Local loss densities in domains with increased heat dissipation are assumed to be stable when the deviation between iterations does not exceed ±2%, which is for a local density of 1.2 W/cm^3 corresponds to the limits of 0.024 W/cm^3. The use of such numerical thresholds provides methodically reproducible updating of electrophysical and thermal characteristics in a two-way electromagnetic-thermal circuit.

The circuit is considered convergent only if there are no changes in these metrics between adjacent iterations. In addition, it has been established that the formalised bilateral circuit is suitable for various coordination schemes – sequential-iterative, co-simulation, and integrated multiphysics – provided that the same data transfer points and convergence criteria are maintained. This ensures comparability of results between scenarios and allows interpreting differences as a consequence of the binding structure, rather than different rules for exchanging parameters. Summarising, the constructed formalised two-way computational circuit sets the reproducible algorithmic basis for matching electromagnetic and thermal sub-models, fixes data exchange interfaces, and criteria for completing iterations, and thereby translates multiphysical matching from the level of instrumental practice to the level of standardised engineering procedure.

Structuring of electromagnetic losses and rules for their transfer to thermal staging

Within the constructed computational circuit, the structuring of electromagnetic losses is performed with their formalised separation by physical nature, spatial localisation, and the method of transfer to thermal staging. Losses are interpreted as distributed energy sources to be reduced to consistent calculated domains of the thermal model with control of volume, material, and mode compliance. The basic groups of losses that are subject to mandatory mapping have been identified: Joule losses in windings, losses in the magnetic circuit (hysteresis and eddy current losses), additional load losses, and local eddy losses in structural elements. For each group, the conversion rule to the thermal equivalent is established – in the form of a volume or surface heat source – with the fixing of the calculated domain and the parameter transmitted to the thermal problem. A generalised correspondence between the components of losses, their physical nature, and the transfer rules is presented in Table 2.

Table 2. Correspondence of components of electromagnetic losses to types of heat sources and settlement domains

Component of electromagnetic losses	Physical mechanism	Primary calculation in the electromagnetic (EM) model	Type of heat source in a thermal sub-model	Spatial transfer domain	Thermal mapping rule
Joule losses in windings	Ohmic heating of conductors	Current density distribution and $R(T)$	Volumetric heat source	Winding volume	Integral losses are distributed over the volume of the conductor, considering the fill factor and the temperature dependence of the resistance
Losses in the steel of the magnetic circuit (hysteresis)	Magnetic hysteresis loop	Local specific losses in the core	Volumetric heat source	Slats/segments of the magnetic circuit	Specific losses are multiplied by the local volume of the domain linked to the material domain
Steel losses (eddy currents)	Induced currents in the core	Frequency-dependent losses	Volumetric heat source	Magnetic circuit	Mapping is performed on an element grid with aggregation into thermal subdomains
Additional load losses	Scattering, field harmonics	Balance/residual losses	Generalised volume source	Active part (consolidated domain)	Distributed proportionally to energy-loaded areas according to the accepted weighting rule
Local vortex losses in structural parts	Eddy currents	Local losses in detail	Local volume or surface source	Fasteners, screens, massive metal parts	Bound to the corresponding CAD domains as separate thermal regions
Surface losses from stray currents	Surface effect	Surface loss density	Surface heat load	Surfaces of the leading parts	Converted to the limit thermal condition (heat flux)

Source: compiled by the authors according to the rules for determining and interpreting losses in accordance with IEC 60034-2-1:2024 (2024) with implementation in COMSOL Multiphysics 6.2 and Ansys Motor-CAD

The generalised matching analysis in Table 2 showed that the key condition for correct transfer is domain-oriented mapping, where each loss component is passed not as a reduced number, but as a spatially bound distribution. This ensures consistency of the energy balance between sub-models and enables the correct reproduction of local temperature maxima in windings, zones of increased magnetic losses, and structural elements. Separately, it was identified that aggregated transfer of total losses without spatial decomposition leads to smoothing of the temperature field and loss of sensitivity of the model to design solutions for cooling. That is why the rule of mandatory decomposition of losses by domain is applied in the agreed circuit, followed by reduction to equivalent heat sources of a given type. As a result, the structuring of composite losses and the formalisation of the rules for their mapping provided a reproducible procedure for the transition from electromagnetic calculation to thermal setting, consistent with the normative interpretation of losses and suitable for a multi-criteria multiphysical design circuit.

Results of constructing the temperature field and identifying critical heating zones

Within the framework of a consistent electromagnetic-thermal formulation, temperature fields were constructed for all calculated scenarios. Analysis of the spatial temperature distribution showed stable structural inhomogeneity, which is determined not only by the level of total losses but also by the configuration of heat sink paths, the type of cooling, and the value of contact thermal resistances. Generalisation of the results of 40 scenarios showed that even at close integral loss values, temperature maxima are localised in different domains depending on the cooling IC code, convection parameters, and thermal interconnection of layers. This confirms the need for spatially consistent, rather than averaged, thermal analysis. Figure 2 shows a generalised map of temperature fields, where the average, maximum, and critical temperatures for the main structural domains are spatially compared: windings, magnetic core, housing, and cooling zones.

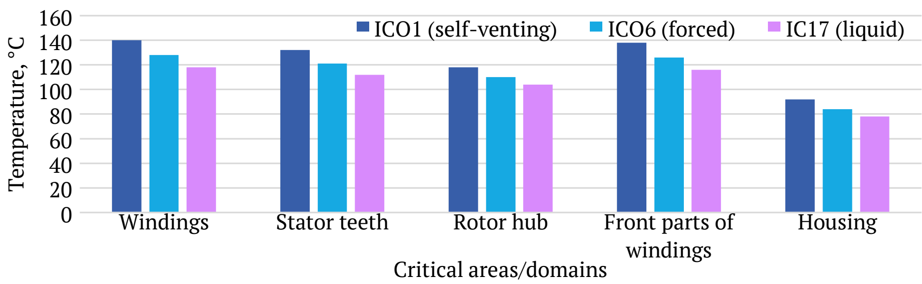

Figure 2. Generalised map of temperature fields and critical heating zones in a coordinated electromagnetic-thermal formulation

Source: compiled by the authors on the basis of a thermal sub-model of heat transfer with parameterisation of cooling conditions by IEC 60034-6:1991 (1991) with numerical implementation in Ansys Fluent and COMSOL Multiphysics 6.2

According to Figure 2, the highest temperatures are recorded in the windings: maximum ≈130°C, critical value ≈140°C, average ≈110°C, which forms the upper cluster and corresponds to the domain with the highest specific loss generation. Next in terms of heating level is the magnetic circuit: maximum ≈105°C, critical ≈115°C, average ≈90°C, i.e., lower than the windings, but higher than the housing. The housing is characterised by lower values: maximum ≈85°C, critical ≈95°C, and average ≈70°C, reflecting a more efficient heat sink. The lowest temperatures are observed in the cooling zone: maximum ≈60°C, critical ≈70°C, average ≈50°C, i.e., the lower limit of the temperature field, relative to which the heating gradient of other domains is formed. Generalisation of the results of temperature modelling confirmed that critical heating zones are scenario-dependent and should be determined in the coupled electromagnetic-thermal state since their position and intensity change after temperature correction of material parameters. This means that the engineering correct interpretation of thermal constraints and verification of permissible modes is possible only in an iterative two-way matching circuit, and the use of an isolated thermal estimate without updated losses leads to a shift in the assessment of risk zones.

Temperature-parametric feedback and refinement of the electromagnetic calculation

As part of the consistent electromagnetic-thermal analysis, the temperature field obtained at the previous iteration of the thermal calculation was used to update the temperature-dependent electrophysical and magnetic parameters in the corresponding calculated domains. A two-way binding circuit "temperature field → parameter correction → repeated electromagnetic calculation" was implemented, which specified the electrical resistivity of conductors, magnetic permeability, and specific losses in the magnetic circuit. Generalised temperature corrections of parameters and their impact on refined losses and performance characteristics are shown in Table 3.

Table 3. Temperature corrections of electrophysical and magnetic parameters and their impact on electromagnetic results

Parameter (notation)	Where it is used in the model	How it changes with temperature (qualitatively)	What corrects in the EM calculation	Expected direction of impact on losses/characteristics
Electrical resistance of the winding ($R_w(T)$)	Windings/conductors	Increases with increasing T	Joule loss $P_{Cu} = I^2R$; local heat sources in windings	Losses in copper ↑, winding temperature ↑, (efficiency)↓; at constant torque, current may increase in certain modes
Conductor resistivity ($p_e(T)$)	Conductors, conductive busbars	Increases with increasing T	Current distribution, current density J, ohmic losses	Ohmic losses↑, increasing the thermal load of conductor zones
Specific losses in steel ($P_{Fe}(T)$)	Magnetic circuit (yoke/prongs)	Temperature-dependent (often weak, but significant for modes/materials)	Hysteresis and eddy current losses; balance of steel losses	Changes in steel losses (often moderate), redistribution of heat sources in the magnetic circuit; risk of local maxima in areas of increased induction
Magnetic permeability/magnetisation curve ($\mu(T)$, B-H (T))	Magnetic circuit	Effective permeability may decrease; saturation occurs "earlier"	Operating point on B-H, induction B, flow coupling, field distribution	Possible reduction of torque/EMF or the need for more current; indirectly may increase losses in copper
Residual induction/coercive force of a permanent magnet, ($Br(T)$, $Hc(T)$) if there are permanent magnets	Rotor/magnets	Usually decreases with increasing T	Main flux from a permanent magnet, EMF, moment constant	Flow ↓ → moment/EMF ↓, to maintain the mode, the current increases → P_{Cu} ↑; additionally, the risks of overheating of magnets increase
Equivalent conductivity/loss in structural elements ($P_{add}(T)$)	Covers, screens, fasteners (in the presence of vortex losses)	Indirectly depends on $\rho(T)$	Additional vortex losses in metal parts	Additional losses may vary; affect local heating of structural elements
Insulation system temperature limits (T_{lim})	Windings/insulation	The norm sets the permissible range T	Thermal mode acceptability criterion, optimisation "stop condition"	Defines limits for modes and design; when exceeded, changes in cooling/materials/current density are required

Note: EMF – electromagnetic force
Source: it is formed by the authors according to the method of parametric Binding of sub-models and the normative interpretation of permissible temperature limits by IEC 60034-18-1:2022 (2022) with calculated implementation in Ansys Motor-CAD and COMSOL Multiphysics 6.2

As shown in Table 3, temperature-parametric feedback changes electromagnetic results not through a single coefficient, but through a consistent set of corrections to the electrophysical and magnetic properties of materials. The most sensitive channel of influence is the temperature dependence of the electrical resistance of windings and conductors: as the temperature increases, R and resistivity increase, which directly increases the Joule losses I^2R and forms a positive thermal reverse circuit "heating → resistance → loss → additional heating". This means that without updating the temperature parameters, the electromagnetic calculation systematically underestimates the losses in copper and the associated temperature peaks. The second most important block of changes is related to magnetic characteristics. Temperature corrections of the magnetisation curves and effective magnetic permeability shift the operating point of the magnetic circuit and can lead to earlier saturation of individual sections. In the calculated terms, this manifests itself as a change in the distribution of induction and flow coupling, which affects the EMF and moment characteristics and indirectly – the current load of the windings. For machines with permanent magnets, a temperature decrease in the residual induction and coercive force is additionally triggered, which reduces the useful magnetic flux and requires current compensation, again increasing copper losses. Corrections for specific losses in steel and additional losses in structural elements have a more moderate but spatially important effect: they change the map of the distribution of heat sources in the magnetic circuit and adjacent metal parts. This does not always dramatically change the total losses, but it strongly affects the local heating zones that determine the critical temperature nodes of the model. Analysis of the influence of temperature corrections on electromagnetic results showed that the most significant changes are localised in areas where increased losses and limited heat dissipation are combined, primarily in the winding parts and adjacent areas of the magnetic circuit. In these domains, the refinement of parameters leads to a redistribution of specific losses and to changes in the integral indicators used in the design interpretation (in particular, total losses, efficiency, and temperature-limited load modes). Temperature-parametric feedback is not an auxiliary option, but a mandatory procedure for reproducible electromagnetic-thermal matching, since it determines whether the repeated electromagnetic calculation will correspond to the actual thermal conditions of the product and whether engineering conclusions regarding losses and modes will be correct within the accepted temperature limits.

The results of comparison of matching schemes in the electromagnetic-thermal formulation (n = 40 scenarios) showed that the convergence and stability of the calculation process are determined not only by the numerical method, but primarily by the structure of the sub-model binding and whether temperature feedback is implemented in the circuit "losses → heat sources → temperature field → temperature parameter corrections". With identical initial geometric and operating parameters, schemes without full two-way coupling demonstrate formal solution attainability only in terms of cooling conditions, whereas two-way approaches provide reproducible stabilisation of both temperature maxima and total losses when boundary conditions vary. Table 4 shows a comparison of four binding schemes by the proportion of convergent scenarios, the nature of convergence (monotonic/vibrational), the average number of iterations to stabilisation, sensitivity to changes in heat transfer coefficients, and contact thermal resistances, in addition to suitability for design optimisation problems.

Table 4. Comparative indicators of convergence and stability of electromagnetic-thermal matching schemes

Sub-model binding scheme	Communication structure	Convergent scenarios, n/40	The nature of convergence	Typical number of cycles/exchanges before stabilisation*	Sensitivity to cooling conditions (h, IC code)**	Sensitivity to contact thermal resistances	Consistency of the energy balance "losses ↔ heat"	Suitability for project optimisation	Computational cost
1) One-way transfer "loss → heat"	electromagnetic model→ thermal model (TH) (without *T*-feedback)	26/40	Formally stable, but without self-consistency of losses	1	High (risk of T_{max} bias with h variation)	Medium-high	Limited (unaccounted for *T*-effect on EM parameters)	High speed, but low physical correctness	Low
2) Sequential-iterative bilateral coordination	EM ⇄ TH (iterations with parameter updates)	36/40	Mostly monotonous	4-7 (median 5)	Low-medium (T_{max} and P_{loss} stabilisation in most modes)	Medium	High (convergence control by ΔT_{max} and ΔP_{loss})	High (best quality/time balance)	Medium
3) Co-simulation (variable modes / time exchange)	EM ⇄ TH (exchange per step/interval)	32/40	Possible fluctuations under "harsh" conditions	6-12 exchanges (median 8)	Medium-high (depends on the exchange settings)	High	Medium-high (sensitive to the exchange step)	High for variable modes, medium for mass runs	Medium-high
4) Integrated multi-physical calculation	joint solution EM+TH	38/40	Rack (least risk of swaying)	1 (conjugate solution)	Low	Medium	Very high	High as referent/ verification, medium for serial optimisation	High

Note: *"cycles/exchanges" refers to the steps taken to meet the convergence criteria for stabilising maximum temperatures and total losses (for example, conditionally: ΔT_{max} and ΔP_{loss} below specified thresholds); **"sensitivity to cooling conditions" is interpreted as the tendency of the circuit to change T_{max}/gradients and convergence when varying heat transfer coefficients and boundary conditions, parameterised through the IC code
Source: generated by the authors based on the results of parametric runs and post-processing in MATLAB/Simulink R2024a and Python 3.12 using calculation models in COMSOL Multiphysics 6.2 and ANSYS Fluent

Generalisation of indicators from Table 4 confirmed that the key factor of convergence and reproducibility of electromagnetic-thermal matching is the presence of temperature-parametric feedback and the way data exchange between sub-models is organised. The integrated multiphysical scheme showed the highest proportion of convergent scenarios – 38/40, while the lowest was the one-sided transfer of "loss → heat" – 26/40, which records a gap of 12 scenarios between the minimum and maximum convergence. In terms of the rate of stabilisation, the minimum value is 1 cycle/solution in schemes 1 and 4, but these are different in the meaning of "1": in Scheme 1, it is achieved without temperature feedback, while in scheme 4 – as a conjugate solution with full self-matching; the largest typical number of steps/exchanges is observed in the co – simulation-6-12 (median 8), which is the upper limit on labour intensity among the above schemes. In terms of cooling sensitivity, the extreme values are centred at the poles: the highest is in scheme 1, the lowest is in scheme 4, which is consistent with the fact that the conjugate solution itself minimises the "gap" between losses and the temperature field under variable boundary conditions. A systematic comparison of the results showed that the key indicator of the "engineering quality" of the scheme is not only the fact of achieving convergence, but also the consistency of the energy balance and the absence of a systematic shift in temperature maxima under small changes in boundary conditions. That is why, in design problems where serial parametric runs and design optimisation are required, it is advisable to adopt sequential-iterative two-way matching as the basic working procedure, using the integrated multiphysical scheme as a control (reference) to check the correctness of settings and for scenarios with the most severe thermal constraints.

DISCUSSION

A comparison of the established patterns of electromagnetic-thermal matching with current publications on multiphysics design and digital engineering has shown that the integration of CAD systems for electrical machines and devices with related electromagnetic and thermal models is developing as a common trend in the formalisation of exchange interfaces, convergence criteria and reproducible scenario settings in the CAD/CAE circuit. It is demonstrated that the reproducibility of integration of design modelling with multiphysical coordination was determined not by the presence of separate calculation domains, but by the formalisation of a bilateral computational circuit with fixed data transfer points and iteration completion criteria, which ensured the stabilisation of temperature maxima and total losses in a series of parametric runs. This statement was in accordance with the approach of P. Eitz *et al*. (2024), where multiphysical calculation was interpreted as a formalised workflow with controlled sub-model binding in a parametric modelling environment. A similar emphasis on the role of the binding structure and the correctness of state exchange between physical sub-models was reflected in the results of G. Mauromicale *et al*. (2023), which shows that multiphysical models lose their engineering suitability in the absence of consistent interfaces between Electrical and thermal quantities, which directly echoes the need to fix the points "losses → heat sources" and "temperature field → parameter updates". It was determined that the key condition for the correct binding of electromagnetic and thermal statements was domain-oriented spatial mapping of composite losses, in which Joule, magnetic, and local vortex losses were transmitted to the thermal model as distributed sources, and not as an aggregated total value; aggregation itself led to smoothing of the temperature field and loss of sensitivity to local overheating zones. This pattern was consistent with the conclusions drawn by C. Guo *et al*. (2022), where electromagnetic-thermal coupling for machines with permanent magnets and cooling channels was considered through the spatial correspondence of heat sources to structural domains, which determined local temperature peaks and their engineering interpretation. The consistency of the effect of the cooling configuration on the localisation of temperature maxima was reflected in the results of J. Chang & C. Wang (2022), which states that changing the organisation of the heat sink changes not so much the integral heating level, but the position and amplitude of critical zones, which coincided in interpretation with the established domain temperature stratification. It is shown that the normative-parametric unification of operating modes, cooling method, and temperature acceptability was functionally necessary for the reproducibility of comparing binding schemes since it provided the same "input base" for all scenarios and excluded situations where losses were calculated for conditions that were not equivalent to the limiting thermal conditions. The need to consider temperature rise as a target and control indicator for engineering solutions was consistent in the nature of the manifestation, with the results of H. Liu *et al*. (2024), where co-optimisation of electromagnetic and thermal solutions was aimed at minimising temperature gain, which was conceptually consistent with the use of temperature maximal stabilisation as a criterion for convergence and suitability of the solution.

It was established that temperature-parametric feedback determined the refinement of electromagnetic losses due to the temperature dependence of the resistance of conductors and changes in magnetic characteristics, forming a positive circuit "heating → resistance growth → loss growth → additional heating", and that is why circuits without full two-way binding showed lower reproducibility in terms of cooling conditions. This interpretation of the need for multipole binding was in line with the results of H. Cho *et al*. (2024), where it is shown that reliable mode estimation requires simultaneous consideration of the interaction of several physical subsystems, and a separate calculation distorts local constraints and mechanisms of critical zone formation. The parallel with the engineering need to maintain the manageability of complex design circuits through formalised procedures for processing and interpreting results echoed the generalisations of G. Li *et al*. (2024) on the role of intelligent methods in the design of complex electronic systems, which in this context corresponded to the use of standardised convergence and post-processing criteria for serial scenario runs. It was determined that comparing matching schemes was only technically informative if the same data transfer points and convergence criteria were maintained, as this ensured that the results were compared as an effect of the binding structure rather than as a consequence of incompatible exchange rules. This statement correlated with the conclusions of X. Wang *et al*. (2023) that in multiphysics design of complex systems, it is not the "presence of many physics" that is decisive, but the standardisation of interfaces and the coordination of data flows between domains, without which the comparability of scenarios is destroyed. The practical feasibility of using a specialised software environment for the design interpretation of thermal checks and losses in permanent magnet machines corresponded to the conclusions of F.A. Coteț *et al*. (2023) on the usefulness of using engineering design tools for electrical machines under the condition of correct binding and interpretation, which in this study was provided through a normative parametric framework and a two-way circuit with convergence confirmed on a set of 40 scenarios.

It is established that the domain temperature stratification in the coupled electromagnetic-thermal setting had a reproducible profile with maxima in the windings of about 130-140°C, in the magnetic circuit of 105-115°C, in the housing of 85-95°C, and in the cooling zone of 60-70°C, which fixed critical heating nodes precisely as a function of the spatial distribution of losses and heat dissipation paths. This logic of interpreting electrothermal constraints corresponded to an approach of A. Shandilya & V. Kumar (2024), where electrothermal analysis for traction drives was interpreted through local temperature peaks and their relationship to load and cooling modes. The analogy with multiscale coupling "2-D (dimensional) electromagnetic staging-3-D thermal staging" was traced in a paper of A. Ebrahimi Shohani *et al*. (2025), where dimensional separation was used to reproduce local thermal effects in complex geometry; in the above results, a similar need was manifested through the requirement of domain-oriented loss mapping, which preserved local temperature maxima rather than averaging them. Clarification of the role of the digital design circuit as a control system for multiphysical models echoed N.Y. Choi & S.U. Zhang (2025), where a combination of multiphysical simulation and project support algorithms was used to improve the reproducibility of high-level design solutions; in this case, formalised data exchange points and convergence criteria acted as such a "managed circuit". The correlation with the procedural formalisation of calculations through the experimental plan and the compared statements was traced in the study of N.Y. Choi *et al*. (2025), where benchmarking of thermal and electrical characteristics was based on comparable scenarios and controlled parameter variations; in the presented results, a similar function was performed by a unified input frame and comparability of 40 scenarios. It was recorded that the normative parametric unification of modes, cooling conditions, and temperature limits created a common parametric interface of sub-models and made the comparison of binding schemes correct, since all 40 scenarios had the same input base. This principle of "single input base → comparable scenarios → comparable binding structure effect" was in accordance with R. Cinar *et al*. (2025), where CAD-FEA automation was reduced to ensuring repeatability of statements and results when parameters vary. The generalisation of integrated multiphysical modelling in microsystems parallels the findings of A. Ghaemi *et al*. (2025), where the performance of the integrated model was determined by the consistency of domains and the correctness of energy transfer between them; in this case, domain-oriented loss mapping and convergence criteria performed a similar function.

An additional parallel regarding the controllability of multiphysical productions through standardised channel and profile configurations in microfluidic systems was observed in a study by P. Sai Kumar & S. Goel (2025), where the comparability of variants was provided by a structured variation of geometry and boundary conditions; unified modes, heat exchange conditions, and convergence control played a similar role in the presented results. Based on the comparison of coupling structures, it was established that "1 cycle" in a unilateral scheme and "1 conjugate solution" in an integrated multiphysical scheme have different engineering meanings: the former did not include temperature parameter updates, while the latter ensured self-consistency of losses and temperature field, which was reflected in the maximum convergence of 38/40. This difference in the interpretation of "speed" correlated with Z. Dong *et al*. (2025), where multiphysical models demonstrated that a formally shorter calculation can be methodically incomplete without correct domain binding. An analogy to the applied problems of electric and magnetic fields in high-voltage apparatuses was presented in a study by E. Tunç & M. Fidan (2025), where multiphysical modelling in the field calculation environment required a correct Binding of boundary conditions and material parameters; in the above results, a similar requirement was realised through the transfer of the temperature field to the update of electrophysical parameters. It is recorded that for design problems with serial parametric runs, the two-way iterative scheme turned out to be the most balanced in terms of "quality/time", since it provided a convergence of 36/40 for 4-7 cycles, while the integrated conjugate solution, although it gave 38/40, was characterised by a higher computational cost. This approach to the choice of the "working" and "reference" schemes was consistent with the work of S. Pavalkis & M. Otte (2025), where digital procedures were selected based on the scalability and cost of calculations while maintaining the quality of verification. A parallel with benchmark initiatives for traction electric motors was observed in L. Solimene *et al*. (2025), which emphasised the need for comparable data and uniform comparison procedures for multiphysical models; a unified input framework and formalised convergence criteria for a set of 40 scenarios played a similar role in the presented results.

Thus, the results of the study showed that the integration of CAD of electric machines and apparatuses with multiphysical modelling should be based on the interrelated formalisation of operating modes, cooling conditions and temperature acceptability, since it was their consistent task that determined the correctness of transferring electromagnetic losses to the thermal setting, localisation of critical heating zones and engineering interpretation of the results. Systematic comparison of the obtained regularities with the conclusions of modern research in the field of multiphysical design confirmed that the key role is played by standardised exchange interfaces between sub-models, domain-oriented mapping of heat sources, and the presence of temperature-parametric feedback as conditions for reproducible self-agreement of electromagnetic and thermal estimates in the design circuit.

CONCLUSIONS

Within the framework of the conducted research, a reproducible engineering procedure for electromagnetic-thermal matching in a multiphysical CAD circuit was formed on the basis of normative-parametric unification of the initial conditions, formalised two-way computational binding, and domain-oriented transfer of losses to the thermal setting. The constructed normatively consistent framework of modes, cooling IC code, insulation temperature limits, and energy efficiency classes provided a common parametric interface of sub-models and eliminated the discrepancy between the electromagnetic state description and thermal boundary conditions. Formalisation of a two-way computational circuit with fixed data transmission points and convergence criteria established a reproducible iterative matching scheme for the "losses → heat sources → temperature field → temperature parameter corrections" circuit, suitable for parametric scenarios and comparative runs. The structuring of electromagnetic losses, divided into Joule, magnetic, additional load, and local vortex components and their mandatory spatial mapping into thermal domains ensured the correctness of the energy balance and the preservation of local temperature maxima, while the aggregate transfer of total losses showed a loss of spatial sensitivity of the temperature field. Consistent temperature modelling recorded a stable heating domain stratification: for TMAX windings ≈130°C and critical values ≈140°C, for a magnetic circuit ≈105/115°C, for a housing ≈85/95°C, for a cooling zone ≈60/70°C, which confirmed the scenario-dependent localisation of critical zones, and the need for a connected, rather than isolated, thermal calculation. Temperature-parametric feedback showed a systemic effect on electromagnetic results through an increase in R(T) and P(T), a shift in the B-H characteristics, and a decrease in the parameters of permanent magnets, which forms an additional gain loop for copper losses and changes the distribution of heat sources in iterations. Comparison of matching schemes on a set of 40 scenarios established a convergence range from 26/40 for a one-way transfer of "loss → heat" to 38/40 for an integrated multiphysical solution; a series-iterative two-way scheme provided 36/40 matching scenarios with typical stabilisation in 4-7 cycles (median 5), while co-modelling required 6-12 exchanges (median 8) and showed higher sensitivity to heat exchange parameters and contact resistances.

Thus, the results proved that the effective integration of CAD of electrical machines and apparatuses with multiphysical modelling is implemented through a standardised two-way circuit of coordination of electromagnetic and thermal models with normatively unified inputs, formalised data exchange interfaces, and temperature parameter updating. The best balance of accuracy, stability, and computational cost for design tasks provides sequential-iterative two-way matching, while integrated multiphysical calculation can be used as a reference for verification and modes with rigid thermal constraints. Further research should be aimed at expanding multi-domain cooling models, automated optimisation of design parameters in a connected circuit, and experimental validation of temperature-loss maps for various types of electrical machines and apparatuses.

ACKNOWLEDGEMENTS

None.

FUNDING

None.

CONFLICT OF INTEREST

None.

REFERENCES

[1] Chang, J., & Wang, C. (2022). Electromagnetic thermal coupling analysis for a novel cooling system of an axial flux hub motor. *IET Electric Power Applications*, 16(4), 421-433. doi: 10.1049/elp2.12164.

[2] Cho, H., Park, J.S., Han, Y.S., Xu, G., & Sohn, D. (2024). Electromagnetic-thermal-mechanical coupling analysis of bent rotor straightening via electromagnetic induction heating. *Journal of Computational Design and Engineering*, 11(6), 283-299. doi: 10.1093/jcde/qwae104.

[3] Choi, N.Y., & Zhang, S.U. (2025). Digital design for high-performance IGBT devices using machine learning and multi-physics simulation. In *PCIM conference 2025; international exhibition and conference for power electronics, intelligent motion, renewable energy and energy management* (pp. 90-96). Berlin: VDE. doi: 10.30420/566541012.

[4] Choi, N.Y., Kim, D.H., Nam, S., Lee, Y.J., Kim, S.G., & Zhang, S.U. (2025). A benchmarking study on IGBT thermal-electrical performance using finite element analysis and design of experiments (DOE). *Journal of Electrical Engineering & Technology*, 20, 1113-1126. doi: 10.1007/s42835-025-02178-6.

[5] Cinar, R., Celik, H.K., Ucar, M., & Rennie, A.E. (2025). CAD-FEA integrated automation platform for structural design, deformation simulation, and size optimization of housings in external gear pumps. *Applied Sciences*, 15(23), article number 12564. doi: 10.3390/app152312564.
[6] Coteț, F.A., Văscan, I., & Szabó, L. (2023). On the usefulness of employing ANSYS Motor-CAD software in designing permanent magnet synchronous machines. *Designs*, 7(1), article number 7. doi: 10.3390/designs7010007.
[7] Dong, Z., Wei, W., Song, B., Chen, X., & Zong, Z. (2025). A coupled electromagnetic, heat transfer, phase transition and thermodynamic model for concrete breaking under microwave heating: Multiphysics simulation and experimental investigations. *Thermal Science and Engineering Progress*, 68, article number 104276. doi: 10.1016/j.tsep.2025.104276.
[8] Ebrahimi Shohani, A., Farahzadi, M., Ali, S., Abbaszadeh, K., Marignetti, F., & Farrokh, F. (2025). 2-D electromagnetic analysis coupled with 3-D thermal analysis of a dual-PM excited flux-switching generator with overhang structure for direct drive wind turbines. *IET Electric Power Applications*, 19(1), article number e70042. doi: 10.1049/elp2.70042.
[9] Eitz, P., Zinke, T., & Lieberwirth, H. (2024). Multiphysics simulation of a vertical roller mill in Matlab®/Simulink®. *BHM Berg-und Hüttenmännische Monatshefte*, 169(8), 421-430. doi: 10.1007/s00501-024-01496-y.
[10] Ghaemi, A., Ebrahimi, A., & Hajipour, M. (2025). Integrated multiphysics modeling of a piezoelectric micropump. *ArXiv*. doi: 10.48550/arXiv.2502.06413.
[11] Guo, C., Long, L., Wu, Y., Xu, K., & Ye, H. (2022). Electromagnetic-thermal coupling analysis of a permanent-magnet in-wheel motor with cooling channels in the deepened stator slots. *Case Studies in Thermal Engineering*, 35, article number 102158. doi: 10.1016/j.csite.2022.102158.
[12] IEC 60034-1:2022. (2022). *Rotating electrical machines – Part 1: Rating and performance*. Retrieved from https://webstore.iec.ch/en/publication/65446.
[13] IEC 60034-18-1:2022. (2022). *Rotating electrical machines – Part 18-1: Functional evaluation of insulation systems*. Retrieved from https://webstore.iec.ch/en/publication/64618.
[14] IEC 60034-2-1:2024. (2024). *Rotating electrical machines – Part 2-1: Standard methods for determining losses and efficiency from tests*. Retrieved from https://webstore.iec.ch/en/publication/67756.
[15] IEC 60034-30-1:2025. (2025). *Rotating electrical machines – Part 30-1: Efficiency classes of line operated AC motors*. Retrieved from https://webstore.iec.ch/en/publication/91195.
[16] IEC 60034-6:1991. (1991). *Rotating electrical machines – Part 6: Methods of cooling*. Retrieved from https://webstore.iec.ch/en/publication/143.
[17] Kostin, O., Yaros, O., Yaros, Y., Savenko, A., Martynenko, V., & Boyko, I. (2022). Method for evaluating the stability of arc burning of electrodes with rutile-cellulosic covering. In *Proceedings of the 4th international conference on modern electrical and energy system*. Kremenchuk: IEEE. doi: 10.1109/MEES58014.2022.10005682.
[18] Li, G., Shan, G., Zheng, Y., Meng, B., & Cao, H. (2024). The application of machine learning methods in the design of electronic systems for robotics. *Journal of Artificial Intelligence*, 1(2), article number 1015.
[19] Liu, H., Luta, J.A., Pekarek, S.D., & Weibel, J.A. (2024). Electromagnetic-thermal co-optimization to minimize case-to-winding temperature rise in permanent magnet machines. *Applied Thermal Engineering*, 238, article number 122132. doi: 10.1016/j.applthermaleng.2023.122132.
[20] Manka, M., Karpiel, G., & Prusak, D. (2023). Computer-aided design of electric drives with FEA software. In K. Soliman (Ed.), *Artificial intelligence and machine learning* (pp. 250-263). Cham: Springer. doi: 10.1007/978-3-031-62843-6_25.
[21] Mauromicale, G., Calabretta, M., Scarcella, G., Scelba, G., & Sitta, A. (2023). Multi-physics models of a low-voltage power semiconductor system-in-package for automotive applications. *Journal of Electronic Packaging*, 145(3), article number 031003. doi: 10.1115/1.4056413.
[22] Młot, A., Korkosz, M., Lechowicz, A., Podhajecki, J., & Rawicki, S. (2022). Electromagnetic analysis, efficiency map and thermal analysis of an 80-kW IPM motor with distributed and concentrated winding for electric vehicle applications. *Archives of Electrical Engineering*, 71(4), 981-1002. doi: 10.24425/aee.2022.142120.
[23] Pavalkis, S., & Otte, M. (2025). Accelerating digital engineering adoption: A comprehensive example using MBSE and digital twin with a portable robotic arm. *INSIGHT*, 28(5), 67-71. doi: 10.1002/inst.70007.
[24] Pliuhin, V., Sukhonos, M., Biletskyi, I., Plankovskyy, S., & Tsegelnyk, Y. (2024). Implementation features of local and remote technical objects digital twins. *IOP Conference Series: Earth and Environmental Science*, 1376, article number 012036. doi: 10.1088/1755-1315/1376/1/012036.
[25] Pliuhin, V., Tsegelnyk, Y., Sukhonos, M., Biletskyi, I., Plankovskyy, S., & Tietieriev, V. (2025). Machine learning and HPC in computer-aided design of electric machines. In B.B. Youssef & M. Ismail (Eds.), *Integrating machine learning into HPC-based simulations and analytics* (pp. 145-196). London: IGI Global. doi: 10.4018/978-1-6684-3795-7.ch007.
[26] Reato, F.M., Ricci, C., Misfatto, J., Calzaferri, M., & Cinquemani, S. (2023). An alternative multi-physics-based methodology for strongly coupled electro-magneto-mechanical problems. *Algorithms*, 16(6), article number 306. doi: 10.3390/a16060306.

[27] Sadovoy, O., Vakhonina, L., Koshkin, D., & Martynenko, V. (2022). Comparison of active power losses of single-phase electromagnetic static devices by radial electromagnetic system. In *Proceedings of the 4th international conference on modern electrical and energy* system (pp. 1-5). Kremenchuk: IEEE. doi: 10.1109/MEES58014.2022.10005760.

[28] Sai Kumar, P., & Goel, S. (2025). Multiphysics simulations on the effect of fluidic concentration profiles over Y-channel and T-channel designs. In S. Goel (Ed.), *Micro electromechanical systems practical lab manual* (pp. 1-11). London: Wiley. doi: 10.1002/9781394229864.ch1.

[29] Santos, J.F.D., Tshoombe, B.K., Santos, L.H., Araújo, R.C., Manito, A.R., Fonseca, W.S., & Silva, M.O. (2022). Digital twin-based monitoring system of induction motors using IoT sensors and thermo-magnetic finite element analysis. *IEEE Access*, 11, 1682-1693. doi: 10.1109/ACCESS.2022.3232063.

[30] Shandilya, A., & Kumar, V. (2024). Electro-thermal analysis of permanent magnet synchronous motor for electric vehicles. *SAE Technical Paper*, 2024-28-0080. doi: 10.4271/2024-28-0080.

[31] Solimene, L., *et al*. (2025). The galileo ferraris contest: A benchmark initiative for data-driven multi-physics modeling of traction electric motors. *TechRxiv*. doi: 10.36227/techrxiv.176583445.54143509/v1.

[32] Tunç, E., & Fidan, M. (2025). Electric and magnetic field analysis for a 34.5 kV transformer under composite voltage conditions: COMSOL multiphysics simulation. *Duzce University Journal of Science and Technology*, 13(3), 1161-1179. doi: 10.29130/dubited.1624167.

[33] Umland, N., Winkler, K., & Inkermann, D. (2023). Multidisciplinary design automation of electric motors – systematic literature review and methodological framework. *Energies*, 16(20), article number 7070. doi: 10.3390/en16207070.

[34] Usca-Gomez, H.G., Puma-Benavides, D.S., Zambrano-Leon, V.D., Castillo-Díaz, R., Quinga-Morales, M.I., Solís-Santamaria, J.M., & Llanes-Cedeño, E.A. (2025). A review and case of study of cooling methods: Integrating modeling, simulation, and thermal analysis for a model based on a commercial electric permanent magnet synchronous motor. *World Electric Vehicle Journal*, 16(8), article number 437. doi: 10.3390/wevj16080437.

[35] Wang, X., Chen, D., Li, D., Kou, C., & Yang, Y. (2023). The development and progress of multi-physics simulation design for TSV-based 3D integrated system. *Symmetry*, 15(2), article number 418. doi: 10.3390/sym15020418.

Лариса Вахоніна
Кандидат фізико-математичних наук, доцент
Миколаївський національний аграрний університет
54008, вул. Георгія Гонгадзе, 9, м. Миколаїв, Україна
https://orcid.org/0000-0002-1668-2275

Володимир Мартиненко
Кандидат технічних наук, доцент
Миколаївський національний аграрний університет
54008, вул. Георгія Гонгадзе, 9, м. Миколаїв, Україна
https://orcid.org/0000-0003-4067-3640

Андрій Руденко
Аспірант, асистент
Миколаївський національний аграрний університет
54008, вул. Георгія Гонгадзе, 9, м. Миколаїв, Україна
https://orcid.org/0000-0002-5103-6412

Віталій Мардзявко
Аспірант, асистент
Миколаївський національний аграрний університет
54008, вул. Георгія Гонгадзе, 9, м. Миколаїв, Україна
https://orcid.org/0000-0001-7327-9215

Інтеграція САПР електричних машин і апаратів із мультифізичним моделюванням: підхід до узгодження електромагнітних і теплових моделей

Анотація. Ізольоване використання електромагнітних або теплових розрахунків під час проєктування електричних машин і апаратів є суттєвим джерелом інженерних похибок, оскільки робочі режими формуються взаємопов'язаними польовими й тепловими процесами. Метою дослідження було обґрунтувати та формалізувати підхід до інтеграції автоматизованого проєктування з мультифізичним моделюванням через узгодження електромагнітної та теплової моделей у єдиному параметрично керованому контурі. Методологія ґрунтувалася на нормативно узгоджених режимах, умовах охолодження та температурних межах із двостороннім ітераційним зв'язуванням і просторово узгодженим перенесенням втрат у теплову модель з температурною корекцією властивостей матеріалів. У результаті сформовано спільну параметричну рамку входів, що забезпечує узгоджене трактування навантаження, охолодження, температурної прийнятності та енергетичної результативності. Формалізований двосторонній контур із критеріями збіжності забезпечив відтворювану стабілізацію температурних максимумів і сумарних втрат. Показано, що просторове картування складових втрат зберігає локальні зони перегріву, тоді як їх зведене перенесення згладжує температурне поле. Узгоджене моделювання встановило доменну стратифікацію нагріву: в обмотках близько 130-140 °C, у магнітопроводі 105-115 °C, у корпусі 85-95 °C, у зоні охолодження 60-70 °C. Температурні корекції електричних і магнітних параметрів суттєво змінюють розподіл втрат, насамперед через зростання опору провідників. Порівняння чотирьох схем узгодження на 40 сценаріях показало збіжність від 26 з 40 для одностороннього зв'язування до 38 з 40 для інтегрованого розв'язання; двостороння ітераційна схема забезпечила 36 з 40 зі стабілізацією за 4-7 циклів, тоді як покрокове спільне моделювання потребувало 6-12 обмінів. Практична значимість полягає у можливості безпосереднього використання підходу для підвищення точності теплових перевірок, вибору режимів навантаження та оптимізації конструктивних рішень електротехнічних виробів

Ключові слова: температурне поле; двосторонній контур; об'ємне джерело; ко-симуляція; теплові джерела; вихрові втрати

Machinery & Energetics
Vol. 17, No. 1. 2026

Journal homepage:
https://technicalscience.com.ua/en

UDC 621.431.73
DOI: 10.31548/machinery/1.2026.43

ISSN 2663-1334
e-ISSN 2663-1342

Viktor Duhanets*
Doctor of Pedagogical Sciences, Professor
Higher Educational Institution "Podillia State University"
32316, 12 Shevchenko Str., Kamianets-Podilskyi, Ukraine
https://orcid.org/0000-0002-3383-5907

Vitaliy Pukas
PhD in Technical Sciences, Associate Professor
Higher Educational Institution "Podillia State University"
32316, 12 Shevchenko Str., Kamianets-Podilskyi, Ukraine
https://orcid.org/0000-0002-0083-7359

Mykola Volynkin
Master of Science, Assistant
Higher Educational Institution "Podillia State University"
32316, 12 Shevchenko Str., Kamianets-Podilskyi, Ukraine
https://orcid.org/0009-0006-4960-8537

Increasing thermal efficiency in internal combustion engines through automated control of operational processes

Abstract. The study aimed to analyse a closed-loop control strategy that adjusts the ignition timing and fuel injection to increase work output in the cylinder whilst ensuring knock safety and reducing cycle instability. The methodology was based on methods of energy (thermal) balance analysis, classification and analytical systematisation, structural-functional modelling, comparative analysis and analytical generalisation. It has been established that the thermal efficiency of an internal combustion engine (ICE) is the proportion of the fuel energy converted into useful work. The difference between theoretical and actual efficiency indicated the amount of energy lost due to mechanical and auxiliary processes. The energy balance reflected the distribution of fuel energy between useful work at the shaft, heat dissipation to the cooling system, losses with exhaust gases, and other types of losses, allowing the dominant directions of its utilisation to be identified. Increasing the efficiency is limited by rising pressures, temperatures and thermal loads; therefore, optimal heat release phasing is key, which must be maintained without detonation or excessive peaks. The study determined that injection and ignition parameters determine the combustion phasing and power output; and since injection alters ignition conditions, the ignition timing must be coordinated with the fuel strategy (particularly in a closed-loop system). Parameter optimisation was constrained by detonation, thermomechanical, emission and operational factors, which define the permissible range of settings. The study noted that automated control improves efficiency by optimising mixture formation and the combustion phase, and by reducing mechanical and auxiliary losses through coordinated control of the subsystems. The reduction in mechanical and auxiliary losses was achieved through a combination of tribological solutions and control of the units to avoid excessive energy consumption. The use of energy balance as a criterion and coordinated closed-loop control of ignition, fuel supply and auxiliary systems via the engine control unit (ECU) makes it possible to reduce dominant losses and improve the efficiency of the internal combustion engine within the limits of detonation and thermal load constraints. The practical significance lies in the ability of engineers to apply the results when calibrating the ECU during bench tests and engine tuning on the vehicle

Keywords: detonation; ignition; injection; restriction; combustion phasing

Article's History: Received: 07.11.2025; Revised: 02.02.2026; Accepted: 26.02.2026; Published: 30.03.2026.

Suggested Citation:
Duhanets, V., Pukas, V., & Volynkin, M. (2026). Increasing thermal efficiency in internal combustion engines through automated control of operational processes. *Machinery & Energetics,* 17(1), 43-54. doi: 10.31548/machinery/1.2026.43.

*Corresponding author

INTRODUCTION

In the context of the global energy transition, internal combustion engines (ICEs) remain critical for heavy-duty transport and off-grid power generation, which necessitates further improvements in their operational and environmental performance. Improving thermal efficiency is a priority, as even a small reduction in specific fuel consumption translates into a significant reduction in costs and harmful emissions across the industry. At the same time, the potential for purely design-based improvements in many production solutions is limited by knock resistance, thermal loads and service life requirements, particularly under variable operating conditions. Under such conditions, automated control of operational processes becomes one of the most effective tools for further optimisation: intelligent control systems can maintain real-time convergence towards optimal combustion phasing, whilst simultaneously mitigating detonation risks and adapting the cycle to operation on alternative fuels, which poses a challenge for static maps and algorithms.

Scientific literature confirms that control strategies which simultaneously account for combustion phasing, detonation constraints and cycle variability are effective. The study by Q. Zhu *et al.* (2021) demonstrated the possibility of online optimisation of the ignition timing based on models of combustion phasing, detonation and the IMEP coefficient of variation. This means that the ignition optimum is formulated as a multi-criteria problem, where "efficiency" is not separated from stability and detonation limits, which is of fundamental priority for real-world control. In parallel with ignition optimisation, approaches are being developed to reduce detonation sensitivity through fuel strategy and combined ignition modes. D. Lou *et al.* (2024) demonstrated that hydrogen injection methods and spark ignition strategies alter the conditions for detonation in a hydrogen engine. In automated control, ignition should not be considered in isolation, but as an element of coordinated control of mixture formation and energy supply mode.

Y. Kou *et al.* (2022) found that the Taguchi-Grey combination (a combination of two methods for multi-criteria optimisation of process/system parameters) can be used for systematic selection of parameters that reduce the susceptibility to detonation in spark-ignition internal combustion engines. This approach confirms that even with complex process non-linearity, stable "optimal" settings can be found, but for practical application, these findings must be adapted to changing conditions in real time. V. Mittal (2024) summarised advances in detonation detection in spark-ignition engines and emphasised that improving the accuracy and speed of algorithms is critical for more aggressive ignition control strategies. In practice, this makes it possible to operate closer to the detonation limit without compromising reliability, which translates into improved thermal efficiency.

Efficiency optimisation can be achieved not only through the ignition timing but also through speed profile control. J. Song & H.H. Song (2022) noted that optimising the engine's speed profile improves net indicated efficiency and provided a quantitative explanation of the mechanisms underlying this optimisation. This indicates that automation must cover a broader set of controlled variables, rather than being limited to a single parameter. The expansion of the fuel base places greater demands on the control of operational processes. R. Menaca *et al.* (2025), using the example of an optical engine with multi-spark ignition, confirmed that multi-point/multi-cycle spark generation can sustain combustion with more complex fuels, and numerical validation enhances confidence in control models. Automated algorithms must be compatible with non-conventional ignition modes and exhibit greater sensitivity to ignition conditions. In a study by J. Park *et al.* (2023), a one-dimensional convolutional neural network with hyperparameter optimisation and data augmentation was used to determine the onset of detonation. This approach demonstrates the suitability of such models for integration into on-board systems as a "sensory layer" for adaptive control.

Ukrainian studies also confirm the practical benefits of precise ignition control for alternative fuels and specific power units. N.Ye. Ryaboshapka *et al.* (2023) found that changing the ignition advance angle affects the operating processes of a petrol internal combustion engine when running on fuel containing ethanol. This confirms the need for adaptive (automated) ignition adjustment for fuel mixtures, where the optimum depends on the operating mode and fuel composition. H.I. Slynko *et al.* (2022) found that installing an ignition timing variator in combination with a gas cylinder system (propane-butane) improves the performance of a specific engine. This provides practical justification for the effectiveness of ignition correction measures as an element of automated control, capable of maintaining higher thermal efficiency without altering the design.

Despite the development of individual solutions for optimising ignition and detecting knock, there is a lack of a coordinated, automated control loop within the engine control unit (ECU) that coordinates ignition and fuel injection within the constraints (knock, instability, fuel variability) and demonstrates an increase in thermal efficiency through the energy balance. Therefore, the study aimed to evaluate a closed-loop adaptation of ignition and fuel delivery aimed at improving performance indicators regarding knock and cycle variability. To achieve this objective, the following tasks were set: to identify the dominant channels of energy loss in the internal combustion engine based on the energy (thermal) balance; to justify a closed-loop ECU system for coordinated control of fuel delivery and ignition, incorporating safety constraints; to interpret the effect of automation through changes in the proportions of thermal, pumping, mechanical and auxiliary losses in the engine's overall energy balance.

MATERIALS AND METHODS

The study was of an analytical and synthetic nature and aimed to provide a theoretical justification for coordinated closed-loop control of fuel injection and ignition to improve the specific efficiency of internal combustion engines within the constraints of detonation, thermomechanical and emission limits. The conceptual framework was developed through the synthesis of energy balancing approaches, control theory and experimental data from scientific publications in the field of internal combustion engine process automation. The information base for the research consisted of scientific publications in peer-reviewed journals from 2020 to 2025, sourced from the Scopus, Web of Science and Google Scholar databases, on improving internal combustion engine efficiency and engine control, as well as works on the adaptation of control systems to alternative fuels.

The study combined methods of energy (thermal) balance analysis, classification and analytical systematisation, structural and functional modelling, comparative analysis and analytical generalisation to identify loss pathways based on the energy balance and to optimise the control actions of the electronic control unit to improve the thermal efficiency of the internal combustion engine. Using the method of energy (thermal) balance analysis, the fuel energy was decomposed into work output at the shaft and losses, which were classified into three groups: thermal, gas-dynamic (pumping), mechanical and auxiliary, based on the nature of the losses, their sources and the expected direction of reduction, as these loss groups reflect the main physically distinct energy dissipation channels in the internal combustion engine and correspond to the basic items of the energy balance, which are subject to separate control and optimisation. This approach has made it possible to structure the control object according to loss channels and establish a basis for evaluating the control effect by changing the proportions of losses in the balance whilst adhering to constraints (detonation, peak pressures/temperatures, thermal load, emissions, actuator limits).

Using a classification-based analytical systematisation of constraints, a list of key optimisation limits for ICE operating processes has been compiled, categorised as follows: thermomechanical, detonation/combustion stability, emissions, actuator and measurement, and operational variability. These constraints were selected as fundamental because they directly determine the permissible range of operating modes and settings and are decisive for ensuring performance, reliability, environmental compliance and the feasibility of control under real operating conditions. The criterion for the effectiveness of adjusting the control parameters (combustion phasing, ignition advance angle and injection characteristics) was an analytical interpretation of the increase in the proportion of fuel energy converted into energy, achieved by reducing the proportion of thermal, gas-dynamic and mechanical losses within the established limits. This approach was used to interpret the effect of automation as a conceptual redistribution of fuel energy between loss channels within the permissible range of settings, defined by thermomechanical and detonation constraints (a quantitative assessment of loss reduction was not performed within the scope of this theoretical study). Using the method of structural-functional modelling, the architecture of the ECU was generalised as a closed-loop system "sensors → algorithms (state estimation, controllers/maps, diagnostics and protection) → actuators", with three functional levels identified (measurement, computation, execution). This formalisation made it possible to link controllable variables (fuel injection, ignition, gas exchange, component control) to the corresponding measurements, algorithms and constraints (knock, temperature limits, emissions, reliability) and to demonstrate the role of models and observers in ensuring robustness. This was done to justify the ECU as the central mechanism for implementing coordinated control to maintain the optimal combustion phase and reduce losses without exceeding the specified limits.

Using comparative analysis and the systematisation of scientific sources, the theoretical approaches to reducing heat loss have been categorised as follows: balanced (Popa *et al.*, 2022), combustion phase control (Ahmed *et al.*, 2022), early combustion suppression (Watanabe *et al.*, 2021), and process stabilisation (Björnsson & Tunestal, 2024). These approaches were selected as they correspond to the main physical "levers" governing heat loss formation in the cylinder – the phase and duration of heat release, the level of peak temperatures/pressures, and the proportion of unstable cycles – whilst also having direct, implementable control effects in the ECU. The comparison criteria were physical mechanism for reducing heat transfer (energy redistribution, changes in combustion phase/duration, peak limitation, reduction of cycle variation) and type of automated control involvement (balance-based evaluation, target phase maintenance, operation within limits, closed-loop corrections). This formulated a coordinated scheme of control actions specifically aimed at reducing heat losses in the CPG and assessed the feasibility of combining approaches within the constraints of thermomechanical and detonation limits. Analytical generalisation was used to systematise methods for increasing the overall thermal efficiency of internal combustion engines via two pathways: combustion optimisation (indicator level) and the reduction of mechanical and auxiliary losses (output shaft level), which differentiates between the contribution of processes within the cylinder and losses due to friction/drive of components, as well as the comparison of controllable parameters (injection, ignition, pump/lubrication control) within the constraints of reliability and operational safety. This approach formed the methodological basis for selecting a coordinated control strategy via the ECU and interpreting its impact on the components of energy losses.

RESULTS AND DISCUSSION

Automated workflow management to improve the efficiency of internal combustion engines

The thermal efficiency of an internal combustion engine is the proportion of the fuel's chemical energy that is converted into useful mechanical output at the crankshaft in a real-world cycle. It is assessed by the indicated and effective (braking) thermal efficiency: the indicated efficiency reflects the conversion of energy in the cylinder into gases, whilst the effective efficiency accounts for additional losses between the cylinder and the shaft (friction, drive of units, auxiliary systems); the difference between them characterises the total mechanical and auxiliary losses. A significant proportion of heat is also lost through heat exchange with the cylinder walls and the cooling system, and via the exhaust gases (Popa *et al.*, 2022). It is advisable to describe these components using the engine's energy balance, which can identify dominant loss pathways in a specific operating mode and priority control measures (Table 1).

Table 1. Classification of energy losses in internal combustion engines

Type	Characteristic	Main sources of formation	Loss reduction method
Heat-based	Heat dissipation into structural components and via the exhaust gases, and losses due to incomplete combustion	Heat exchange in the combustion chamber, elevated exhaust gas temperature, and incomplete air-fuel mixing and ignition	Optimisation of combustion phasing and heat release profile, evaluation based on the heat balance
Gas-dynamic (pump-driven)	Increase in negative gas exchange at the inlet/outlet	Restrictions in the intake/exhaust tract, throttling at partial loads, the effects of supercharging and recirculation	Control of gas exchange processes (blowing, recirculation, gas distribution phases)
Mechanical and auxiliary	Losses of mechanical energy due to friction and the drive of auxiliary units	Friction in cylinder-piston group, crankshaft-connecting rod mechanism and bearings; energy consumption of pumps, generator, and cooling and lubrication systems	Tribological/design solutions, optimal control of units with a focus on reliability

Source: compiled by the authors based on National Academies of Sciences, Engineering, and Medicine (2021), A. Gangopadhyay (2021), Z. Liu *et al*. (2022), D. Popa *et al*. (2022)

Heat losses depend on heat transfer, exhaust energy and incomplete combustion; they are therefore reduced primarily by controlling the timing and progression of combustion and are assessed via the heat balance. Pump losses are determined by gas exchange and increase at partial loads due to resistance in the ducts and throttling; their margin is linked to gas exchange control and the coordination of these effects with the load regime. Mechanical and auxiliary losses are caused by friction and the drive of the units; therefore, they are reduced by a combination of tribological solutions and optimal control of the subsystems without compromising reliability. Improving thermal efficiency is a complex process, and the benefits of automation should be justified by analysing the changes in the proportions of losses within the engine's overall energy balance.

To identify the predominant losses under different operating conditions, an energy (thermal) balance is used, within which the fuel energy is distributed between output at the shaft, heat in the cooling system, exhaust energy, and mechanical and other losses. Balance analysis provides a basis for setting priorities: if thermal losses predominate, the focus is on controlling the combustion process and heat transfer; if mechanical and auxiliary losses predominate, the focus is on reducing friction and optimising the control of systems (pumps, cooling, lubrication) (Popa *et al.*, 2022). At the same time, the potential for improving efficiency is limited by physical and design factors: an increase in efficiency is accompanied by higher peak pressures and temperatures, increased heat fluxes to components, a more acute trade-off between efficiency and emissions (particularly nitrogen oxides), as well as higher demands on the strength and thermal stability of components. This determines the practical limits of further loss reduction and the need to optimise operating processes whilst considering reliability and environmental standards (Watanabe *et al.*, 2021).

Thermodynamic efficiency in a real internal combustion engine cycle is primarily determined by when and how intensely the heat of combustion is released in relation to piston movement and changes in volume. Under identical conditions, different phasing and shapes of the heat release curve result in different amounts of output and heat losses; therefore, the key controllable factors are injection (timing, duration, pressure, pulse structure) and ignition (advance angle, spark energy, knock control). Maximum output is achieved when the main heat release occurs near top dead centre (the position of the piston in the cylinder when it is at its highest point (at the end of the compression or exhaust stroke) and before the change in direction of movement), but without excessive peak pressures/temperatures and without detonation. Late combustion increases exhaust losses, whilst excessively early combustion increases mechanical loads, heat fluxes to the cylinder walls and the risk of detonation; therefore, the optimum is a compromise that the control system must maintain across a wide range of operating conditions. This is confirmed by approaches to optimising the ignition timing with constraints (Arsie *et al.*, 2024) and closed-loop control of the combustion phase to improve stability/efficiency under inter-cylinder variations (Björnsson & Tunestal, 2024).

In petrol direct-injection internal combustion engines, the injection timing determines the mixture structure (homogeneous/layered), local air-fuel ratios and flame development conditions. At high loads, evaporation and mixing affect the combustion rate and duration, cyclic fluctuations and susceptibility to knock. Changes in the injection timing and pressure alter the combustion process, efficiency and emission characteristics, through a shift in the heat release phase, changes in heat losses (including to the cylinder walls) and the "efficiency-toxicity" trade-off (Wang *et al.*, 2023). For diesel modes, the start/end of injection and the division into multiple pulses are critical, as they influence ignition delay, pressure rise rate, combustion behaviour, peak temperatures and, consequently, indicated efficiency, nitrogen oxide emission limits and reliability. A promising approach is adaptive dynamic control of injection timing using deep reinforcement learning methods, which accounts for non-linearity and changing conditions and reduces the need for manual re-tuning at each operating point (Henry de Frahan *et al.*, 2022).

Ignition and injection are interrelated: the ignition timing determines the combustion phase, but the injection timing alters the ignition conditions and the rate of flame propagation, and consequently the optimum ignition angle. Therefore, modern 21st-century strategies coordinate these parameters via combustion phase targets; one example is model-predictive control, which coordinates injection and ignition influences whilst accounting for actuator limitations, stability and emissions (Ahmed *et al.*, 2022). Injection and ignition determine efficiency through mixture formation and the combustion phase/rate (and duration), which affects net output, exhaust losses and heat transfer to the cylinder walls; optimisation is implemented as automated control of the combustion phase, taking into account detonation, thermal load, emissions and actuator limits, as confirmed experimentally. However, the optimisation of combustion phasing, injection and ignition is not arbitrary: it is constrained by thermomechanical, knock, emission, actuator-measurement and operational factors. These limitations define the permissible range of settings and determine which parameters can be adjusted in a given mode (Table 2).

Table 2. Key constraints on the optimisation of ICE operating processes

Restriction class	Characteristic	Impact on selection of optimisation parameters
Thermomechanical	Peak pressure/rate of pressure rise, temperature limits and heat fluxes	They limit the "early" combustion phase, as the load and heat transfer increase
Detonation and combustion stability	For spark-ignition engines – knocking; at partial loads – stability limits	Ignition timing and lean-burn modes are restricted due to the risk of unstable combustion
Environmental (emissions)	Trade-offs between efficiency and emissions (nitrogen oxides/particulate matter)	Require a multi-criteria selection of settings
Actuators and sensors	Injector/ignition timing, sensor delays and errors, air-fuel ratio limits	Limit the range of available modes and make precise control more difficult
Operational flexibility	Non-linearity, changing conditions, differences between cylinders, ageing	Necessitates adaptability and robustness in control systems

Source: compiled by the authors based on K. Watanabe *et al.* (2021), O.Y. Ahmed *et al.* (2022), M. Henry de Frahan *et al.* (2022), I. Arsie *et al.* (2024), O. Björnsson & P. Tunestal (2024), J. Wang *et al.* (2023)

Optimising fuel injection, ignition and combustion phasing to improve thermal efficiency involves finding the optimum within the range of permissible operating conditions, rather than an "absolute" maximum. The decisive constraints are thermomechanical limits (peak pressure, rate of pressure rise, temperatures and heat fluxes), knock resistance and combustion stability for spark-ignition engines, as well as environmental trade-offs between efficiency and emissions (particularly nitrogen oxides and soot), as confirmed by experiments varying injection parameters. Furthermore, the feasibility of optimal settings is limited by the capabilities of actuators and measurement accuracy; therefore, practical efficiency improvements are achieved through control methods that explicitly account for these limitations and closed-loop combustion phase control, and in conditions of operating mode variability – through adaptive approaches subject to safety controls.

The modern 21st century internal combustion engine is a dynamic system in which efficiency, emissions and reliability depend to a large extent on the precision of real-time control of operational processes. The central element is the ECU, which, based on measurements, state assessments and safety limits, controls fuel supply, ignition, gas exchange and auxiliary systems in steady-state and transient modes and under changing operating conditions. A typical ECU architecture implements a closed-loop system with three functional levels: measurement (sensors), computation and algorithms (filtering, state estimation, maps/controllers, diagnostics and protection), and actuators (injectors, ignition, air control devices, and, where necessary, gas distribution and assemblies). In the context of improving thermal efficiency, the ECU provides control of the air-fuel mixture composition and fuel delivery, optimisation of ignition considering knock and temperature limits, maintaining the target combustion phase (maps + feedback), as well as reducing auxiliary costs through subsystem control without compromising reliability (Aliramezani *et al.*, 2021). As engine complexity increases, so does the role of models and data processing methods (tuning, state observers, adaptive control elements); however, their application requires robustness and safety guarantees (Fig. 1).

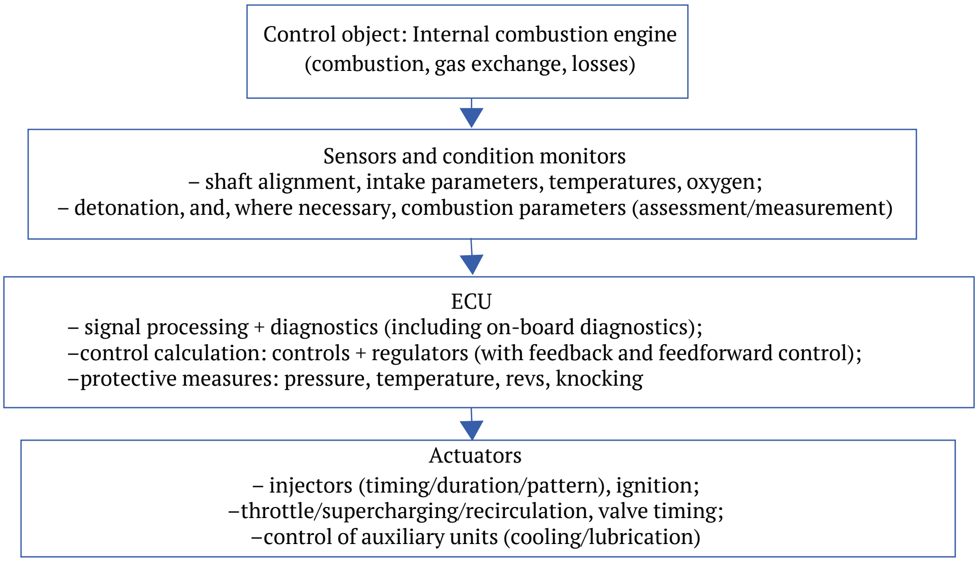

Figure 1. Generalised structure of ECU
Source: compiled by the authors based on M. Aliramezani *et al.* (2021), B.C. Pereira *et al.* (2023)

The ECU implements a closed-loop system of “sensors → algorithms (state/limit estimation) → actuators”, aligning combustion parameters with efficiency, emissions and reliability requirements, and ensuring coordinated control of fuel delivery, ignition, gas exchange and auxiliary systems. As engine complexity increases, so does the role of models and data processing methods; however, their application requires resilience to disturbances and uncertainties, as well as safety guarantees.

The results of the study showed that the energy (thermal) balance serves as a practical tool for identifying the dominant loss pathways in a specific operating mode and selecting priority control actions. Injection parameters act as a key lever which, by altering the heat release rate and combustion phase, redistributes energy between output and losses. A similar interpretation of the balance approach is demonstrated by M. Güler & M. Özkan (2022), who found that the energy balance is not merely a descriptive framework but a practical optimisation tool: for a direct-injection diesel engine with multi-pulse injection, the authors performed a breakdown of fuel energy across loss channels and demonstrated that the selection of timing/number of pilot pulses alters the distribution between output and losses (exhaust/cooling/other components). Therefore, the balance analysis provides a quantitative basis for optimising injection parameters: it can be used not only to improve thermal efficiency but also to identify which specific loss channel (exhaust, cooling or other components) is responsible for the gains achieved in a particular operating mode.

G. Kaltakkıran *et al.* (2022) performed an instantaneous energy balance during the warm-up of a spark-ignition petrol engine and demonstrated that, particularly under transient thermal conditions, the balance can be used to quantitatively elucidate relationship between thermal management strategies and the structure of losses. This is consistent with the results of presented study, which emphasises the mode-dependent nature of the dominant loss channels and the need to evaluate the effect of control via the balance in a specific mode, rather than based on an averaged picture. The selection of priority control actions in transient thermal conditions should be based on a mode-oriented balance analysis, which can direct control towards those loss channels that are decisive in the specific engine state.

The results of the study established that an increase in thermal efficiency through combustion control constitutes an optimisation within a feasible region bounded by thermomechanical and emission limits, as well as actuator and measurement constraints, disturbances and operational variability. The effectiveness of ECU is determined by the ability of algorithms to robustly maintain the combustion phase and key process indicators under conditions of noise and incomplete observability without violating safety limits. This is consistent with the approach of P. GhafGhanbari *et al.* (2024), who proposed a model-predictive control scheme with output feedback for a compression-ignition engine and emphasised that uncertainties, disturbances and limited measurements render “ideal” optimisation without explicit consideration of constraints potentially unstable or unsafe. Accordingly, improved thermal efficiency is achieved by optimising combustion control within permissible constraints, and the practically achievable effect is determined by the robustness of the algorithms and compliance with safety requirements. Z. Chen *et al.* (2025) demonstrated that combining model-predictive control with reinforcement learning is a practical approach for transitioning from static maps to adaptive multi-criteria control in transient conditions: model-predictive control is used as a guiding mechanism for the learning process, and the objective is set as a trade-off between nitrogen oxide emissions and engine performance indicators via the control of fuel delivery parameters (in particular, fuel rail pressure and injection parameters). This is consistent with the results of the current study, which emphasises that, due to non-linearity, variable operating conditions and "efficiency-emissions" trade-offs, there is a growing need for adaptive control approaches that explicitly consider constraints and safety requirements. Thus, the energy balance can be used to determine which losses dominate in a given engine operating mode and, accordingly, to select priority control actions. Improved thermal efficiency is achieved by optimising combustion and reducing auxiliary losses within thermomechanical, environmental and actuator constraints, which requires robust and adaptive control.

Comprehensive optimisation of operational processes and the energy balance of internal combustion engines

Optimisation of injection and ignition parameters is one of the most effective ways of improving the thermal efficiency of an internal combustion engine, as these controllable factors influence mixture formation, the heat release curve and the combustion phase. In practice, the task boils down to selecting parameters (injection timing/duration, pressure and pulse structure, ignition advance angle) that minimise specific fuel consumption or maximise efficiency whilst simultaneously meeting constraints regarding knock, emissions, thermal load, service life and the capabilities of the actuators. The basic formulation is constrained optimisation: an objective function (fuel consumption/efficiency) and a system of constraints (knock, peak pressure and its rise rate, temperature limits, emission limits, combustion stability, actuator constraints) (Yu *et al.*, 2022; Vlaswinkel *et al.*, 2025). For spark-ignition internal combustion engines, this manifests as optimisation of the ignition timing, where the optimum is constrained by knock and thermal load; for high-load modes with direct injection, changes in injection timing and pressure simultaneously affect both efficiency and emissions, resulting in a multi-criteria problem.

In practice, map calibration (RPM/load) is used in conjunction with optimisation algorithms (gradient, heuristic, surrogate and multi-criteria methods) to reduce the number of bench tests and account for constraints (Yu *et al.*, 2022). To improve the validity of the results, model-based optimisation is employed, which formalises the relationship between "control → combustion phase → losses → efficiency" (in particular for selecting the ignition timing whilst accounting for detonation). Data-driven approaches are also used, where machine learning models act as surrogates for predicting efficiency/emissions and for state estimation (Aliramezani *et al.*, 2021), whilst Bayesian optimisation with constraints ensures safe exploration of settings during costly experiments, considering the risk of exceeding limits (Vlaswinkel *et al.*, 2025). The need for multi-criteria optimisation is particularly evident under high-load conditions. The largest proportion of heat losses occurs in the cylinder-piston group due to heat exchange at high temperatures; improving thermal efficiency requires a targeted influence on the combustion process. Theoretical approaches to reducing these losses through automated control are summarised in Table 3.

Table 3. Theoretical approaches to reducing heat loss in the cylinder-piston group through automation

Method	Mechanism of effect on heat loss	Role of automated control
Balance approach	The conversion of energy from "wall/cooling" into output (or into exhaust)	Quantitative assessment of the effect based on the energy balance
Combustion phase control	Reduction in duration of high temperatures → lower total heat transfer	Maintenance of target combustion phase under different operating conditions
Restrictions on early burning	Avoiding excessive pressure/temperature peaks → lower heat fluxes in the component	Operation within thermomechanical limits
Stabilisation of process	Reduction of "bad cycles" (delays/instability) → lower average losses	Closed-loop combustion parameter control

Source: compiled by the authors based on M. Aliramezani *et al.* (2021), K. Watanabe *et al.* (2021), O.Y. Ahmed *et al*. (2022), D. Popa *et al.* (2022), O. Björnsson & P. Tunestal (2024)

The reduction in heat loss within the cylinder-piston assembly through automation is achieved not so much by a direct "reduction in heat exchange" as by a controlled modification of the combustion process, which redistributes energy within the engine's thermal balance in favour of output. The key factor is combustion phase control: maintaining the target phase reduces the duration of high-temperature conditions and minimises the probability of deviations that lead to increased losses. At the same time, the potential of this approach is limited by the need to avoid excessively early combustion, which sharply increases peak pressures/temperatures and heat fluxes in the component; therefore, optimisation inevitably takes place within thermomechanical limits. In this context, the balance approach serves as a tool for verifying the results: it can be used to quantitatively confirm that stabilising and optimising combustion does indeed reduce the proportion of energy dissipated into the walls and cooling, thereby translating into an increase in efficiency.

Improvements in effective thermal efficiency of internal combustion engines are determined not only by the quality of combustion, but also by the level of mechanical and auxiliary losses, which reduce the proportion of net output reaching the output shaft. Therefore, reducing friction in engine components and lowering the energy consumption of auxiliary systems (lubrication and cooling systems) represents a critical reserve for improving efficiency, particularly when combustion parameters are already close to optimal. In contrast to the "aggressive" approach of achieving thermodynamically favourable combustion conditions, reducing mechanical losses often improves efficiency without directly exacerbating trade-offs regarding emissions or knock resistance; however, it requires strict consideration of reliability and lubrication requirements. It is advisable to consider mechanical losses in two components: friction losses in the main assemblies (primarily in the cylinder-piston group and bearings) and losses in the drive of auxiliary units. In many configurations, the largest contribution comes from friction in the "piston-ring-cylinder liner" zone, so improving efficiency begins with tribological solutions. Coatings, optimisation of surface roughness and design changes in the power cylinder reduce friction losses and, consequently, improve efficiency by reducing the gap between rated and actual performance (Gangopadhyay, 2021). At the same time, the actual effect of such solutions depends on the temperature regime and the properties of the oil, which determine the nature of the lubrication.

The most direct method of increasing efficiency through automation relates to the control of auxiliary units, primarily the lubrication system. The oil pump ensures the necessary minimum permissible oil pressure and flow rate; however, an excess of these increases the energy consumption of the drive and reduces efficiency. Therefore, pump control must maintain pressure/flow at or above the limits set by the requirements of hydrodynamic lubrication and heat dissipation in bearings and the crankshaft, whilst avoiding excessive flow in operating modes where it is not required (Liu *et al.*, 2022). Pump control should be viewed as an optimisation problem with constraints: minimising energy consumption while maintaining lubrication safety and the permissible thermal state of friction components. In practice, this is achieved by adapting the pump's operating mode to oil temperature, speed and load, and by integrating this logic into the overall motor control system. Thus, reducing mechanical losses to improve thermal efficiency involves combining tribological measures to reduce friction with automated control of auxiliary units (in particular the lubrication system), whilst strictly adhering to service life and reliability constraints.

Automated control improves the thermal efficiency of internal combustion engines through two interrelated mechanisms: increasing the indicated fraction output by optimising mixture formation, the heat release law and combustion phasing; and reducing mechanical and auxiliary losses, which account for the difference between indicated power and output shaft. Real efficiency gains are achieved through coordinated control of fuel delivery, ignition, combustion parameters and auxiliary subsystems, considering reliability constraints and environmental requirements. At the indicator level, maintaining optimal combustion timing and process stability is key. At high loads, direct injection parameters influence the combustion process, efficiency and emissions; therefore, their selection is crucial in critical operating modes (Wang *et al.*, 2023). For spark-ignition engines, optimising the ignition timing is a constrained optimisation problem, where efficiency gains are limited by knock resistance and thermal load (Arsie *et al.*, 2024). To maintain optimal conditions across a wide range of operating modes, closed-loop combustion phase control algorithms are employed: model-predictive control coordinates process parameters whilst accounting for constraints, and closed-loop combustion phase optimisation reduces inter-cylinder variation and the probability of deviations from the effective zone. Promising learning-based approaches demonstrate the possibility of adaptive control of injection timing in complex multi-pulse processes, increasing adaptability to changing conditions (Henry de Frahan *et al.*, 2022).

At the output shaft level, automation delivers benefits by reducing friction losses and the power required to drive the units. Tribological solutions in the cylinder-piston assembly (coatings, surface roughness, design optimisations) reduce friction losses and directly improve efficiency. Optimal control of the units, particularly the lubrication system, is a key factor: the energy consumption of the oil pump drive depends on the operating mode and can be reduced provided that lubrication safety is maintained, which imposes constraints on the control algorithms. Such measures improve efficiency without directly exacerbating combustion trade-offs, but require integration into the control logic, incorporating resource and temperature limits (Gangopadhyay, 2021).

Practical gains in efficiency are impossible without high-quality calibration; optimisation algorithms make it possible to reduce the scope of testing and bring control maps closer to the optimal ones whilst adhering to constraints. Bayesian optimisation methods that take constraints into account further reduce the risk of breaching detonation and temperature limits whilst searching for efficient settings, and data-driven models reinforce these approaches in modelling and diagnostic tasks. At the same time, automation does not eliminate physical limits: as efficiency levels approach high values, thermomechanical and emission barriers dominate, defining the practical limit to further growth. Therefore, a correct assessment of the effect of automated control must be based on the energy balance, which determines which loss channel has contributed to the efficiency gain. Thus, the energy balance determines the dominant losses in the internal combustion engine and the priorities for reducing them. Automated control via the ECU improves efficiency by optimising fuel injection and ignition and managing subsystems within specified limits (knock, emissions, thermal load, service life), whilst the effect is assessed by changes in the proportions of losses in the balance.

The results of the study revealed that improving the thermal efficiency of internal combustion engines essentially boils down to optimising fuel injection and ignition as a constrained optimisation problem (involving constraints such as knocking, emissions, thermal load, service life and the limits of actuators), as well as to reducing the volume of bench testing through the use of models and optimisation procedures (in particular Bayesian optimisation) whilst maintaining safety requirements. This logic is supported by K. Esaki *et al.* (2022), demonstrating the practical implementation of automated machine learning for engine control parameters: during operation, the system autonomously collects data and adapts control to changes in the type/ratio of fuel mixtures, improving combustion efficiency and reducing the need for manual calibration. The application of algorithmic optimisation in calibration tasks can reduce the labour intensity of selecting control parameters and improve engine stability under changing operating modes and conditions.

The study by B. Hu *et al.* (2024) demonstrates the rapid calibration of a diesel engine injection map using grid-adaptive Bayesian optimisation, i.e., a practical tool for finding optimal settings with a limited number of tests. In contrast to the authors' focus on the online calibration procedure for a specific map, presented study considers optimisation calibration as part of the general formulation of "constrained optimisation", where the prior objective is not only to find parameters but also to explain through which loss channel (exhaust, cooling, mechanical/auxiliary) the gain is generated. Accordingly, algorithmic calibration is interpreted not merely as a means of reducing the number of experiments but as a mechanism for controlled entry into the permissible operating range, with the possibility of quantitatively verifying the effect via the energy balance. J.C. Peyton Jones *et al.* (2025) summarised feedback-based detonation control strategies and demonstrated that such control loops are a key mechanism for maintaining engine operation near optimal settings without breaching detonation and thermal limits. These findings are consistent with the present study; however, the present study includes detonation stability within a broader set of constraints (thermomechanical, emissions, actuator-measurement and operational variability) that define the feasible optimisation domain. Therefore, the practical improvement in efficiency is interpreted as the result of consistently maintaining the combustion phase within this range, where detonation feedback is a necessary but not the only element of safe control.

J. Tang *et al*. (2021) interpreted "Safe" search as a controlled approach to the detonation threshold: stochastic Bayesian optimisation is used to predict the detonation threshold and account for uncertainty, to approach the limit conditions without an uncontrolled transition into the detonation regime. In the results of this study, safety is formulated more broadly – as optimisation within a permissible operating region, where detonation is merely one of the constraints alongside peak pressure and its rate of rise, boundary temperatures/heat fluxes, emission limits, actuator limits and operational variability. Accordingly, whilst the authors' work addressed risk management regarding the violation of a single critical constraint (detonation), the presented study interprets the selection of optimal settings as ensuring simultaneous compliance with a set of constraints that collectively determine a practically achievable compromise between efficiency, toxicity and reliability. In both studies, the necessity of searching for settings near the boundary conditions is justified, with explicit consideration of uncertainty and the risk of constraint violation.

In general, an increase in the thermal efficiency of an internal combustion engine is achieved by optimising fuel injection and ignition as a constrained problem, where the determining factors are detonation, thermomechanical, emission and actuator-measurement limits. Practical efficiency gains are achieved not by seeking an "absolute maximum", but through the controlled selection of parameters within the permissible range, using models and algorithmic optimisation methods that reduce the labour intensity of calibration. Therefore, a key condition for implementing this potential is robust closed-loop control capable of maintaining operation near the boundary conditions, considering uncertainties and the risk of exceeding limits.

CONCLUSIONS

The results of the study showed that the energy (thermal) balance forms the basis for classifying losses by channel in a specific operating mode and for the informed selection of control measures. Varying the injection parameters, by influencing the heat release law and the combustion phase, alters the distribution of energy between output and losses, whilst the balance approach makes it possible to quantitatively determine which specific loss channel has contributed to the increase in efficiency. For transient thermal states, the study confirmed that the application of instantaneous energy balance can ling thermal control strategies to changes in the loss structure, thereby highlighting the mode dependence of the dominant components. The selection of injection, ignition and combustion phasing parameters should be viewed as a search for the optimum within the permissible operating range, defined by a set of constraints. Thermomechanical limits, detonation resistance and combustion stability, as well as environmental trade-offs between efficiency and emissions, are central. The practical feasibility of optimal settings is further determined by the capabilities of the actuators and the accuracy of measurements, necessitating robust and adaptive control algorithms with safety monitoring.

The role of the ECU as a closed-loop system ("sensors → algorithmic modules → actuators") has been summarised; this system coordinates fuel supply, ignition, gas exchange and auxiliary systems, whilst explicitly accounting for constraints. A correct assessment of the effect of automation must be based on changes in the proportions of losses in the overall energy balance, which distinguishes contribution of combustion control from contribution of reduced auxiliary and mechanical losses. For practical implementation, high-quality calibration is required, and optimisation algorithms (in particular Bayesian ones) reduce the volume of testing and lower the risk of violating constraints during the search for settings. In general, an increase in thermal efficiency is achieved through coordinated control of the combustion process and auxiliary subsystems within thermomechanical, environmental and actuator constraints, provided that control is stable and adaptive. A limitation of the study is its theoretical nature without bench validation. Future research should experimentally verify proposed approaches and develop coordinated closed-loop control of ignition and injection, with an assessment of the effect on the energy balance.

ACKNOWLEDGEMENTS

None.

FUNDING

None.

CONFLICT OF INTEREST

None.

REFERENCES

[1] Ahmed, O.Y., Middleton, R.J., Tran, V., Weng, A., Stefanopoulou, A.G., Kim, K.S., & Kweon, C.B. (2022). Model predictive control of combustion phasing in compression ignition engines by coordinating fuel injection timing and ignition assist. *IFAC-PapersOnLine*, 55(24), 90-96. doi: 10.1016/j.ifacol.2022.10.267.

[2] Aliramezani, M., Koch, C.R., & Shahbakhti, M. (2021). Modeling, diagnostics, optimization, and control of internal combustion engines via modern machine learning techniques: A review and future directions. *Progress in Energy and Combustion Science*, 88, article number 100967. doi: 10.1016/j.pecs.2021.100967.

[3] Arsie, I., Frasci, E., Irimescu, A., & Merola, S.S. (2024). Spark timing optimization through co-simulation analysis in a spark ignition engine. *Energies*, 17(15), article number 3695. doi: 10.3390/en17153695.

[4] Björnsson, O., & Tunestal, P. (2024). Evaluation of closed-loop combustion phase optimization for varying fuel compensation and cylinder balancing in a HD SI-ICE. *SAE Technical Paper*. doi: 10.4271/2024-01-2837.

[5] Chen, Z., Ju, P., Wang, Z., Shi, L., & Deng, K. (2025). Research on multi-objective optimization control of diesel engine combustion process based on model predictive control-guided reinforcement learning method. *Energy*, 325, article number 136173. doi: 10.1016/j.energy.2025.136173.

[6] Esaki, K., Shirakawa, Y., Naito, H., Matsumoto, K., & Ito, K. (2022). Automated machine learning of engine control parameters for various mixed fuels to help achieve carbon neutrality. *Hitachi Review*, 71(2), 56-60.

[7] Gangopadhyay, A. (2021). *Power cylinder friction reduction through coatings, surface finish and design*. Dearborn: Ford Motor Company.

[8] GhafGhanbari, P., Bao, Y., & Mohammadpour Velni, J. (2024). Uncertainty-aware output feedback model predictive combustion control of RCCI engines. *Control Engineering Practice*, 150, article number 106005. doi: 10.1016/j.conengprac.2024.106005.

[9] Güler, M., & Özkan, M. (2022). Energy balance analysis of a DI diesel engine with multiple pilot injections strategy and optimization of brake thermal efficiency. *Applied Thermal Engineering*, 204, article number 117972. doi: 10.1016/j.applthermaleng.2021.117972.

[10] Henry de Frahan, M., Wimer, N., Yellapantula, S., & Grout, R. (2022). Deep reinforcement learning for dynamic control of fuel injection timing in multi-pulse compression ignition engines. *International Journal of Engine Research*, 23(9), 1503-1521. doi: 10.1177/14680874211019345.

[11] Hu, B., Huang, Y., Zhang, F., & Liang, S. (2024). Online calibration algorithm for fuel injection MAP of unit-pump diesel engine based on mesh adaptive Bayesian optimization. *IFAC-PapersOnLine*, 58(29), 70-75. doi: 10.1016/j.ifacol.2024.11.122.

[12] Kaltakkıran, G., Ceviz, M.A., & Bakirci, K. (2022). Instantaneous energy balance and performance analysis during warm up period of a spark ignition engine under several thermal energy management strategies. *Energy Conversion and Management*, 269, article number 116102. doi: 10.1016/j.enconman.2022.116102.

[13] Kou, Y., Gao, Y., You, Y., & Wang, Y. (2022). Numerical investigation for optimization of spark-ignition internal combustion engine knock by Taguchi-Grey method. *Science Progress*, 105(4). doi: 10.1177/00368504221129280.

[14] Liu, Z., Cheng, L., & Zhai, X. (2022). Experimental study on the oil pump driving energy consumption and lubrication safety in a PFI engine under NEDC and WLTC. *Journal of Mechanical Science and Technology*, 36, 457-465. doi: 10.1007/s12206-021-1243-3.

[15] Lou, D., Rao, X., Zhang, Y., Fang, L., Tan, P., & Hu, Z. (2024). Investigation of impacts of hydrogen injection and spark strategy on knock in hydrogen engine. *International Journal of Hydrogen Energy*, 82, 1252-1262. doi: 10.1016/j.ijhydene.2024.08.052.

[16] Menaca, R., Silva, M., Uddeen, K., Almatrafi, F., Tang, Q., Turner, J.W., & Im, H.G. (2025). Optical multi-spark ammonia combustion engine: Numerical analysis and validation. *Frontiers in Mechanical Engineering*, 11, article number 1478081. doi: 10.3389/fmech.2025.1478081.

[17] Mittal, V. (2024). A review of recent advancements in knock detection in spark ignition engines. *Signals*, 5(1), 165-180. doi: 10.3390/signals5010009.

[18] National Academies of Sciences, Engineering, and Medicine. (2021). *Assessment of Technologies for Improving Light-Duty Vehicle Fuel Economy – 2025-2035*. Washington: The National Academies Press. doi: 10.17226/26092.

[19] Park, J., Shin, S., Oh, S., Lee, S., Shin, W., & Min, K. (2023). Knock onset determination with 1D CNN using random search hyperparameter optimization and data augmentation in SI engine. *International Journal of Automotive Technology*, 24, 1395-1410. doi: 10.1007/s12239-023-0113-7.
[20] Pereira, B.C., Pereira, B.S., Teixeira, E.L., Laganá, A.A., Cipparrone, F.A., & Santos, M.M. (2023). Design, implementation and testing of a spark-ignition engine management system. *Journal of Control, Automation and Electrical Systems*, 34, 554-565. doi: 10.1007/s40313-022-00978-z.
[21] Peyton Jones, J.C., Patel, V., & Frey, J. (2025). Knock feedback control strategies: A review. *Annual Reviews in Control*, 59, article number 100990. doi: 10.1016/j.arcontrol.2025.100990.
[22] Popa, D., Stan, C., Marin, N., Savu, N., & Ailincai, D. (2022). Study concerning the thermal energy balance in an internal combustion engine. *IOP Conference Series: Earth and Environmental Science*, 960, article number 012012. doi: 10.1088/1755-1315/960/1/012012.
[23] Ryaboshapka, N.Ye., Sukhonos, R.F., & Hrachov, P.V. (2023). Influence of ignition advance angle on the working processes of gasoline internal combustion engines operating on fuel with ethanol addition. In *Materials of the 14th international scientific and practical conference "Modern energy installations in transport, technologies and equipment for their service" (CEUTTOO-2023)* (pp. 163-164). Kherson: Kherson State Maritime Academy.
[24] Slynko, H.I., Yevsieieva, N.O., Kurylov, M.S., Sukhonos, R.F., & Slynko, V.V. (2022). Improving the characteristics of the MeMZ-317 engine with an LPG system by installing an ignition timing advance variator. *Innovative Materials and Technologies in Metallurgy and Mechanical Engineering*, 1, 78-80. doi: 10.15588/1607-6885-2022-1-13.
[25] Song, J., & Song, H.H. (2022). Spark-ignition engine speed profile optimization for maximizing the net indicated efficiency and quantitative analysis of the optimal speed profile. *Applied Energy*, 307, article number 118162. doi: 10.1016/j.apenergy.2021.118162.
[26] Tang, J., Pal, A., Dai, W., Archer, C., Yi, J., & Zhu, G. (2021). Stochastic Bayesian optimization for predicting borderline knock. *International Journal of Engine Research*, 24(3), 793-807. doi: 10.1177/14680874211065237.
[27] Vlaswinkel, M., Antunes, D., & Willems, F. (2025). Automated and risk-aware engine control calibration using constrained Bayesian optimization. *ArXiv*. doi: 10.48550/arXiv.2503.20493.
[28] Wang, J., Tian, H., Zhang, R., Shen, B., Su, Y., Yu, H., & Zhang, Y. (2023). Experimental investigation on the effects of direct injection timing on the combustion, performance, and emission characteristics of methanol/gasoline dual-fuel spark turbocharged ignition (DFSI) engine with different injection pressures under high load. *Energies*, 16(24), article number 7921. doi: 10.3390/en16247921.
[29] Watanabe, K., Uchida, N., Yokogawa, K., & Kawaharazuka, F. (2021). What are the barriers against brake thermal efficiency beyond 55% for HD diesel engines? *SAE Technical Paper*. doi: 10.4271/2021-24-0039.
[30] Yu, X., Zhu, L., Wang, Y., Filev, D., & Yao, X. (2022). Internal combustion engine calibration using optimization algorithms. *Applied Energy*, 305, article number 117894. doi: 10.1016/j.apenergy.2021.117894.
[31] Zhu, Q., Prucka, R., Wang, S., & Prucka, M. (2021). Online spark timing optimization with complex high-fidelity combustion phasing, knock, and coefficient of variation of IMEP models. *Journal of Dynamic Systems, Measurement, and Control*, 143(6), article number 061007. doi: 10.1115/1.4049733.

Віктор Дуганець
Доктор педагогічних наук, професор
Заклад вищої освіти «Подільський державний університет»
32316, вул. Шевченка, 12, м. Кам'янець-Подільський, Україна
https://orcid.org/0000-0002-3383-5907

Віталій Пукас
Кандидат технічних наук, доцент
Заклад вищої освіти «Подільський державний університет»
32316, вул. Шевченка, 12, м. Кам'янець-Подільський, Україна
https://orcid.org/0000-0002-0083-7359

Микола Волинкін
Магістр, асистент
Заклад вищої освіти «Подільський державний університет»
32316, вул. Шевченка, 12, м. Кам'янець-Подільський, Україна
https://orcid.org/0009-0006-4960-8537

Підвищення теплової ефективності двигунів внутрішнього згоряння шляхом автоматизованого керування робочими процесами

Анотація. Метою дослідження було проаналізувати замкнену стратегію керування, що коригує момент іскроутворення та подачу палива для зростання корисної роботи в циліндрі за умови детонаційної безпеки та зменшення циклової нестабільності. Методологія базувалась на методах енергетичного (теплового) балансового аналізу, класифікаційно-аналітичної систематизації, структурно-функціонального моделювання, порівняльного аналізу та аналітичного узагальнення. Встановлено, що теплова ефективність двигуна внутрішнього згорання (ДВЗ) — це відсоток енергії палива, який перетворюється в корисну роботу. Різниця між теоретичними і реальними показниками ефективності показує, скільки енергії втрачається через механічні та допоміжні процеси. Енергетичний баланс відображає розподіл енергії палива між корисною роботою на валу, тепловідведенням у систему охолодження, втратами з вихлопними газами та іншими видами втрат, дозволяючи визначити домінуючі напрямі її використання. Підвищення коефіцієнту користної дії обмежується зростанням тисків, температур і теплових навантажень, тому ключовим є оптимальне фазування тепловиділення, яке треба утримувати без детонації та надмірних піків. Виявлено, що параметри упорскування та запалювання формують фазування згоряння й індикаторну роботу, а оскільки упорскування змінює умови займання, кут запалювання має узгоджуватися з паливною стратегією (зокрема у замкненому контурі). Оптимізацію параметрів обмежують детонаційні, термомеханічні, емісійні та експлуатаційні чинники, які формують допустиму область налаштувань. Зазначено, що автоматизоване керування підвищує ефективність через оптимізацію сумішоутворення/фазування згоряння та через зменшення механічних і допоміжних втрат узгодженим керуванням підсистемами. Зниження механічних і допоміжних втрат досягається поєднанням трибологічних рішень і керування агрегатами для уникнення надлишкових енерговитрат. Застосування енергетичного балансу як критерію та узгоджене замкненоконтурне керування запалюванням, паливоподачею й допоміжними системами через електронний блок керування двигуном (ЕБКД) дає змогу зменшувати домінуючі втрати та підвищувати ефективність ДВЗ в межах детонаційних і термонавантажувальних обмежень. Практична значимість полягає у можливості застосування результатів інженерами з калібрування ЕБКД під час стендових випробувань і налаштувань двигуна на транспорті

Ключові слова: детонація; запалювання; упорскування; обмеження; фазування згоряння

Machinery & Energetics
Vol. 17, No. 1. 2026

Journal homepage:
https://technicalscience.com.ua/en

UDC 621.396.67
DOI: 10.31548/machinery/1.2026.55

ISSN 2663-1334
e-ISSN 2663-1342

Hryhorii Radzivilov
PhD in Technical Sciences, Associate Professor
Kruty Heroes Military Institute of Telecommunications and Information Technology
01011, 45/1 Knyaziv Ostrozkykh Str., Kyiv, Ukraine
https://orcid.org/0000-0002-6047-1897

Dmytro Pavliuk*
Adjunct
Kruty Heroes Military Institute of Telecommunications and Information Technology
01011, 45/1 Knyaziv Ostrozkykh Str., Kyiv, Ukraine
https://orcid.org/0000-0001-8461-3899

Mathematical model of the functioning of a mobile radio communication system built on software-defined means

Abstract. The purpose of the study was to develop a generalised mathematical model of the functioning of multi-antenna radio communication systems under the influence of random and intentional interference and to analytically describe the influence of interference-noise and non-stationary factors on the security and reliability of information transmission. The work used a matrix channel model, space-time block coding, orthonormal representation of signals in a common signal space and statistical modelling of noise and interference in the coordinates of the basis. The results of the study showed that under quasi-stationarity of the channel on the interval of block transmission and orthogonality of the space-time structure, an inverse channel operator was formed. Under such conditions, linear recovery of the transmitted symbol vector and coherent summation of the useful component were ensured with statistical independence of noise components at the decoder output. The desired signal, fluctuating noise, and intentional interference had a consistent coordinate structure in the same orthonormal signal space. As a result, the quality of each antenna channel was determined by the energy balance between the desired energy and the spectral parameters of noise and interference, which determined the distance of signal points from the regions of false decision. The constellation degradation was described by the composition of geometric transformations (rotation, scaling, quadrature deformation) and stochastic perturbations (phase jitter, interference, additive noise), and the parameters of these distortions were identified by the mathematical expectation, dispersion, and covariance of the coordinates of the received symbols. The temporal nonstationarity of the channel was determined by the Doppler shift and the correlation structure of the transmission coefficient, and the elliptical geometric scattering model related the delays of multipath components to the spatial configuration of the scatterers. The practical significance of the results lay in the possibility of using the proposed model for analysis and optimisation of multi-antenna radio systems on software-defined devices in conditions of noise, interference and non-stationary channel. Its application contributed to the justification of modulation and coding parameters, as well as to increasing the reliability and interference immunity of radio communications

Keywords: space-time coding; additive noise; intentional interference; MIMO; software-defined radio; Doppler effect

INTRODUCTION

Mathematical modelling of a radio channel in multi-antenna communication systems occupies a key place in modern radio engineering and telecommunications, since it is aimed not so much at describing individual implementations

Article's History: Received: 12.11.2025; Revised: 03.02.2026; Accepted: 26.02.2026; Published: 30.03.2026.

Suggested Citation:
Radzivilov, H., & Pavliuk, D. (2026). Mathematical model of the functioning of a mobile radio communication system built on software-defined means. *Machinery & Energetics,* 17(1), 55-72. doi: 10.31548/machinery/1.2026.56.

*Corresponding author

of the signal as at establishing the structural properties of the channel, its statistical stability, sensitivity to parameters, correctness of channel state estimation and prediction of reception errors in real electromagnetic conditions. Unlike simplified models focused on idealised conditions, the applied approach for mobile Software-Defined Radio (SDR) systems requires simultaneous consideration of spatial correlation between antennas, non-stationarity due to the movement of the transmitter and receiver, Doppler shift, multipath propagation, intersymbol interference, phase shifts and phase jitter, as well as intentional interference of various types, which directly determine noise immunity and Multiple Input Multiple Output (MIMO).

In modern research, more and more attention is paid to models and methods that combine a realistic description of spatially correlated MIMO channels with mechanisms for channel estimation, interference detection, and decision support for software-defined radio systems. In particular, the work of H. Khudov *et al.* (2023) showed the practical value of SDR receivers for the tasks of determining the coordinates of low-visibility aerial objects. According to the conclusions, the accuracy of signal processing in such systems significantly depends on an adequate description of the radio channel and its coordination with signal processing algorithms under conditions of signal degradation. In the next work, H. Khudov *et al*. (2021) proposed a method for determining the coordinates of aerial objects using Automatic Dependent Surveillance-Broadcast (ADS-B) receivers. Such hybrid surveillance systems increase the requirements for mathematical models of the radio channel, which must correctly take into account the influence of noise, interference, and uncertainties in the signal propagation environment. The influence of the interference environment on the efficiency of signal processing has also been confirmed by experimental studies of radar systems. V.P. Riabukha *et al.* (2022) compared adaptive and non-adaptive Moving Target Indication (MTI) systems in pulsed radar stations of various applications and ranges, showing the dependence of signal processing efficiency on the characteristics of the interference and channel environment.

Similar problems arise in modern communication systems with massive MIMO. In particular, the tasks of detecting intentional jamming and channel estimation have become significant precisely for spatially correlated configurations. P. Du *et al*. (2026) considered the joint formulation of jamming detection and channel estimation for beamspace massive MIMO, thereby fixing the need for models that include interference as an integral element of the channel state, rather than as an external "superstructure". Similarly, J. Amadid *et al*. (2022) investigated the features of channel parameter estimation and spectral efficiency in cell-free massive MIMO with multichannel access points taking into account spatial correlation. The authors showed that the channel correlation structure can limit the gain from multi-antenna, so it must be explicitly taken into account in the mathematical model.

The universality of the spatial correlation problem is also confirmed by studies in other multichannel communication technologies. For example, L. Zhao *et al*. (2024) demonstrated the criticality of correlation for visible light massive MIMO systems with "antenna" selection based on the Pearson coefficient. Further development of resource management methods in massive MIMO for spatially correlated channels is reflected in the study of A. de la Fuente *et al.* (2022), where user subgrouping and power control for multicast are directly related to the channel correlation structure and its impact on the coherence of spatial multiplexing.

A separate line of modern work is formed by approaches using Reconfigurable Intelligent Surfaces (RIS), in which the channel model must take into account not only propagation statistics, but also controlled reflection as an element of the system architecture. In particular, E. Shi *et al*. (2022) analysed cell-free massive MIMO systems with RIS support in spatially correlated channels, showing that correlation determines both the efficiency of signal matching and the limits of gain from additional reflective degrees of freedom. In the work of Z. Sui *et al.* (2025), RIS-assisted cell-free massive MIMO with modulation of reflection patterns is considered, where the controlled reflective contour actually changes the structure of the effective channel and requires models that can correctly describe the "switching" of reflective configurations in space and time. Further, A. Papazafeiropoulos *et al*. (2024) investigated the achievable speed in massive MIMO Simultaneously Transmitting and Reflecting Reconfigurable Intelligent Surface (STAR-RIS) for spatially correlated channels, emphasising that the correctness of the throughput prediction depends on the consistent consideration of correlation and parameters of the guided wave transmission/reflection.

Despite the presence of a significant number of studies devoted to the modelling of MIMO systems, in the modern scientific literature there is a need to develop a generalised mathematical model capable of simultaneously taking into account spatial correlation, transmitter and receiver motion, Doppler non-stationarity, noise effects, intentional interference and other signal degradation factors with moderate computational complexity. Existing approaches are mainly focused on individual aspects of channel operation and do not provide a holistic description of the interaction of destabilising factors within a single analytical scheme. This necessitates the development of a model that would allow for a more adequate description of the operating conditions of multi-antenna radio communication systems and create a basis for further analysis of the interference immunity and reliability.

The purpose of the study was to develop a consistent analytical scheme for the operation of multi-antenna radio communication systems under the influence of random and intentional interference, as well as to establish the influence of interference-noise and non-stationary factors on the security and reliability of information transmission. To achieve the goal of the study, the following tasks were set: to form a generalised model of the channel state of a multi-antenna radio communication system taking into account spatial correlation, transmitter and receiver motion, and Doppler non-stationarity; to formalise a model of interference-noise influence, which includes additive white Gaussian noise, intentional interference, intersymbol interference, phase distortions, and other signal degradation factors.

MATERIALS AND METHODS

The study was of a theoretical-analytical nature and was based on analytical-statistical modelling of multi-antenna radio communication systems. The work used matrix relations for the MIMO channel, stochastic noise and interference models, statistical fading models (Rayleigh, Rice, Nakagami, Rice-Nakagami), as well as parameterised models of non-stationary multipath propagation, suitable for consistent consideration of the motion of the transmitter and receiver and changes in the correlation structure of the channel in time.

The basic relationship between the transmitted and received signals was given by the matrix model of the MIMO channel in the form:

$$X(t) = H(t)A(t) + n(t) + j(t), \quad (1)$$

where $A(t)$ – the vector (or matrix) of transmitted complex symbols at time t; $X(t)$ – the vector (or matrix) of received complex symbols; $H(t)$ – the channel matrix (complex matrix of transmission coefficients); $n(t)$ – the additive noise (in particular, the thermal noise of the receiver); $j(t)$ – the intentional interference; t – the time.

The matrix of the multipath channel was given in the form of formula:

$$H(t) = \begin{bmatrix} h_{11}(t) & h_{12}(t) & \cdots & h_{1J}(t) \\ h_{21}(t) & h_{22}(t) & \cdots & h_{2J}(t) \\ \vdots & \vdots & \ddots & \vdots \\ h_{I1}(t) & h_{I2}(t) & \cdots & h_{IJ}(t) \end{bmatrix}, \quad (2)$$

where $h_{ij}(t)$ – the complex transmission coefficient between the i-th transmitting antenna and the j-th receiving antenna; I – the number of transmitting antennas; J – the number of receiving antennas. The random nature of the amplitude-phase relations in $h_{ij}(t)$ was interpreted through typical scenarios of the absence or presence of a pronounced direct component corresponding to a Rayleigh or Rician channel.

For a consistent description of signals in a multichannel structure, the representation of each of the v-signals as a projection onto an orthonormal basis of functions on the time interval T was used:

$$x_{Lm}(t) = \sum_{n=1}^{L} x_{Lmn}\ \omega_{Ln}(t) \ldots,$$
$$x_{vm}(t) = \sum_{n=1}^{L} x_{vmn}\ \omega_{vn}(t), \quad (3)$$

where m – the signal (symbol) index; L – the number of basic functions; v – the number of channels (antenna branches); $\omega_{Ln}(t)$ – the orthonormal basis functions; x_{Lmn} – the coefficients of the orthonormal decomposition (projection).

This representation corresponded to the standard procedure for transitioning from a continuous signal to complex symbols after matched filtering and discretisation. In this case, the elements of the vectors $A(t)$ and $X(t)$ in model (1) were interpreted as the coefficients of the orthonormal decomposition of the signal.

The decomposition coefficients were defined as formula:

$$x_{Lmn} = \int_0^T x_{Lm}(t)\ \omega_{Ln}(t)\, dt, \ldots,$$
$$x_{vmn} = \int_0^T x_{vm}(t)\ \omega_{vn}(t)\, dt, \quad (4)$$

where T – the duration of the transmission interval of an elementary unit of information.

The energy limit for the L-th channel was given by the relation:

$$\int_0^T x_{Lm}^2(t)\, dt = E_L, L = \overline{1,v}, \quad (5)$$

where E_L – the signal energy in the L-th channel (antenna branch) for the interval T.

The stochastic noise component was modelled as fluctuation noise in the basis representation:

$$n_L(t) = \sum_{n=1}^{N} n_{Ln}\ \omega_{Ln}(t), \ldots, n_v(t) = \sum_{n=1}^{N} n_{vn}\ \omega_{vn}(t), \quad (6)$$

where n_{Ln} – random noise coefficients; N – number of basis components taken into account; v – number of channels. The coefficients n_{Ln} were assumed to be Gaussian with zero mean and variance $G_{L0}/2$, and the probability densities were given as formulas:

$$w_1(n_{Ln}) = \xi_L\left(0, \frac{G_{L0}}{2}\right) = \frac{1}{\sqrt{\pi G_{L0}}} \exp\left(-\frac{(n_{Ln})^2}{G_{L0}}\right), \quad (7)$$

$$w_v(n_{vn}) = \xi_v\left(0, \frac{G_{v0}}{2}\right) = \frac{1}{\sqrt{\pi G_{v0}}} \exp\left(-\frac{(n_{vn})^2}{G_{v0}}\right), \quad (8)$$

where G_{L0} – the parameter characterising the spectral energy of noise in the L-th channel.

Intentional interference was uniformly modelled as additive white Gaussian noise (AWGN) in the basis representation:

$$j_L(t) = \sum_{n=1}^{L} j_{Ln}\ \omega_{Ln}(t), \ldots, j_v(t) = \sum_{n=1}^{L} j_{vn}\ \omega_{vn}(t), \quad (9)$$

where j_{Ln} – independent random noise coefficients with zero mean; the variances were equal to $G_{Lz}/2$. The corresponding probability densities were represented via formulas:

$$w_L(j_{Ln}) = \eta_L\left(0, \frac{G_{Lz}}{2}\right) = \frac{1}{\sqrt{\pi G_{Lz}}} exp\left(-\frac{j_{Ln}^2}{G_{Lz}}\right), \quad (10)$$

$$w_v(j_{vn}) = \eta_v\left(0, \frac{G_{vz}}{2}\right) = \frac{1}{\sqrt{\pi G_{vz}}} exp\left(-\frac{j_{vn}^2}{G_{vz}}\right), \quad (11)$$

where G_{Lz} – a parameter that characterised the spectral energy of intentional interference in the L-th channel.

The integral energy characteristic of the interference was given as formula:

$$\int_0^T J_L^2(t)\, dt = G_{Lz}, \quad (12)$$

where $J_L(t)$ – the implementation of the interference signal in the L-th channel.

The reception quality in each L-th channel was determined by the signal-to-noise ratio (SNR):

$$SNR_L = \frac{E_L}{G_{L0}} = \frac{P_L}{P_{L0}}, \quad (13)$$

where E_L – energy of the useful signal; G_{L0} – spectral energy of noise; P_L – effective radiated power in the L-th channel; P_{L0} – noise power in the L-th channel.

The signal-to-noise ratio SIR at the demodulator output was given as formula:

$$SIR_L = \frac{P_L}{P_{Lz}} = \frac{P_L}{G_{Lz}}, \quad (14)$$

where P_{Lz} – the power of intentional interference in the L-th channel; G_{Lz} – the parameter of the spectral energy of the interference (in the accepted definition of the comparison scale).

Multipath propagation was described by a discrete-path model in the form formula:

$$u_x(t) = \sum_{l=1}^{\Xi} C_{(l \cdot \partial \cdot r)}\, \Psi_{(r \cdot c \cdot l)}\, u(t-\tau_l) + +n(t), 0 < t < +\infty, \quad (15)$$

where $u_x(t)$ – the signal at the receiver input after passing through the channel; Ξ – the number of propagation paths; l – the path index; τ_l – the delayof the l-th path; $u(t-\tau_l)$ – a time-shifted copy of the transmitted signal; $C_{(l,\partial,r)}$ – the complex coefficient (amplitude and phase) of the signal-code structure for the l-th path in the ∂-th symbol of the r-th frame; $\Psi_{(r,c,l)}$ – the generalised component of the channel model that integrated destabilising factors (in particular, correlation, non-stationary and interference); $n(t)$ – additive noise; t – time. The research area covered the time axis $t \in (0, +\infty)$ and space of complex channel coefficients and signals in each antenna branch, as well as the procedures for transitioning from channel parameters to reception error estimates for phase-shift keying M (FM-M), quadrature amplitude modulation M (QAM- M), and hierarchical quadrature amplitude modulation M (IQAM-M) under fading and intentional interference conditions.

The methodological logic of the study was based on a combination of matrix modelling of the MIMO channel with independent modelling of antenna branches and subsequent aggregation into complex indicators of reception quality, as well as on statistical identification of distortion parameters by momentary characteristics of received symbols. Procedurally, the model was built as a sequence of channel symbol transformations in each channel, with the separation of deterministic geometric transformations of the constellation and random processes that determined signal degradation.

At the first stage, the reception process was formalised as a superposition of the useful signal and noise-interference components in the form:

$$\hat{z}(t) = z(t) + n(t), \quad (16)$$

where $\hat{z}(t)$ – the observed input signal of the receiver; $z(t)$ – the useful component after passing through the channel; $n(t)$ – additive noise; t – time.

The transition from a "pure" channel symbol to an observed one was described by adding interference in the symbol and the channel:

$$\hat{C}_{(\partial \cdot l)} = C_{(\partial \cdot l)} + n_{(\partial \cdot l)}, \quad (17)$$

where $C_{(\partial,l)}$ – complex channel symbol for symbol in the l-th channel; $\hat{C}_{(\partial,l)}$ – observed channel symbol; $n_{(\partial,l)}$ – disturbance (a combination of noise, interference and/or clutter) in the corresponding symbol and channel; ∂ – symbol index; l – channel index (antenna branch).

The channel symbol was given as a matrix of real and imaginary parts:

$$c_{(\partial \cdot l)} = \begin{bmatrix} \Re\{C_{(\partial \cdot l)}\} \\ \Im\{C_{(\partial \cdot l)}\} \end{bmatrix}, \hat{c}_{(\partial \cdot l)} = \begin{bmatrix} \Re\{\hat{C}_{(\partial \cdot l)}\} \\ \Im\{\hat{C}_{(\partial \cdot l)}\} \end{bmatrix}, \quad (18)$$

where $\Re\{\cdot\}$ and $\Im\{\cdot\}$ – the real and imaginary parts of a complex quantity. This allowed describing the set of distortions as a composition of controlled constellation transformations and random processes.

The phase shift was formalised by rotating the constellation by an angle φ:

$$\hat{c}_{(\partial \cdot l)} = R(\varphi)\, c_{(\partial \cdot l)}, R(\varphi) = \begin{bmatrix} \cos\varphi & -\sin\varphi \\ \sin\varphi & \cos\varphi \end{bmatrix}. \quad (19)$$

The amplitude mismatch between the real and imaginary branches was given by different gain coefficients:

$$\hat{c}_{(\partial \cdot l)} = G\, c_{(\partial \cdot l)}, \quad (20)$$

$$G = \begin{bmatrix} k_I & 0 \\ 0 & k_Q \end{bmatrix}, \quad (21)$$

where k_I and k_Q – amplification factors for I- and Q-components.

The quadrature error was described by the mutual rotation of the quadrature components:

$$\hat{c}_{(\partial \cdot l)} = R(\theta_{IQ})\, c_{(\partial \cdot l)}, \quad (22)$$

where θ_{IQ} – quadrature error parameter (angle of mutual displacement of axes I/Q).

The influence of intersymbol interference and additive noise was specified through the decomposition of interference into components:

$$n_{(\partial \cdot l)} = n_{(\partial \cdot l)}^{(ISI)} + n_{(\partial \cdot l)}^{(AWGN)}, \quad (23)$$

where – component caused by the overlap of neighbouring symbols (intersymbol interference); – additive component with uniform spectral distribution.

Phase jitter was considered as a dynamic random process of random rotation of the constellation, for which the angle θ_i obeyed the normal law:

$$\theta_i \sim N(0, \sigma_i^2), \quad (24)$$

where σ_i^2– phase jitter dispersion; $N(\cdot)$ – normal distribution.

Generalisation of transformations formula (20)-(24) led to an integral representation of the observed symbol as a composition of deterministic matrix transformations and random perturbations:

$$\hat{c}_{(\partial, l)} = T_{(\partial, l)}\, c_{(\partial, l)} + n_{(\partial, l)}, T_{(\partial, l)} = R(\varphi)\, G\, R(\theta_{IQ})\, R(\theta_i), \quad (25)$$

where $T_{(\partial, l)}$ – the effective constellation transformation matrix in the (∂, l)-position; $R(\theta_i)$ – the random rotation matrix induced by phase jitter.

Next, a statistical procedure for estimating model parameters based on the moments of received symbols was applied. Assuming small phase fluctuations (or small angular parameters), a linearised approximation of the mathematical expectations of the components of the observed symbol was performed:

$$\mathbb{E}\left[\Re\left\{\hat{C}_{(\partial,l)}\right\}\right] = \mathbb{E}\left[a_1\Re\left\{C_{(\partial,l)}\right\} - a_2\Im\left\{C_{(\partial,l)}\right\}\right],$$
$$\mathbb{E}\left[\Im\{\hat{C}_{(\partial,l)}\}\right] = \mathbb{E}\left[a_3\Re\{C_{(\partial,l)}\} - a_4\Im\{C_{(\partial,l)}\}\right], \quad (26)$$

where a_1, a_2, a_3, a_4 – generalised coefficients that accumulated the influence of amplification, mutual transformation of quadratures and components of the interference circuit; $\mathbb{E}[\cdot]$ – mathematical expectation operator.

The phase jitter variance was estimated through the covariance of the real and imaginary parts of the observed symbol (27):

$$Cov\left(\Re\left\{\hat{C}_{(\partial,l)}\right\}, \Im\left\{\hat{C}_{(\partial,l)}\right\}\right) = -\kappa\, \sigma_i^2\, \Phi\left(C_{(\partial,l)}\right), \quad (27)$$

where $Cov(\cdot, \cdot)$ – covariance; κ – generalised scale constant (depended on the transformation structure $T_{(\partial, l)}$; $\Phi(C_{(\partial, l)})$ – a function that depended on the coordinates of the "pure" symbol and the parameters of static transformations.

The intensity of the interference component was characterised by the index A, which was determined through a combination of dispersions and high-order central moments (28):

$$A = F\left(Var\left[\Re\{\hat{C}_{(\partial,l)}\}\right], m_4\left(\Re\{\hat{C}_{(\partial,l)}\}\right)\right), \quad (28)$$

where $Var[\cdot]$ – dispersion; $m_4(\cdot)$– central moment of the fourth order; $F(\cdot)$ – the interference intensity function defined in the model.

After that, the characteristics of intentional interference and noise were related to the variances of the components of the received symbol (formula (29)):

$$Var\left[\Re\left\{\hat{C}_{(\partial,l)}\right\}\right] = G_R(\sigma_i^2, A) + Var\left[\Re\{n_l\}\right],$$
$$Var\left[\Im\left\{\hat{C}_{(\partial,l)}\right\}\right] = G_I(\sigma_i^2, A) + Var\left[\Im\{n_l\}\right], \quad (29)$$

where $n_{(l)}$ – the additive noise-interference component in l-th channel; $G_R(\cdot)$ and $G_I(\cdot)$ – the model distribution functions of the dispersion contribution of phase fluctuations and interference in the corresponding quadratures. Thus, the method provided separation of the contributions of phase fluctuations, interference and additive noise/interference by statistically observed quantities in each antenna branch.

At the second stage, correlation-frequency characteristics within the Jakes model were used to model nonstationarity and Doppler structure, where the autocorrelation function and spectral distribution over Doppler frequencies were given as:

$$R(\tau) = J_0, (2\pi f_D \tau), P(f) = \frac{1}{\pi f_D \sqrt{1-(f/f_D)^2}}, | f | < f_D, \quad (30)$$

where $R(\tau)$ – autocorrelation function; $P(f)$ – spectral power density at Doppler frequencies; τ – time shift; f – Doppler frequency; f_D – maximum Doppler shift; $J_0(\cdot)$ – zero-order Bessel function.

For complex urban scenarios, an elliptical approach with two scattering ellipses was used, in which the parameters of the outer and inner contours were determined by time delays and motion geometry. The formalisation of the delays was carried out by the relation:

$$\tau_m = \frac{D_m}{c}, \quad (31)$$

where τ_m – the largest signal delay (for the limiting propagation route); D_m – appropriate length of the route; c – the speed of propagation of an electromagnetic wave.

The conditions for the formation of the reflected component and the correct consideration of the geometry of the antenna placement were set by the criterion:

$$d \geq \frac{4h_t h_r}{\lambda}, \quad (32)$$

where d – the distance between the transmitter and the receiver; $h_{(t)}$ and h_r – antenna heights; λ – wavelength.

The Doppler shift for motion along an arbitrary path was defined as formulas:

$$f_D = \frac{v}{\lambda} \cos\, \beta, \quad (33)$$

$$\Delta f(t) = \frac{v(t)}{\lambda} \cos\, \beta(t), \quad (34)$$

where v or $v(t)$ – the relative speed of movement; β or $\beta(t)$ – the angle between the velocity vector and the direction of wave arrival.

The generalised instantaneous transfer characteristic of the channel was formed in:

$$h(t) = \sum_{(i=0)}^{N} g_i\, exp\,(j(2\pi\Delta f_i\, t + \theta_i + \phi_i)\, u(t - t_i), \quad (35)$$

where $h(t)$ – complex transfer characteristic; N – number of propagation paths; g_i – weighting factor (energy ratio of the i-th path); Δf_i – Doppler shift for the i-th path; θ_i – phase shift; ϕ_i – arbitrary initial phase; $u(\cdot)$ – step function; t_i – delay of the i-th path; j – imaginary unit.

At the third stage, an analytical assessment of noise immunity was carried out through the bit error rate (BER) for phase shift keying *M*-arn (FM-M), quadrature amplitude shift keying *M*-arn (QAM-M) and hierarchical quadrature amplitude shift keying *M*-arn (IQAM-*M*) in channels with fading and intentional interference. For FM-*M* in frequency-selective channels with additive noise and coherent reception, the bit error probabilities were given by the relation:

$$P_{(b,\,i)} = F_i(SNR, M, i),\ i = 1,\dots, B. \quad (36)$$

where $P_{(b,\,i)}$ – the probability of a bit i error; M – the constellation dimension; B – the number of bits in the block; $F_i(\cdot)$ – the function given by the analytical formulas of the model.

In this case, for the first two bits, separate partial cases of this dependence were used, while for bits with numbers, $i = 3,\dots, B$ a generalised notation was used, taking into account the bit position number.

The auxiliary functions and angular parameters included in $F_i(\cdot)$ were given as formulas:

$$T_z(\cdot) = T(\cdot), \quad (37)$$

$$\psi_m = \mathrm{P}(M, m), \quad (38)$$

where $T(\cdot)$ and $P(\cdot)$ – analytical expressions were defined in the model that ensured correct consideration of constellation geometry and bit mapping.

The average error probability in a *B*-bit block was determined by averaging (formula (39)):

$$P_B = \frac{1}{B}\sum_{i=1}^{B} P_{b,i}, \quad (39)$$

For KAM-*M* and IKAM-*M* generalised relations were used, these relations took into account the parameters of the constellation, fading, and hierarchical structure: the basic form was given as:

$$P_{(b,\,1:2)} = G(SNR, M, \alpha, \lambda^2), \quad (40)$$

with auxiliary quantities:

$$g = G(M, \alpha, \cdot), \quad (41)$$

and the extension for all bits of the block:

$$P_{(b,\,i)} = G_i(SNR, M, \alpha, \lambda^2, i),\ i = 3, \overline{B}, \quad (42)$$

after which the total error probability was aggregated as:

$$P_B = H\left(\{P_{b,i}\}_{i=1}^{B}\right), \quad (43)$$

and in exact form was written as formula:

$$P_B = H_{exact}(SNR, M, \alpha, \lambda^2). \quad (44)$$

In these relations α – the hierarchy parameter (for classical QAM $\alpha = 1$, for hierarchical – $\alpha > 1$); λ^2 – the parameter characterising the ratio of regular and fluctuation components in Rician scenarios; $G(\cdot)$, $G_i(\cdot)$, $H(\cdot)$, $H_{exact}(\cdot)$ – analytical expressions of the model that take into account the minimum Euclidean distances and the priority of subflows.

The bit weight coefficients $\{\alpha_{2j-1}\}$, which parameterised the contribution of critical transitions in the constellation, were given as:

$$\alpha_{2j-1} = \alpha_{2j-1}(M), \quad (45)$$

where j – the coefficient index, and the specific values $\alpha_{2j-1}(M)$ – determined by the selected mapping of bits to the constellation and the adopted variant of analytical formalisation.

The final aggregation of the error for the multichannel structure was carried out by averaging over the L antenna channels in the form:

$$P_B^{(L)} = \frac{P_{B,1} + P_{B,2} + \dots + P_{B,L}}{L}, \quad (46)$$

where $P_B^{(L)}$ – the average bit error probability for the multichannel structure; $P_{(B,l)}$ – the average fraction of bits received with error in the l-th antenna branch, taking into account selective fading, Doppler non-stationarity, intersymbol interference, phase jitter, and intentional interference.

As a result, the applied methodological approach provided a formalised combination of a matrix description of the MIMO channel, stochastic modelling of noise and intentional interference, a non-stationary geometric description of the moving environment, and a statistical estimation of distortion parameters based on the momentary characteristics of received symbols, which created the basis for a consistent analytical estimation of the bit error rate in spatially correlated channels in line-of-sight (LoS) and non-line-of-sight (NLoS) modes with controllable computational complexity.

RESULTS

Structure of signal transmission in MIMO system and conditions for spatial symbol recovery

Analysis of the structure of signal transmission in a multi-antenna system was performed for the matrix model of the channel under conditions of multi-path signal propagation, when the interaction between the transmitting and receiving antennas is described by the channel operator given by the relations formulas (1), (2). In this formulation, the transmitted symbol vector was considered as an element of the signal space, which under the action of the channel operator is mapped into the vector of received signals. The structure of the channel matrix in this case determines the geometry of the interaction of the antenna branches and sets the nature of the spatial mixing of signals at the receiver.

It was established that if the conditions of quasi-stationarity of the channel during the transmission interval of a block pair of symbols and if the conditions of orthogonality of the space-time structure of the signal are met, the channel operator acquires the property of reversibility. This means that the system formulas (1), (2) allows a fundamental linear transformation of the received signal, which allows recovering the transmitted symbol vector without loss of information. In the signal space, a mapping is formed for which the received vector is a scaled projection of the initial information vector. In other words, the action of the channel operator is reduced to a linear transformation that changes the scale and orientation of the signal in the antenna coordinate space, but does not violate the possibility of its recovery under the condition of linear independence of the columns of the channel matrix. Thus, signal decoding can be implemented through the corresponding linear transformation of the received signal, which actually performs the role of a space-time decoder.

The interpretation of this result is related to the geometric structure of signals in the multidimensional space of antenna channels. Orthogonal space-time coding forms a signal system in which individual information symbols are transmitted along mutually orthogonal directions of the signal space. As a result, coherent summation of the useful signal components occurs on the receiving side, while the noise components remain statistically independent. This property leads to an increase in the effective signal-to-noise ratio and ensures the stability of the information recovery process even in the presence of random fluctuations in the channel parameters. Analysis of the obtained relations showed that the geometry of the channel matrix determines the structure of the signal space of the transmission system. If the columns of this matrix remain linearly independent, each information symbol corresponds to its own direction in the space of antenna channels, and the mutual influence of information flows remains limited. Under these conditions, the spatial modes of the signal retain the identifiability, and the decoding process is reduced to restoring the corresponding coordinates in the signal space. To generalise the obtained result, the parameters of the signal transmission model that determine the channel geometry can be presented in the form of a systematised set of characteristics given in Table 1.

Table 1. Logic diagram for obtaining spatial symbol recovery conditions in a MIMO system

Analysis stage	Ratios used	Result obtained
Formalisation of the signal transmission model	(1)	A matrix relationship is established between the transmitted and received signals
Multipath channel structure	(2)	The geometry of the interaction of the transmitting and receiving antennas is determined
Space-time block coding	(3)	The condition for linear recovery of the vector of transmitted symbols is obtained

Source: compiled by the authors

The key element of the signal transmission structure in a multi-antenna system is the coordination of the channel matrix model with the spatiotemporal organisation of signals. Relation (1) specifies the general operator form of signal transformation during passage through the channel and determines the linear nature of the interaction between the transmitted and received signals. At the same time, the structure of the channel matrix, described by relation (2), reflects the multipath nature of signal propagation and specifies the geometry of the signal space in which information is transmitted. Further analysis showed that the use of space-time block coding, described by relation (3), leads to the formation of a special block structure of the channel operator. This structure ensures linear independence of signal components and creates conditions for the correct recovery of the transmitted symbol vector on the receiving side. Thus, the system of formulas (1), (2) allows for the existence of a linear transformation, which allows decoding the signal by projecting the received vector onto the corresponding basis of the signal space.

The obtained result means that a set of spatially separated signal modes is formed in the antenna coordinate space. Each such mode corresponds to a separate information flow and is characterised by its own energy weight, which is determined by the coefficients of the channel matrix. In this case, the action of the channel leads to scaling and rotation of the signal vector in the antenna coordinate space, but does not violate the structure of the spatial separation of the flows, provided that the linear independence of the columns of the channel matrix is preserved. Collectively, this means that space-time coding provides a geometric decomposition of the signal space into independent directions along which information is transmitted. As a result, coherent summation of the useful signal components occurs on the receiving side, while the noise components remain statistically independent. It is this property that determines the possibility of effective signal recovery even in the presence of random changes in the channel parameters. Thus, the established structure of the system formulas (1), (2) determines the fundamental geometry of signal transmission in a multi-antenna system. It forms the basis for further analysis of the impact of random factors of the propagation environment, noise and intentional interference on the stability of the radio communication system and on the accuracy of the recovery of transmitted information.

Signal energy structure and statistical model of noise and intentional interference in a multi-antenna system

The analysis of the energy structure of the signal was performed for a mathematical model of a multi-antenna transmission system, in which the signal realisations are considered in the functional space of orthonormal basis functions. The conditions for such a representation are determined by the relations formulas (3)-(5), which specify the decomposition of the transmitted signals in the coordinates of the signal space and impose restrictions on the energy parameters of the transmission. The use of an orthonormal basis allows representing each signal of a multi-antenna system as a vector of coordinates in the L-dimensional channel space. The coefficients of the orthonormal decomposition of the signal determine the energy contribution of the corresponding basis functions to the formation of the transmitted signal realisation. Thus, the signal energy is distributed between the coordinates of the signal space, and the structure of this distribution determines the geometry of the signal constellation in the multidimensional channel space.

Further analysis showed that the fluctuation noise in each antenna channel can also be represented in the same functional basis. According to the formulas (6)-(8), the noise components are described by random decomposition coefficients, which have a Gaussian distribution with zero mathematical expectation and given variances. This means that the noise effect manifests itself in the form of random fluctuations of the coordinates of the signal vector in the signal space. A similar structure was established for intentional interference. According to the formulas (9)-(12), interference signals can be represented by decomposition in the same orthonormal basis of functions. In this case, the difference between noise and interference is determined by the statistical characteristics of the decomposition coefficients, in particular the variances and spectral power densities.

The obtained result showed that the signal, fluctuation noise and intentional interference have a consistent coordinate structure in a single signal space of a multi-antenna system. In this interpretation, the information transmission process can be represented as a superposition of a deterministic signal component and random disturbances that cause random shifts of the signal vector relative to its ideal position in the signal space. A generalisation of the structure of the mathematical model of signal, noise, and interference in a multi-antenna system is given in Table 2.

Table 2. Structure of the energy model of signal, noise, and interference in a multi-antenna system

System component	Mathematical representation	Basic parameters	Physical interpretation
Useful signal	Orthonormal distribution of signals in the basis of functions formulas (3)-(5)	$xLmn$, EL	Distribution of signal energy between coordinates of the L-dimensional signal space
Fluctuating noise	Statistical model of noise distribution formulas (6)-(8)	$GL0$	Random fluctuations of the signal vector coordinates
Intentional interference	Noise signal model formulas (9)-(12)	$GL3$	Energy disturbances caused by external interference
Reception quality	Signal-to-noise ratio and signal-to-interference formulas (13)-(14)	($hL02$), ($PL/PL0$)	Integral characteristic of transmission channel stability

Source: compiled by the authors

The generalisation of the results presented in Table 2 shows that the useful signal $x_{Lm}(t)$, the fluctuation noise $n_L(t)$ and the intentional interference $j_L(t)$ have a consistent coordinate structure in the orthonormal signal space formed by the basis functions $\omega_{Ln}(t)$. In this space, each signal realisation is described by a set of orthonormal decomposition coefficients x_{Lmn}, which determine the signal projections onto the corresponding basis functions and characterise the energy contribution of each coordinate to the signal formation.

Similarly, the noise and interference components are given by the coefficients n_{Ln} and j_{Ln}, the statistical properties of which are given by the dispersions $G_{L0}/2$ and $G_{L3}/2$, respectively. Such a structure means that the action of the fluctuation noise and intentional interference manifested itself in the form of random perturbations of the signal vector coordinates in the multidimensional channel space. In this representation, the transmitted signal in the L-th channel was characterised by the energy parameter E_L, which was determined by the transmission energy limitation condition (6), while the noise and interference intensity were described by the spectral parameters G_{L0} and G_{L3}. Thus, the information transmission process in a multi-antenna system was interpreted as the energy interaction of the signal vector coordinates $\{x_{Lmn}\}$ with random perturbations $\{n_{Ln}\}$ and $\{j_{Ln}\}$ arising in the signal propagation medium. In the geometric interpretation, this corresponded to a random displacement of signal points in the L-dimensional signal space relative to the ideal positions.

The efficiency of information transmission in each channel of the multi-antenna system was determined by the energy balance between the useful signal power P_L and the noise powers P_{L0} and interference P_{L3}. This balance was formalised by integral indicators of reception quality – the signal/noise ratios $SNR_L = \frac{E_L}{G_{L0}} = \frac{P_L}{P_{L0}}$ and signal/interference $SIR_L = P_L/P_{L3} = P_L/G_{L3}$, determined by the formulas (14)-(15). The value SNR_L of and the corresponding interference parameters determined the level of noise immunity of each antenna channel and characterised the degree of remoteness of the signal vector from the area of false reception. Thus, the obtained result showed that the consistent representation of the signal, noise and intentional interference in the common orthonormal signal space allows describing the process of functioning of a multi-antenna system through the energy characteristics of the signal vector coordinates. It is these characteristics that determine the potential noise immunity of the system and create a mathematical basis for further analytical study of the probability of a bit error in the transmission channels.

Analysis of signal distortions and statistical evaluation of constellation degradation parameters

Analysis of the signal distortion structure was performed for the reception model, in which the observed signal was formed as a superposition of the useful component and noise-interference disturbances according to the relation (16). At the level of an individual channel symbol, this transition from the "pure" to the observed state was specified by the relation (17), where the disturbances included noise, interference and intentional interference within the corresponding antenna branch. It was this representation that created the initial analytical basis for the further description of the degradation of the signal constellation as a result of geometric transformations and stochastic perturbations of the signal vector coordinates. The initial conditions for such a description were given by the relations (18)-(20), which established the connection between the ideal channel symbol $C_{(\partial,l)}$ and the observed symbol $C_{(\partial,l)}$. In this representation, each transmitted symbol was characterised by a complex quantity.

$$C_{(\partial.l)} = \Re\{C_{(\partial.l)}\} + i\,\Im\{C_{(\partial.l)}\}, \tag{47}$$

where ∂ – symbol index in the signal block, l – antenna channel number. Using the formulae (18)-(20), the received signal was presented in the form of a vector model:

$$\hat{c}_{(\partial.l)} = \begin{bmatrix} \Re\{\hat{C}_{(\partial.l)}\} \\ \Im\{\hat{C}_{(\partial.l)}\} \end{bmatrix}, \tag{48}$$

which was associated with the ideal symbol vector:

$$c_{(\partial.l)} = \begin{bmatrix} \Re\{C_{(\partial.l)}\} \\ \Im\{C_{(\partial.l)}\} \end{bmatrix}. \tag{49}$$

This form of description allowed interpreting the signal passage through the channel as a transformation of the coordinates of the signal vector in a two-dimensional signal space. Further analysis showed that the deformations of the signal constellation could be interpreted as a composition of geometric transformations of the coordinates of the signal vector. According to the relation (19), the phase shift of the channel led to a rotation of the signal constellation by an angle φ, which changed the orientation of the coordinates (49) in the signal space. According to the relation (20), the amplitude mismatch between the quadrature channels was described by different gain coefficients for the I- and Q-components, which caused the scaling of the coordinates of the signal vector along the corresponding axes. An additional geometric transformation arose due to the quadrature error of the receiving path, which was described by the relation (22) and led to a mutual rotation of the quadrature components by an angle θ_{IQ}. Taking into account interference components and additive noise led to a generalised description of signal vector perturbations through the decomposition of interference into components according to (23). For a visual representation of the described signal vector transformations, it is advisable to use a graphical visualisation of the influence on the signal constellation configuration in the I-Q plane (Fig. 1).

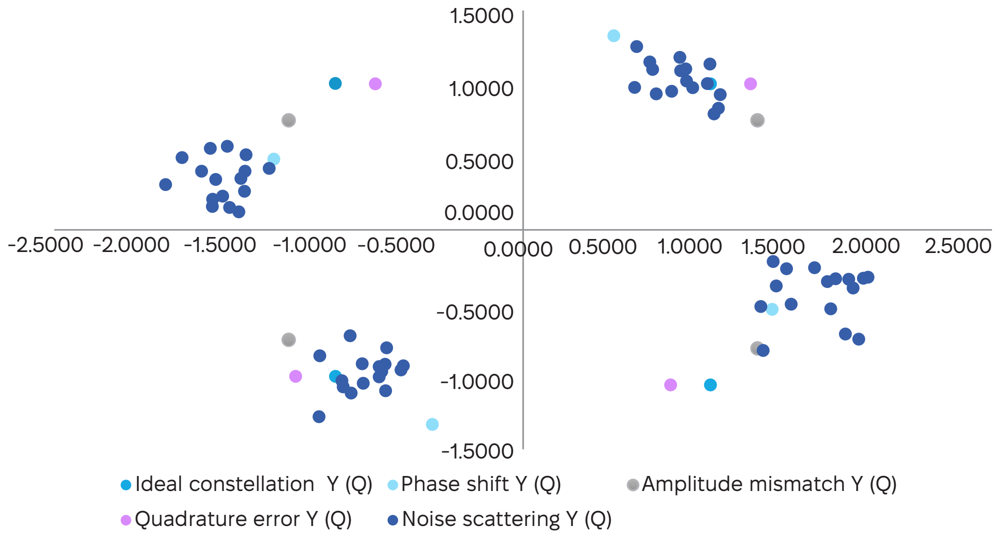

Figure 1. Geometric transformations of the signal constellation in the I-Q plane

Source: compiled by the authors

As shown in Figure 1, the phase shift, amplitude mismatch, and quadrature error change the spatial configuration of the signal constellation, while noise and interference perturbations additionally cause a random scattering of signal points relative to the ideal positions. This creates a basis for further statistical estimation of the degradation parameters from the characteristics of the received symbols. According to the relation (23), the interference-noise component in the symbol and channel was given by a vector.

$$n_{(\partial,l)} = \begin{bmatrix} \Re\{n_{(\partial,l)}\} \\ \Im\{n_{(\partial,l)}\} \end{bmatrix}, \quad (50)$$

which characterised the overlap of adjacent symbols (ISI) and additive oscillations (AWGN) and, in a parameterised description, could be characterised by the intensity A and the phase parameter ϕ (in the accepted definition of the model). An additional factor of signal constellation degradation was phase jitter, which was considered as a random process of rotation of signal points with a phase deviation $\theta_i \sim N(0, \sigma_i^2)$ according to (24), and its inclusion in the matrix contour of transformations was formalised by the relation (25). The generalisation of these transformations led to an integral representation of the observed symbol as a composition of geometric and stochastic changes in the coordinates of the signal vector, which was given by the relation (25), where the effective matrix $T_{(\partial,\, l)}$ accumulated static transformations (rotation, mismatched gain, quadrature error) and random rotation induced by phase jitter.

In this representation, the degradation of the signal constellation was determined by the gain parameters k_I and k_Q, the angular parameters φ, θ_{IQ}, the dispersion of phase fluctuations σ_i^2 and the interference intensity A. A further mathematical result was obtained by statistical analysis of the received symbols $\hat{C}_{(\partial,\, l)}$. Using the moment characteristics of the signal, in particular the mathematical expectation $E[\cdot]$, the dispersion $Var[\cdot]$ and the covariance $Cov[\cdot]$, the estimation of the degradation parameters of the signal constellation was performed. According to relations (26)-(27), the phase jitter was estimated through the covariance between the real and imaginary components of the received symbol:

$$Cov\left(\Re\{\hat{C}_{(\partial,l)}\}, \Im\{\hat{C}_{(\partial,l)}\}\right), \quad (51)$$

which allowed identifying σ_i^2 within the accepted parameterisation $\kappa\Phi(C_{(\partial,\, l)})$ in formula (27). The intensity of the interference component was determined through the statistical characteristics of the deviation of the signal vector coordinates from the average values, namely through the combination of the dispersion and the fourth-order central moment $m_4(\cdot)$ according to formula (28). Further analysis of the dispersions of the real and imaginary components of the received symbol provided an assessment of the contributions of noise and intentional interference according to (29), where the model functions $G_R(\cdot)$ and $G_I(\cdot)$ separated the dispersion contributions of phase fluctuations and interference in quadratures, and the residual term referred to the additive noise-interference component n_l. To generalise the obtained results, the structure of the signal constellation distortions and the corresponding parameters of the statistical assessment are given in Table 3.

Table 3. Structure of signal constellation distortions and parameters of the statistical evaluation

Distortion type	Model parameter	Mathematical description	Statistical evaluation method
Phase shift	φ	Signal constellation rotation (19)	Estimation through coordinate covariance
Amplitude mismatch	*kE*	Coordinate scaling (20-21)	Variance analysis of coordinates
Quadrature error	*θcomp*	Matrix rotation (22)	Evaluation by moment characteristics
Phase jitter	*σi2*	Random rotation of points (24-25)	Covariance of real and imaginary parts (27)
Interference	*A*	Breakdown of obstacles into components (23)	Fourth-order central moments (28)
Additive noise	$D[n_l]$	Noise component variance (29)	Variance estimates (29)

Source: compiled by the authors

As can be seen from Table 3, the signal constellation distortions in a multi-antenna system have a clearly structured nature and can be represented as a set of deterministic and stochastic transformations of the signal vector coordinates in the complex signal space. The deterministic distortion components are related to the channel and receiver path parameters and become manifested in the form of signal constellation rotation, coordinate scaling, and quadrature deformation, which are described by the parameters φ, *kE* and *θcomp*, respectively. The stochastic signal degradation components are formed by random processes in the transmission channel and include phase jitter, interference, and additive noise, the statistical characteristics of which are determined by the parameters σi^2, A and $D[nl]$. The generalisation of the obtained results shows that the signal constellation degradation can be formalised through a system of statistical estimates based on the momentary characteristics of the received symbols. The use of covariance and dispersion analysis of signal vector coordinates allows separating the contribution of different types of disturbances to the overall structure of signal distortions. This approach provides the ability to identify the parameters of phase fluctuations, interference components and noise components of the channel, which creates the basis for further analysis of the probability of bit errors and assessment of the noise immunity of a multi-antenna radio communication system.

Dynamic channel structure and the influence of non-stationarity of signal propagation

The dynamic structure of a multi-antenna communication channel is investigated taking into account the non-stationarity of propagation due to multipath and relative motion of the transmitter and receiver, and the time structure of the multipath signal is formalised by the discrete-path model (15). Under these conditions, the channel transmission coefficient h_{ij} is a random time-dependent quantity, and fluctuations in its amplitude and phase determine the statistical variability of the received signal. The initial conditions of the description are given by a class of fading models in which the amplitude statistics h_{ij} are consistent with the absence/presence of a dominant regular component: in the case of a predominance of scattered components, the Rayleigh mode is used, in the presence of a direct beam, the Rice mode, and for a generalised description of different degrees of "regularity-fluctuation" the Nakagami and Rice-Nakagami models are used.

The mathematical result of this step is the introduction of parameters that quantitatively record the contribution of the regular and random components to the average channel power: the ratio between $h_0^2(st)$ and $h_0^2(Rl)$, as well as the parameter ς, which specifies the ratio of the average powers, allow formalising the boundary transitions between the Rayleigh ($\varsigma \to 0$) and static ($\varsigma \to \infty$) regimes and thereby specifying a single fading classification scale within the framework of a consistent statistical model (transition formulas are given in the methodology). The next step of the analysis is aimed at the temporal variability of the channel. Within the Jakes model, the correlation structure of the transmission coefficient is determined by the autocorrelation function and the corresponding Doppler spectrum, and the key parameter is the maximum Doppler shift f_D, proportional to the relative velocity of the receiver; the compact form of the autocorrelation record is given by relation (41). Interpretatively, this means that the "update rate" of the channel is given by the geometry of the multi-beam field and the kinematics of the subscriber motion: with increasing v, f_D increases, the decorrelation $h_{ij}(t)$ in time accelerates, and the effect of interference of waves arriving by different paths with different Doppler shifts is enhanced. The generalisation of the spatio-temporal structure of the channel is carried out in the geometric elliptical scattering model (Fig. 2), where the transmitter and receiver are considered as foci of a system of ellipses, and the scatterers are considered as points evenly distributed within the outer and inner ellipses.

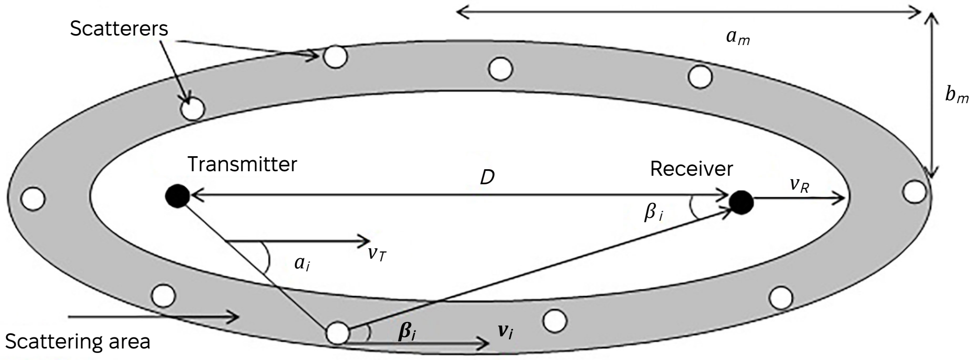

Figure 2. Taking into account the dynamic characteristics of the transmitter and receiver in the model in a multi-antenna system

Note: D – the length of the signal propagation path; β_i – the angle of reflection from the outer surface of the ellipse; a_i – the angle of reflection from the scatterer of the inner surface of the ellipse; v_T – the rate of change of the transmitter position; v_R – the rate of change of the receiver position; a_m – the semi-major axis of the outer ellipse; b_m – the semi-minor axis of the outer ellipse

Source: compiled by the authors

The model presented in Figure 2 is built on the basis of the elliptical approach to modelling a multibeam radio signal propagation channel. This approach is used to describe the operation of the channel in the uplink direction – from the mobile subscriber to the base station in microcell conditions, when the base station is located at a relatively low altitude and a line of sight (LoS) is possible between the transmitter and the receiver. Similar conditions are typical for urban wireless networks and tactical radio communication systems. Within the model, the transmitter, and receiver are considered as foci of a system of ellipses in which the signal scattering objects are located. It is assumed that the scatterers are evenly distributed within two ellipses: external and internal. The parameters of the external ellipse a_m and b_m are determined based on the maximum signal propagation delay according to the relation (42), while the internal ellipse is given by the geometric characteristics of the mobile subscriber's movement. The model assumes a minimum signal delay in the presence of direct visibility between the transmitter and receiver. An increase in the signal delay corresponds to the appearance of additional multipath components that arise as a result of reflection or diffraction of the signal on environmental objects. Thus, the elliptical geometric model allows linking the spatial structure of the signal propagation environment with the time characteristics of the communication channel.

Analytical assessment of interference immunity and bit error probability in a multi-antenna system

As a result of the analysis, the sequence of formation of indicators of reliability of information transmission in a multi-antenna system was determined: the signal/noise and signal/interference ratios, given by formulas (13), (14), determined the effective energy parameter of the channel h_0^2; this parameter was included in the bit-dependent estimates of the error probability $P_{(b,\ i)}$, obtained in formulas (31)-(35) and (36)-(40); further generalisation of single-channel estimates led to the system error indicator $P_B^{(L)}$, determined by averaging over antenna channels according to (47). It is shown that the quality of the L-th antenna channel was formalised through the energy parameters E_L, G_{L0} and G_{L3}, introduced in the energy-statistical description of the signal, fluctuation noise and intentional interference in the common orthonormal signal space formulas (3)-(12). In particular, E_L characterised the energy of the useful component in the L-th branch, while G_{L0} and G_{L3} specified the intensity of the noise and interference components through the spectral (dispersion) parameters in the same coordinates. Based on these quantities, integral metrics of reception quality were obtained by the formulas (13-14), which recorded the effective scale of signal degradation in each channel and subsequently directly determined the parameterisation of analytical error estimates.

The modulation structure was given by the signal constellation parameters $M = 2^B$, where B denoted the number of information bits per symbol, which allowed moving from the constellation geometry to the bit error probabilities. It was the dependence on B that was used in the bit-dependent estimates $P_{(b,\ i)}$ for the phase manipulation of the FM-M type in the relations formulas (36)-(39), where the expressions for the first bits of the symbol were given separately and the estimates for all bit positions were generalised. For the quadrature amplitude manipulation KAM-M and hierarchical quadrature amplitude manipulation, a similar transition from the constellation geometry to the bit error was implemented in the relations formulas (40)-(45), which allowed taking into account the configuration of the signal constellation and the differences between individual classes of erroneous transitions. For hierarchical quadrature amplitude manipulation, the parameter α was additionally taken into account, which changed the geometry of the constellation and affected the distribution of error probabilities between bit positions. As a result, it was found that varying this parameter provides differentiated reliability of bit streams by changing the decision-making boundaries in the signal space. After determining the single-channel estimates $P_{(B,\ l)}$, the analytical results were reduced to the integral characteristic of MIMO through averaging over antenna channels according to (46), which provided a transition from the quality of a separate branch to a generalised assessment of the reliability of data transmission in the system. To clearly display the sequence of transition from channel energy parameters and modulation structure to integral assessment of bit error, it is advisable to use the block diagram of the analytical BER model (Fig. 3).

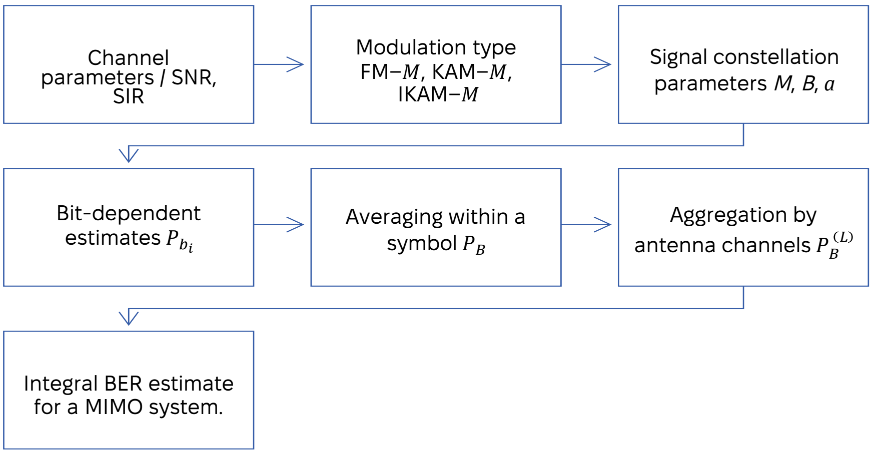

Figure 3. Analytical chain of BER formation in a multi-antenna communication system

Source: compiled by the authors

As shown in Figure 3, the formation of BER in a multi-antenna system is determined by the sequential interaction of the channel energy parameters, the characteristics of the interference environment, the structure of the signal constellation and the procedures for aggregating the error across the antenna branches. After determining the bit-dependent error estimates for individual positions in the signal block, the total error probability was aggregated within the symbol according to the formulas (43), (44). This allowed moving from partial estimates $P_{(b,\,i)}$ to a generalised indicator P_B, which took into account the configuration of the signal constellation, the hierarchy parameter α and the ratio of the regular and fluctuating components in the channel. Additionally, the bit weight coefficients given by the relation (45) parameterised the contribution of critical transitions between the constellation points and thereby specified the structure of the formation of the average bit error. The final step was the final aggregation of the error for the multichannel structure by averaging over the antenna branches according to (46). As a result, the single-channel estimates $P_{(B,\,l)}$ were reduced to the integral indicator $P_B^{(L)}$, which characterised the average bit error probability for the entire multi-antenna system, taking into account selective fading, Doppler non-stationarity, intersymbol interference, phase jitter and intentional interference.

It was established that the channel energy balance, determined by the relations (formulas (13), (14)), set the effective margin of separation of the signal constellation points relative to noise fluctuations. Within the analytical model, this margin was included in the expressions for the bit error probability through the parameter h_0^2 and the channel characteristics associated with it. As a result, a direct causal relationship was established between the channel energy parameters and the geometry of the signal space, which determined the analytical estimates $P_{(bi)}$ for individual bit positions. For phase manipulation in the coherent reception mode, an exact analytical expression of the error probability for the first two bits (31) was obtained, while for the remaining bits $i = \overline{3, B}$ a generalised analytical notation (32) was used, in which the auxiliary functions formulas (formulas (33), (34)) reflected the geometry of the decision-making areas in the signal constellation. The average bit error within one symbol was determined by averaging over all bit positions according to (35), which allowed moving from local estimates of $P_{(bi)}$ to an integral characteristic of the transmission quality for a given value of M. For quadrature amplitude manipulation and hierarchical quadrature amplitude manipulation, a generalised expression for the error of the first two bits (36) was obtained.

Further analysis led to an accurate analytical record of the average error over all bit positions formulas (37)-(39). Weighting coefficients (40) determined the contribution of different classes of transitions between points of the signal constellation and thereby formalised the influence of the geometry of the decision boundaries on the structure of bit errors. It was found that, even with the same energy parameters of the channel M and h_0^2, the error probability depended on the bit number i. This dependence is explained by the geometric structure of the signal constellation, since different bit positions correspond to different partitions of the set of signal points into the decision-making areas. As a result, the minimum distances to the decision boundaries turned out to be different, which caused an uneven distribution of errors between bits. It is shown that the parameter α, which is used in hierarchical quadrature amplitude manipulation, directly affects the minimum Euclidean distances between subsets of signal constellation points. For the value $\alpha = 1$, the constellation structure corresponds to symmetric quadrature amplitude manipulation, in which all bits have close discrimination conditions. With increasing α, part of the decision boundaries is removed, which leads to a decrease in the probability of error for priority bits and, accordingly, to the redistribution of errors between bit streams. After determining the values of $P_{(B,\,l)}$ for each antenna channel, a system error indicator of the multi-antenna structure was obtained. The generalisation was performed by averaging over all antenna channels according to the relation (46), which allowed moving from a single-channel assessment to an integral characteristic of the reliability of the entire MIMO system.

The results obtained formed a consistent analytical scheme for assessing the noise immunity of multi-antenna radio communication systems. The energy metrics of reception quality determined the scale of signal degradation in the channel, the geometry of the signal constellation formed a bit-dependent error distribution for different modulation schemes, and the aggregation of the results over antenna channels allowed obtaining an integral error indicator of the system. Taken together, this provided a formalised transition from the parameters of the noise-interference environment and fading modes to a quantitative assessment of the bit error probability for both a separate channel and the entire multi-antenna radio communication system.

DISCUSSION

The obtained analytical results allow interpreting the mechanism of bit error formation in multi-antenna radio systems as a consequence of the interaction of channel energy parameters, signal constellation structure, and statistical characteristics of noise and interference disturbances. In this representation, the channel energy balance determines the scale of fluctuations in the coordinates of signal points, while the constellation geometry sets the configuration of decision-making regions in the signal space, through which these fluctuations are transformed into bit errors. This interpretation is consistent with the approach of Y. Ma *et al*. (2018), who proposed a geometrically conditioned non-stationary MIMO model for vehicular communications and showed that temporal changes in channel parameters have a physically interpreted relationship with the motion of the transmitter and receiver. The results of the study are also consistent with the conclusions of G.N. Kamga *et al*. (2017), which show that the characteristics of multi-antenna systems significantly depend on the comprehensive consideration of channel effects, rather than on the isolated analysis of individual factors. A similar result is also found in the work of M. Yang *et al*. (2017), where it is shown that the correlation characteristics of the channel can significantly change the spatial separation of signals and affect the reception error. This is consistent with the conclusions that the preservation of linear independence of spatial modes, the energy balance of antenna branches and the statistical structure of distortions directly determine the possibility of correct recovery of transmitted symbols. A similar logic of spatial analysis of communication channels was presented in the study of L. Ribeiro *et al*. (2022), where the concept of channel charting was used to display the geometric structure of the channel space in massive MIMO systems. In the current study, this principle was manifested in the representation of the degradation of the signal constellation as a geometric transformation of the coordinates of the signal vector, which allowed linking the statistics of noise and interference with the geometry of decision-making.

In the review study of M. Ahmed *et al*. (2023), the authors showed that the use of STAR-RIS allows actively changing the structure of the multipath environment and thereby influencing the energy characteristics of the channel. Such an interpretation of the propagation environment as a geometric configuration of scatterers is consistent with the results of the analysis of the dynamic structure of the channel, where temporal fluctuations in the transmission coefficient were explained by changes in the multipath propagation trajectories and Doppler effects that arose during the movement of subscribers. Further development of this idea was demonstrated in the work of J. Xiao *et al.* (2024), where multitask learning was used to estimate the channel parameters in the near and far zones for networks with reconfigurable surfaces.

From a methodological point of view, the obtained results are also consistent with modern approaches to channel modelling in new generation systems. In the work of M.P. Kumar *et al*. (2025), it was shown that the accuracy of wireless channel modelling significantly depends on taking into account the real parameters of the propagation environment and measurement data obtained in field experiments. A similar logic is also observed in the current analysis, where the structure of channel non-stationarity is explained through the geometric scattering model and the correlation-Doppler properties of the signal. In the study of Y. Singh (2026), the possibilities of using the National Instruments – Universal Software Radio Peripheral (NI-USRP) platform for real-time monitoring and analysis of wireless signals were demonstrated, which confirmed the relevance of experimental verification of channel models. In this context, the results obtained on the statistical evaluation of the constellation degradation parameters can be used as a tool for interpreting the measured signal characteristics, since the instantaneous characteristics of the received symbols are directly related to the statistics of channel disturbances.

Machine learning methods used for channel parameter estimation and signal detection have also made a significant contribution to modern wireless systems analysis, for example, A. Singh & S. Saha (2022) showed that deep learning algorithms can effectively compensate for the effects of various types of channel distortions in Orthogonal Frequency Division Multiplexing (OFDM) systems. A similar trend was continued in the study of A.S. Alqahtani *et al.* (2024), where generative models with self-attention mechanisms were used to improve channel estimation in MIMO-OFDM systems. In the presented study, a similar result was obtained analytically by introducing constellation degradation parameters that described the effects of noise, interference, and phase fluctuations. Further development of intelligent signal processing methods in massive multi-antenna systems was demonstrated in the work of A. Kumar & A. Nanthaamornphong (2025), where deep neural networks were applied to the problem of detecting signals in Multiple Input Multiple Output – Orthogonal Time Frequency Space (MIMO-OTFS). In turn, R. Shankar (2023) used a bidirectional Long Short-Term Memory (LSTM) architecture for channel estimation in 5G massive MIMO-OFDM systems. The results obtained are consistent with this trend, since the analysis of the dynamic structure of the channel showed that the non-stationarity of signal propagation is directly related to the correlation properties of the channel and Doppler broadening of the spectrum. In the work of M.M.E. Kotb *et al*. (2025), a comparative analysis of algorithms for estimating the carrier frequency shift in OFDM and MIMO-OFDM systems was carried out. The results obtained in the current study showed that even minor phase and frequency deviations can significantly affect the accuracy of signal recovery.

In the broader context of the evolution of wireless networks, the presented results correspond to the general trend of development of multi-antenna technologies. In the work of M. Pande *et al.* (2025), it was shown that MIMO systems have become a key element of the architecture of mobile networks of the third, fourth and fifth generations, since spatial diversity allows simultaneously increasing the throughput and reliability of data transmission. In the current study, this property was manifested in the formation of a systematic error estimate through the aggregation of bit errors over antenna channels, which allowed interpreting the MIMO system as a set of parallel error modes with different statistical characteristics. Further comparison of the results with modern studies showed that increasing the reliability of information transmission in multi-antenna systems is increasingly associated with a combination of analytical channel models and intelligent signal processing algorithms. In the work of M. Islam *et al*. (2025), the authors demonstrated the use of deep neural networks to optimise the parameters of the receive-transmit path in 5G MIMO systems. In the analysis conducted, a similar problem was solved analytically through the formalisation of the signal constellation degradation parameters and the statistical evaluation based on the moment characteristics of the received symbols. A similar approach was observed in the work of L.S.S.P.K. Chodisetti *et al*. (2023), where a soft detection algorithm based on coordinate descent was proposed for massive MU-MIMO-OFDM systems.

Another direction of modern research is related to the compensation of nonlinear distortions and optimisation of signal transmission parameters. In the work of G.K. Reddy & G.M. Sheeba (2024), the use of hybrid equalisers Minimum Mean Square Error – Maximum Likelihood Sequence Estimation (MMSE-MLSE) to reduce the peak signal values in MIMO-OFDM systems was considered. The results were consistent with the results of the analysis of signal constellation distortions, where phase perturbations, quadrature errors and interference components led to deformation of the coordinates of signal points and, accordingly, to a change in the structure of decision-making areas. New principles of multiple access also play a significant role in the development of modern communication systems. The work of H. Iklodiya & M.S. Bhanwar (2025) considered the application of Non-Orthogonal Multiple Access (NOMA) technology in combination with OFDM and machine learning methods to improve the efficiency of spectrum use. In this context, the results of the analysis of bit errors acquire special importance, since the uneven distribution of errors between bit positions in the signal constellation can be used for differentiated protection of information flows of different priorities.

A separate area of research concerns the optimisation of data transmission in satellite and hybrid networks. In the work of K. Balamurugan & N. Janakiraman (2025), a cascade coding scheme was proposed for the optimisation of satellite channels of the Digital Video Broadcasting – Return Channel via Satellite, 2nd generation (DVB-RCS2) standard in MIMO-OFDM systems. The authors showed that the combination of coding methods and spatial diversity allows reducing the probability of data transmission errors in channels with a high level of noise. A similar logic is also observed in the obtained results, where the system error estimate was formed by aggregating bit errors over antenna channels, which allowed interpreting the MIMO system as a set of parallel channels with different statistical characteristics.

An important contribution was made by the study of L. Ge *et al*. (2022), where a classification-weighted neural network model was proposed to compensate for channel distortions in massive MIMO-OFDM systems. The results obtained showed that the use of deep models allows for effective signal structure reconstruction even under difficult channel conditions. In the study by H. Harkat *et al.* (2022), it was shown that MIMO-OFDM technology has become a key element of modern communication networks due to its ability to simultaneously increase bandwidth and reliability of signal transmission. This conclusion is consistent with the results of the study, in which the multi-antenna structure is also considered as a systemic basis for increasing interference immunity and transmission stability. A similar conclusion was supported in the work of N. Ye *et al*. (2021), which analysed modern approaches to the use of deep learning in NOMA systems. The study also focuses on an analytical description of signal degradation mechanisms, in particular, the influence of intentional interference, phase distortion, intersymbol interference, and Doppler non-stationarity on the probability of a bit error. The final link in the comparison was formed by the results of the study by M.A. Abdallah *et al.* (2023), devoted to increasing the accuracy of data transmission in MU-MIMO-OFDM systems through the use of efficient coding schemes. This conclusion is consistent with the obtained analytical results, where the bit error probability was considered as an integral characteristic formed under the influence of the energy parameters of the channel, the structure of the signal constellation and the statistical characteristics of noise and interference.

Taken together, the comparison showed that the results of the study are consistent with the main directions of development of modern wireless technologies, where the spatial properties of the channel, the statistical structure of the signal and adaptive processing algorithms play a central role. At the same time, the obtained analytical dependencies allowed forming a consistent scheme for assessing the reliability of information transmission in multi-antenna systems, in which the energy characteristics of the channel, the geometry of the signal constellation and the statistical parameters of interference are integrated into a single model for analysing data transmission errors.

CONCLUSIONS

The study analysed the features of the functioning of multi-antenna radio systems built on software-defined means in conditions of fluctuating noise, intentional interference and channel non-stationarity. The analysis showed that for a correct description of the information transmission process in MIMO systems, a coordinated representation of the useful signal, noise, and interference in a common signal space is necessary. This approach allowed considering the degradation of the received signal not as a set of isolated effects, but as a single process in which the spatio-temporal structure of the transmission, the energy characteristics of the channel and the statistics of disturbances form a general picture of the error. As a result of the study, it was established that with quasi-stationarity of the channel at the block transmission interval and with orthogonal spatio-temporal organisation of signals, the possibility of correct recovery of the transmitted spatial symbols is ensured. This means that the multi-antenna structure can maintain resistance to random channel changes, provided that the channel operator agrees with the spatio-temporal transmission scheme. It is shown that the decoding efficiency in these conditions is determined not only by the very fact of the presence of several antenna branches, but also by the preservation of linear independence of spatial modes, which ensures the separation of information flows on the receiving side. It was also established that the distortions of the signal constellation are complex in nature and are formed under the influence of both deterministic geometric transformations and random perturbations. This made it possible to present the signal degradation as a result of the combined action of phase, amplitude, interference, and noise factors and proceed to the statistically interpreted evaluation by the characteristics of the received symbols.

The results obtained confirmed that the reception error is determined by the combined action of the channel energy balance, the structure of the signal constellation and the intensity of the interference environment, and not by a separate factor in itself. A separate block of results concerned the influence of channel non-stationarity on the stability of information transmission. It is shown that the temporal changes in the transmission coefficients are associated with the correlation properties of the channel and Doppler variability, which complicates the process of signal recovery with increasing mobility of the transmitter and receiver. This made it possible to link the channel dynamics with the conditions for the formation of fading and take this effect into account in the general analytical scheme for assessing the reliability of transmission. As a result, the bit error was interpreted as an integral indicator that reflects the coordinated action of the channel parameters, the type of modulation and the multichannel structure of the system.

The practical significance of the results obtained is that the proposed approach can be used to analyse and optimise multi-antenna radio systems on software-defined devices in conditions of noise, interference and a non-stationary channel. Its application creates a basis for substantiating the parameters of modulation, coding, and signal processing in order to increase the reliability and immunity to interference of radio communications. Prospects for further research are related to applied verification of the model using experimental data and its adaptation to more complex scenarios of spatial correlation and multipath propagation.

ACKNOWLEDGEMENTS

None.

FUNDING

None.

CONFLICT OF INTEREST

None.

REFERENCES

[1] Abdallah, M.A., Nassr, M., Anbar, M., & Alasadi, H.A.A. (2023). BER improvement in 5G MU MIMO-OFDM systems using channel coding techniques. *Pure and Applied Optics,* 56(1), article number 51121. doi: 10.7149/OPA.56.1.51121.

[2] Ahmed, M., Wahid, A., Laique, S.S., Khan, W.U., Ihsan, A., Xu, F., Chatzinotas, S., & Han, Z. (2023). A survey on STAR-RIS: Use cases, recent advances, and future research challenges. *IEEE Internet of Things Journal,* 10(16), 14689-14711. doi: 10.1109/JIOT.2023.3279357.

[3] Alqahtani, A.S., Pandiaraj, S., Alshmrany, S., Almalki, A.J., Prabhu, S., & Kumar, U.A. (2024). Enhancing MIMO-OFDM channel estimation in 5G and beyond with conditional self-attention generative adversarial networks. *Wireless Networks,* 30(3), 1719-1736. doi: 10.1007/s11276-023-03615-y.

[4] Amadid, J., Belhabib, A., Khabba, A., Zeroual, A., & Hassani, M.M. (2022). On channel estimation and spectral efficiency for cell-free massive MIMO with multi-antenna access points considering spatially correlated channels. *Transactions on Emerging Telecommunications Technologies,* 33(5), article number e4438. doi: 10.1002/ett.4438.

[5] Balamurugan, K., & Janakiraman, N. (2025). DVB-RCS2 satellite link optimization for efficient data transmission using cascaded coding approach in MIMO-OFDM system. *Wireless Personal Communications,* 144(3), 435-462. doi: 10.1007/s11277-025-11856-7.

[6] Chodisetti, L.S.S.P.K., Donga, M., Tella, P.V., Rao, K.P., Chandra, K.R., Budumuru, P.R., & Rao, C.V. (2023). Equalization based soft output data detection for massive MU-MIMO-OFDM using coordinate descent. In P. Pareek, N. Gupta & M.J.C.S. Reis (Eds.), *4th EAI international conference: Cognitive computing and cyber physical systems* (pp. 173-184). Cham: Springer. doi: 10.1007/978-3-031-48891-7_14.

[7] de la Fuente, A., Interdonato, G., & Araniti, G. (2022). User subgrouping and power control for multicast massive MIMO over spatially correlated channels. *IEEE Transactions on Broadcasting,* 68(4), 834-847. doi: 10.1109/TBC.2022.3190990.

[8] Du, P., Zhang, C., Jing, Y., Fang, C., Zhang, Z., & Huang, Y. (2026). Jamming detection and channel estimation for spatially correlated beamspace massive MIMO. *IEEE Transactions on Wireless Communications,* 25, 3910-327. doi: 10.1109/TWC.2025.3607091.

[9] Ge, L., Qi, C., Guo, Y., Qian, L., Tong, J., & Wei, P. (2022). Classification weighted deep neural network based channel equalization for massive MIMO-OFDM systems. *Radioengineering,* 31(3), 346-356. doi: 10.13164/re.2022.0346.

[10] Harkat, H., Monteiro, P., Gameiro, A., Guiomar, F., & Ahmed, H.F.T. (2022). A survey on MIMO-OFDM systems: Review of recent trends. *Signals,* 3(2), 359-395. doi: 10.3390/signals3020023.

[11] Iklodiya, H., & Bhanwar, M.S. (2025). Noma based communication in 5G scheme on nonlinear real signal SVM OFDM system. *International Journal of Research & Technology,* 13(3), 365-377.

[12] Islam, M., Islam, A., & Ahmed, F. (2025). A DNN-based 5G MIMO system adopting a mix of tactics. *Discover Electronics,* 2(1), article number 15. doi: 10.1007/s44291-025-00055-0.

[13] Kamga, G.N., Xia, M., & Aïssa, S. (2017). Spectral-efficiency analysis of regular- and large-scale (Massive) MIMO with a comprehensive channel model. *IEEE Transactions on Vehicular Technology,* 66(6), 4984-4996. doi: 10.1109/TVT.2016.2620489.

[14] Khudov, H., Diakonov, O., Kuchuk, N., Maliuha, V., Furmanov, K., Mylashenko, I., Olshevskyi, Y., Stetsiv, S., Solomonenko, Y., & Yuzova, I. (2021). Method for determining coordinates of airborne objects by radars with additional use of ADS-B receivers. *Eastern-European Journal of Enterprise Technologies,* 4(9(112)), 54-64. doi: 10.15587/1729-4061.2021.238407.

[15] Khudov, H., Kostianets, O., Kovalenko, O., Maslenko, O., & Solomonenko, Y. (2023). Using Software-Defined radio receivers for determining the coordinates of low-visible aerial objects. *Eastern-European Journal of Enterprise Technologies,* 4(9(124)), 61-73. doi: 10.15587/1729-4061.2023.286466.

[16] Kotb, M.M.E., Mohamed, M.R.A.H., Fahmy, A.Y.H.A., & Mohra, A.S.S.S. (2025). Fine carrier frequency offset estimation for OFDM and MIMO-OFDM systems: A comparative study. *Scientific Reports,* 15, article number 15622. doi: 10.1038/s41598-025-98233-3.

[17] Kumar, A., & Nanthaamornphong, A. (2025). Signal detection of massive MIMO-OTFS using DNN algorithm with diverse channel state estimation. *Physics Open*, 25, article number 100332. doi: 10.1016/j.physo.2025.100332.

[18] Kumar, M.P., Summaq, A., Chinnadurai, S., Kumaravelu, V.B., Selvaprabhu, P., Imoize, A.L., & Jaiswal, G. (2025). An overview of channel modeling and propagation measurements in IRS-based wireless communication systems. In A.L. Imoize, V.B. Kumaravelu & D.-T. Do (Eds.), *Reconfigurable intelligent surfaces for 6G and beyond wireless networks* (pp. 435-473). Hoboken: John Wiley &Sons. doi: 10.1002/9781394250141.ch13.

[19] Ma, Y., Yang, L., & Zheng, X. (2018). A geometry-based non-stationary MIMO channel model for vehicular communications. *China Communications,* 15(7), 30-38. doi: 10.1109/CC.2018.8424580.

[20] Pande, M., Kulkarni, A.J., & Shastri, A.S. (2025). Multiple input multiple output schemes in 3G, 4G, and 5G networks. In *Optimization methods in mobile communication systems: A machine-generated literature overview* (pp. 129-220). Singapore: Springer. doi: 10.1007/978-981-95-1810-4_3.

[21] Papazafeiropoulos, A., Tran, L.-N., Abdullah, Z., Kourtessis, P., & Chatzinotas, S. (2024). Achievable rate of a STAR-RIS assisted massive MIMO system under spatially-correlated channels. *IEEE Transactions on Wireless Communications,* 23(2), 1550-1564. doi: 10.1109/TWC.2023.3290325.

[22] Reddy, G.K., & Sheeba, G.M. (2024). Enhancing PAPR performance in MIMO-OFDM system using hybrid optimal MMSE-MLSE equalizers. *Multimedia Tools and Applications,* 83(10), 28993-29013. doi: 10.1007/s11042-023-16489-1.

[23] Riabukha, V.P., Semeniaka, A.V., Katiushyn, Ye.A., & Atamanskiy, D.V. (2022). Comparative experimental investigations of adaptive and non-adaptive MTI systems in pulse radars of various applications and wave ranges. *Radioelectronics and Communications Systems,* 65, 165-176. doi: 10.3103/S073527272204001X.

[24] Ribeiro, L., Leinonen, M., Al-Tous, H., Tirkkonen, O., & Juntti, M. (2022). Channel charting aided pilot reuse for massive MIMO systems with spatially correlated channels. *IEEE Open Journal of the Communications Society,* 3, 2390-2406. doi: 10.1109/OJCOMS.2022.3225054.

[25] Shankar, R. (2023). Bi-directional LSTM based channel estimation in 5G massive MIMO OFDM systems over TDL-C model with Rayleigh fading distribution. *International Journal of Communication Systems,* 36(16), article number e5585. doi: 10.1002/dac.5585.

[26] Shi, E., Zhang, J., He, R., Jiao, H., Wang, Z., Ai, B., & Ng, D.W.K. (2022). Spatially correlated reconfigurable intelligent surfaces-aided cell-free massive MIMO systems. *IEEE Transactions on Vehicular Technology,* 71(8), 9073-9077. doi: 10.1109/TVT.2022.3175459.

[27] Singh, A., & Saha, S. (2022). Machine/deep learning based estimation and detection in OFDM communication systems with various channel imperfections. *Wireless Networks,* 28(6), 2637-2650. doi: 10.1007/s11276-022-02994-y.

[28] Singh, Y. (2026). NI-USRP and ANN-based wireless real-time monitoring of liquid level using non-contact capacitive level sensor. *IETE Technical Review,* 43(1), 58-69. doi: 10.1080/02564602.2025.2589806.

[29] Sui, Z., Ngo, H.Q., Van Chien, T., Matthaiou, M., & Hanzo, L. (2025). RIS-assisted cell-free massive MIMO relying on reflection pattern modulation. *IEEE Transactions on Communications,* 73(2), 968-982. doi: 10.1109/TCOMM.2024.3446589.

[30] Xiao, J., Wang, J., Wang, Z., Wang, J., Xie, W., & Liu, Y. (2024). Multi-task learning for near/far field channel estimation in STAR-RIS networks. *IEEE Transactions on Communications,* 72(10), 6344-6359. doi: 10.1109/TCOMM.2024.3402619.

[31] Yang, M., Zhang, S., Shao, S., Guo, C., & Tang, W. (2017). Statistical modeling of the high altitude platform dual-polarized MIMO propagation channel. *China Communications,* 14(3), 43-54. doi: 10.1109/CC.2017.7897321.

[32] Ye, N., An, J., & Yu, J. (2021). Deep-learning-enhanced NOMA transceiver design for massive MTC: Challenges, state of the art, and future directions. *IEEE Wireless Communications*, 28(4), 66-73. doi: 10.1109/MWC.001.2000472.

[33] Zhao, L., Wang, H., Chen, J., & Meng, X. (2024). Multi-array visible-light optical generalized spatial multiplexing – multiple input multiple-output system with pearson coefficient-based antenna selection. *Photonics,* 11(1), article number 67. doi: 10.3390/photonics11010067.

Григорій Радзівілов
Кандидат технічних наук, доцент
Військовий інститут телекомунікацій та інформаційних технологій імені Героїв Крут
01011, вул. Князів Острозьких, 45/1, м. Київ, Україна
https://orcid.org/0000-0002-6047-1897

Дмитро Павлюк
Ад'юнкт
Військовий інститут телекомунікацій та інформаційних технологій імені Героїв Крут
01011, вул. Князів Острозьких, 45/1, м. Київ, Україна
https://orcid.org/0000-0001-8461-3899

Математична модель функціонування рухомої системи радіозв'язку побудованої на програмно керованих засобах

Анотація. Метою дослідження було розроблення узагальненої математичної моделі функціонування багатоантенних систем радіозв'язку в умовах дії випадкових та навмисних завад і аналітичне описання впливу завадово-шумових та нестаціонарних чинників на захищеність і надійність передавання інформації. У роботі застосовано матричну модель каналу, просторово-часове блокове кодування, ортонормальне подання сигналів у спільному сигнальному просторі та статистичне моделювання шуму і завад у координатах базису. Результати дослідження показали, що за квазістаціонарності каналу на інтервалі блокової передачі та ортогональності просторово-часової структури формується оборотний канальний оператор. За таких умов забезпечується лінійне відновлення переданого вектора символів і когерентне підсумовування корисної складової при статистичній незалежності шумових компонент на виході декодера. Корисний сигнал, флуктуаційний шум і навмисні завади мають узгоджену координатну структуру в одному ортонормальному сигнальному просторі. Унаслідок цього якість кожного антенного каналу визначається енергетичним балансом між корисною енергією та спектральними параметрами шуму і завад, що задає віддаленість сигнальних точок від областей помилкового рішення. Деградація констеляції описується композицією геометричних перетворень (обертання, масштабування, квадратурна деформація) і стохастичних збурень (фазове тремтіння, інтерференція, адитивний шум), а параметри цих спотворень ідентифікуються за математичним сподіванням, дисперсією та коваріацією координат прийнятих символів. Часова нестаціонарність каналу визначається доплерівським зсувом і кореляційною структурою коефіцієнта передачі, а еліптична геометрична модель розсіювання пов'язує затримки багатопроменевих компонентів із просторовою конфігурацією розсіювачів. Практична значущість результатів полягає у можливості використання запропонованої моделі для аналізу й оптимізації багатоантенних радіосистем на програмно керованих засобах в умовах шумів, завад і нестаціонарного каналу. Її застосування сприяє обґрунтуванню параметрів модуляції та кодування, а також підвищенню надійності й завадозахищеності радіозв'язку

Ключові слова: просторово-часове кодування; адитивний шум; навмисне втручання; MIMO; програмно визначене радіо; ефект Доплера

Machinery & Energetics
Vol. 17, No. 1. 2026

Journal homepage:
https://technicalscience.com.ua/en

UDC 697.94:620.9
DOI: 10.31548/machinery/1.2026.73

ISSN 2663-1334
e-ISSN 2663-1342

Furqan Haider Mohammed Ali
MSc
Technical Engineering College Kirkuk
Northern Technical University
36001, Kirkuk, Iraq
https://orcid.org/0009-0004-5491-3224

Zahraa Haider Mohammed Ali
MSc
Kirkuk Polytechnic College
Northern Technical University
36001, Kirkuk, Iraq
https://orcid.org/0009-0007-7034-5230

Mustafa Naozad Taifor
MSc
Renewable Energy Research Centre
Northern Technical University
36001, Kirkuk, Iraq
https://orcid.org/0000-0001-7146-1160

Hussein Hayder Mohammed Ali*
PhD
Technical Engineering College Kirkuk
Northern Technical University
36001, Kirkuk, Iraq
https://orcid.org/0000-0003-4264-400X

Experimental study of some parameters to enhance efficiency of evaporative cooler: Technical notes

Abstract. As an alternative to conventional vapour-compression air conditioning systems, which significantly increase peak electrical demand and energy consumption, this study investigates methods to enhance the performance and energy efficiency of evaporative cooling systems. A hybrid dual cooling configuration integrating a vapour-compression refrigeration unit with an evaporative cooler was experimentally developed and evaluated. The study focused on key modifications, including the replacement of conventional wood dust pads with padding cartoon material, the use of an auxiliary submersible pump to increase water circulation, and the combined operation of both pad materials. The experimental results demonstrated a substantial improvement in system performance due to these modifications. In particular, the hybrid system operating with a combined wood dust and padding cartoon medium achieved the highest cooling efficiency of 89%, indicating a significant enhancement in heat and mass transfer processes. The integration of increased water flow further contributed to improved wettability of the pads and more effective evaporative cooling. In terms of energy performance, the hybrid system exhibited an energy efficiency ratio (EER) of 8.3, which is markedly higher than that of the standalone vapour-compression system (EER = 1.95). Additionally, the independent evaporative cooling system achieved a maximum EER of 14.8 with a cooling efficiency of 71%, confirming its superior energy-saving potential

Article's History: Received: 07.11.2025; Revised: 02.02.2026; Accepted: 26.02.2026; Published: 30.03.2026.

Suggested Citation:
Ali, F.H.M., Ali, Z.H.M., Taifor, M.N., & Ali, H.H.M. (2026). Experimental study of some parameters to enhance efficiency of evaporative cooler: Technical notes. *Machinery & Energetics,* 17(1), 73-81. doi: 10.31548/machinery/1.2026.73.

*Corresponding author

under suitable operating conditions. The results also revealed that optimising pad material characteristics and water distribution plays a critical role in enhancing cooling efficiency while minimising energy input. These findings confirmed that the integration of evaporative cooling with conventional systems, along with appropriate material selection and hydraulic enhancement, can significantly reduce overall energy consumption while maintaining satisfactory thermal comfort levels. From a practical perspective, the proposed hybrid cooling system is a cost-effective, energy-efficient, and sustainable solution for hot, dry climates, utilising low-cost local materials and simple modifications to reduce energy demand and emissions while improving and guiding future cooling technologies

Keywords: hybrid air conditioning; thermodynamic analysis; wood dust; cardboard padding; energy efficiency

INTRODUCTION

The growing global demand for cooling, driven by rising ambient temperatures and urbanisation, has led to a significant increase in energy consumption associated with conventional air-conditioning systems. Vapour-compression refrigeration, while widely used, imposes substantial electrical loads and contributes to greenhouse gas emissions, making it increasingly unsustainable in the context of current energy and environmental challenges. In 2026, the need for alternative cooling strategies was particularly urgent in hot and dry regions, where efficient and low-energy solutions can directly alleviate pressure on power infrastructure. From a theoretical perspective, improving evaporative cooling performance through enhanced heat and mass transfer mechanisms offers a promising pathway to increase system efficiency. Practically, hybridising evaporative and vapour-compression systems provides an opportunity to balance thermal comfort with reduced energy use. Therefore, investigating optimised materials and system configurations for hybrid cooling systems is essential for advancing sustainable and cost-effective air-conditioning technologies.

A comparison of recent studies highlights both methodological and technological advancements in evaporative cooling systems. M.J. Romero-Lara *et al*. (2023) focused on developing a simplified method for calculating the seasonal energy efficiency ratio (SEER) of regenerative indirect evaporative coolers, demonstrating reliable prediction accuracy with minimal deviation from detailed simulation models. In contrast, the review by R.A. Hasan *et al*. (2025) provided a broader perspective, emphasising recent innovations such as desiccant-assisted and hybrid cooling systems, and identifying key challenges like humidity sensitivity and maintenance requirements. Meanwhile, S. Rasheed *et al*. (2025a) presented a detailed experimental and numerical investigation into material selection and airflow configurations, showing that high-wettability materials and optimised flow patterns significantly enhance cooling performance and thermal effectiveness. A.H. Salman *et al*. (2024) investigated the performance of a multistage evaporative cooling system designed to enhance cooling efficiency under extreme climatic conditions such as those in Iraq. The study highlighted that conventional evaporative media typically achieve efficiencies between 80% and 90%, though performance can vary widely depending on system design. To address these limitations, a multistage configuration incorporating successive water-air heat exchanger stages was developed to pre-cool the incoming air before direct evaporative cooling. The results indicated that this approach significantly improves thermal performance, reducing outlet dry-bulb temperature by approximately 50% and lowering specific humidity by about 80%. Furthermore, the system demonstrated clear advantages over conventional vapour-compression systems, including reduced energy consumption, lower environmental impact, and cost-effectiveness. A.F. Santos *et al*. (2021) improved the evaluation of evaporative cooler energy efficiency. They developed a COP index for this type of system using parameters that were easier to simulate. Their results showed COP values of 45.58 and 25.77 for two different simulated evaporative cooling units, compared with 6.29 for a conventional vapour-compression refrigeration system.

The purpose of this study was to experimentally enhance the performance and energy efficiency of an evaporative cooling system through structural modifications and hybrid integration with a vapour-compression refrigeration unit. To achieve this, the study investigated the effect of increasing water circulation by incorporating an additional submersible pump on overall cooling performance. It also evaluated the influence of different cooling pad materials, including wood dust, cardboard padding, and their combination, on heat and mass transfer characteristics. Furthermore, the study analysed the impact of key operating parameters such as airflow rate, water flow rate, and ambient air conditions on cooling effectiveness, and energy efficiency ratio (EER), with the goal of identifying the optimal operating configuration for improved system performance.

MATERIALS AND METHODS

The experimental measurements were conducted using a set of calibrated instruments to ensure accurate monitoring of thermal and operating parameters. Air temperature at the inlet and outlet of the evaporative cooler was measured using digital thermocouples (Type K) connected to a multi-channel data logger (e.g., model TM-747DU), with an accuracy of ±0.5°C. To account for high-humidity conditions, shielded temperature probes were employed to minimise measurement drift. Relative humidity of both ambient air and supply air was determined using a digital hygrometer (e.g., Testo 608-H1 or equivalent), with an accuracy of

±3% RH, and cross-validated using a sling psychrometer to improve reliability under varying moisture conditions. All sensors were calibrated prior to testing using standard reference conditions to reduce systematic error.

Measurement points were carefully defined to ensure consistency. The inlet air temperature and humidity were recorded at the external air intake of the system, while outlet conditions were measured directly at the discharge duct of the evaporative cooler. Additional measurements were taken within the test space (working area) to assess the cooling effect on the surrounding environment. Experiments were conducted under controlled conditions during midday hours (11:00 am to 1:00 pm) to ensure relatively stable ambient temperature and solar load.

Airflow rate was measured using an anemometer (e.g., hot-wire type, accuracy ±0.1 m/s) installed at the air outlet, and volumetric flow rate was calculated based on duct cross-sectional area, as shown in Figure 1. Water flow rate was monitored using a calibrated rotameter (range 0-3,000 l/hr, accuracy ±2%), allowing precise adjustment of circulation rates. Electrical power consumption of the system components, including pumps and compressor, was measured using a digital power meter (accuracy ±1%), enabling calculation of the EER.

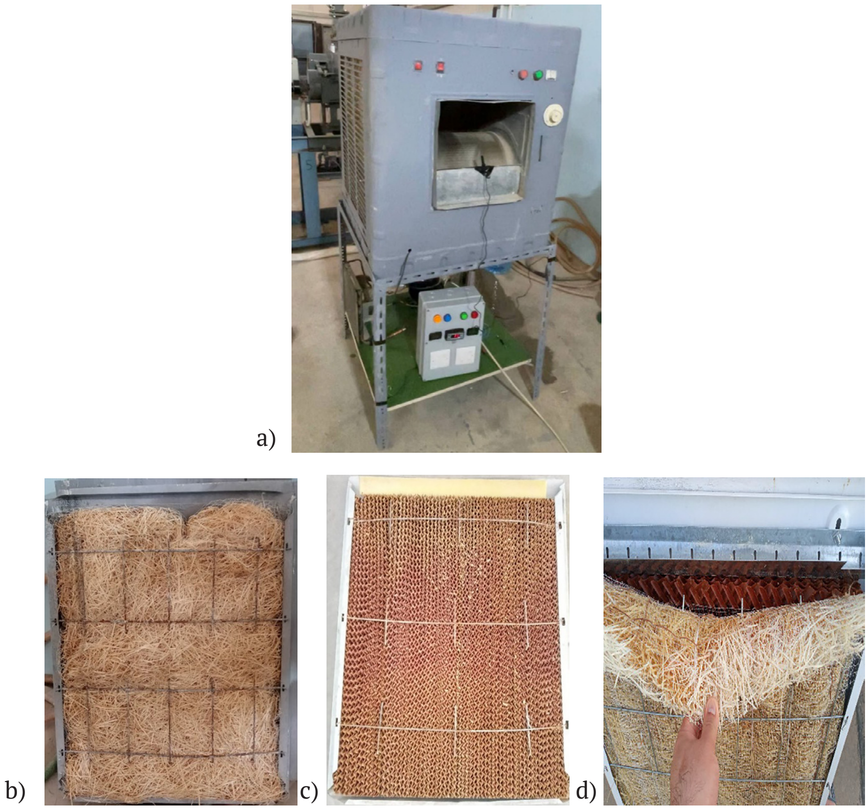

Figure 1. Types of evaporative cooler system pads
Note: a – evaporative cooler system; b – wood dust; c – cardboard padding; d – wood dust and cardboard padding
Source: developed by the authors

In addition to the measurement instrumentation, the experimental rig specifications and operating ranges were carefully defined. The evaporative air cooler was powered by a 1/3 HP (249 W) electric motor operating at 220 V and 50 Hz with a rotational speed of 1,425 RPM. The system was tested under three airflow rates of 0.566, 0.797, and 1.132 m^3/s. Water circulation was provided by two submersible pumps (40 W each), and the water flow rate was varied between 700 and 2,800 l/hr to evaluate its influence on cooling performance. The cooler body dimensions were 73 × 73 × 87 cm, while the outlet duct measured 34.5 × 21 × 19.5 cm. Furthermore, the hybrid cooling configuration incorporated a vapour-compression refrigeration unit equipped with a hermetic reciprocating compressor (1/3 HP, 280 W) using R600a refrigerant. The condenser fan power was 16 W, and the condenser dimensions were 35 × 26 × 3.5 cm. These system parameters were essential in defining the operational envelope of the experiments and ensuring reproducibility of results. To ensure data reliability, each experiment was repeated at least three times under identical operating conditions, and the average values were reported. Measurement uncertainty was estimated based on instrument accuracy and propagated through calculations, resulting in an overall uncertainty of approximately ±3 - 5% for efficiency and EER values. The repeatability of the results was confirmed by observing minimal deviation between repeated trials.

The performance of the evaporative cooling system was evaluated using fundamental heat and mass transfer relationships, which describe the thermodynamic behaviour of air-water interaction during the cooling process. The cooling efficiency (η) represents the ability of the system to reduce the dry-bulb temperature of the incoming air relative to the maximum possible cooling, defined by the wet-bulb temperature. It is expressed as the ratio of the actual temperature drop to the theoretical maximum temperature drop:

$$\eta = \frac{(T_1 - T_{\prime 2})}{(T_1 - T_2)} \times 100\%, \quad (1)$$

where T_1 – dry-bulb's temperature of air at entering (outdoor air temperature) in (°C); $T_{,2}$: dry-bulb's temperature of air at the exit (supply air temperature) in (°C); T_2 – wet-bulb's temperature of air at entering (outdoor air temperature) in (°C). Then the cooling capacity (Q_c) was calculated as:

$$Qc = Qa \times \rho \times Cp \times (T_1 - T_2), \quad (2)$$

where Q_a – air flow rate in (m³/s), Cp – specific air at constant pressure in (kJ/kg.K), ρ – air density (kg/ m³), T_1 – air temperature at the inlet (°C), T_2 – air temperature at the outlet (°C). The EER can be calculated from the following equation:

$$EER = \frac{Q_c}{P_E}, \quad (3)$$

where P_E – electrical power consumed in kW. Figure 2 represents the evaporative cooling process on a psychrometric chart, illustrating how air properties change during cooling and humidification. The horizontal axis (DBT) denotes the dry-bulb temperature, while the vertical axis indicates the specific humidity (humidity ratio). The curved boundary on the left corresponds to the saturation line (100% relative humidity), where air becomes fully saturated.

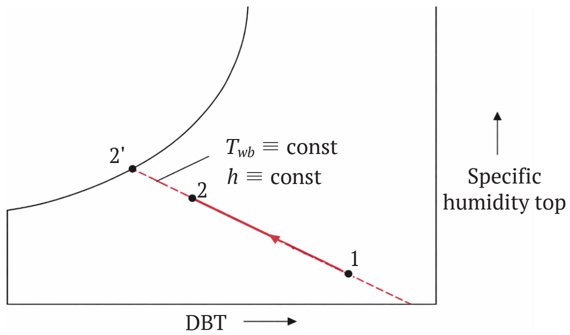

Figure 2. Demonstrates the evaporative cooler process
Source: developed by the authors

Point 1 represents the initial state of the incoming air, characterised by high dry-bulb temperature and low humidity (hot and dry conditions). As the air passes through the evaporative cooling system, it undergoes a transformation along the red line toward point 2. This process involves simultaneous cooling and humidification, where water evaporates into the air, reducing its temperature while increasing its moisture content. The key feature of this process is that it occurs approximately along a constant wet-bulb temperature (T_{wb} ≡ const.) and constant enthalpy (h ≡ const.) line, as indicated in the Figure 2. This reflects the thermodynamic principle that evaporative cooling is an adiabatic process, where the sensible heat of the air is converted into latent heat for water evaporation without external heat exchange. Point 2 represents the actual outlet air condition of the evaporative cooler. However, the process ideally could continue further toward point 2′, which lies closer to the saturation curve. This point represents the maximum achievable cooling limit, where the air approaches saturation and its temperature approaches the wet-bulb temperature. The dashed extension of the line indicates the ideal path, while the solid red line shows the real process, which deviates due to system inefficiencies such as incomplete evaporation, non-uniform wetting, and heat losses.

A simplified statistical assessment was performed to support the reliability of the experimental results. Based on the estimated overall measurement uncertainty (±3 - 5%), the standard deviation of the measured parameters was approximated, and the coefficient of variation was found to be within 4%, indicating good repeatability of the experiments. The maximum cooling efficiency of 89% under hybrid mode (P1&P2&C) falls within an uncertainty range of 85.4-92.6%, confirming the stability of the observed performance improvement. Similarly, the calculated EER values for different operating modes show limited dispersion, supporting the validity of the comparative analysis. Although this estimation provides an initial indication of data consistency, more rigorous statistical analysis based on extensive datasets is recommended for future work.

RESULTS AND DISCUSSION

The effect of the outside air temperature on actual energy consumed per ton of refrigeration is shown in Figure 3a. The results noted that the relationship is inverse with the stability of the airflow rate. These results showed that the increase in the air temperature leads to an increase in the cooling effect. While the energy consumed remains constant at the constant air flow rate, according to equation 3, the energy consumed per tonne of refrigeration is low. The test conditions were at airflow (0.566, 0.797, and 1.132 m³/sec), where the best airflow was selected (1.132 m³/sec) at water flow (1,400 l/hr). In this paper, three different types of packing were used in testing (wood dust, cardboard padding, wood dust and cardboard padding) shown in Figure 3b. It clears a relationship between efficiency and dry air inlet temperature, with airflow of 1.132 m³/s and water flow of 1,400 l/hr. The results showed that the increase of temperature of dry air inlet and lower relative humidity leads to a higher ability of the air stream to contain water vapour. In Figure 3b the mode (wood dust and cardboard padding) indicates that at an ambient temperature of 45°C, the better cooling efficiency was about 84.4%, and a temperature reduction was 65.6%. Figure 5 also indicates in mode (wood dust and cardboard padding) that increasing the ambient air temperature from 25°C to 45°C leads to an increase in the cooling efficiency from 70 to 84.4% and a reduction in the temperature from 58 to 65.6% respectively.

Figure 3c shows that the relationship adjusts the flow rate of circulating water in the system. As the amount of water sprayed in the humidified channels increases, the temperature of the air in the dry channels will continue to decrease to a certain extent. This decrease will be accompanied by an increase in the latent heat gain of the air as it passes through the humidified channels. This result is conditioned by a large amount of sprayed water, where the increase in the enthalpy of water vapour is higher than the decrease in the temperature of dry air of the wet connection. The moisture content of the air will rise after leaving the evaporative cooling system. It leads to an increase in the enthalpy of the ambient air and thus causes a decrease in cooling efficiency. Therefore, high rates of water quantities do not meet the requirement of a good and appropriate design for the cooling system used. The small amount of water requires a small pump to rotate water during the system operation. The result showed that in this case, the consuming electrical energy spent in the system was lower than in other cases, which means a more beneficial case from an economic standpoint. Ultimately, it increased the performance coefficient of the system. This feature is considered one of the benefits of the cooling system concerned with this research. Figure 3c showed that the amount of water flowed at the low rates until it reached a value of 2,100 l/hr, but continuing to increase the water flow above this amount caused a small increase in cooling efficiency sensible where the percentage did not exceed (1%) until it reached the peak value when the amount of water is increased to 2,450 l/hr, then the relationship began to reverse with the flow of water until it reached a maximum value of water flow 2,800 l/hr. On this basis, it can be considered the amount of 2,100 l/hr is the practical and appropriate value for the water flow rate in this case.

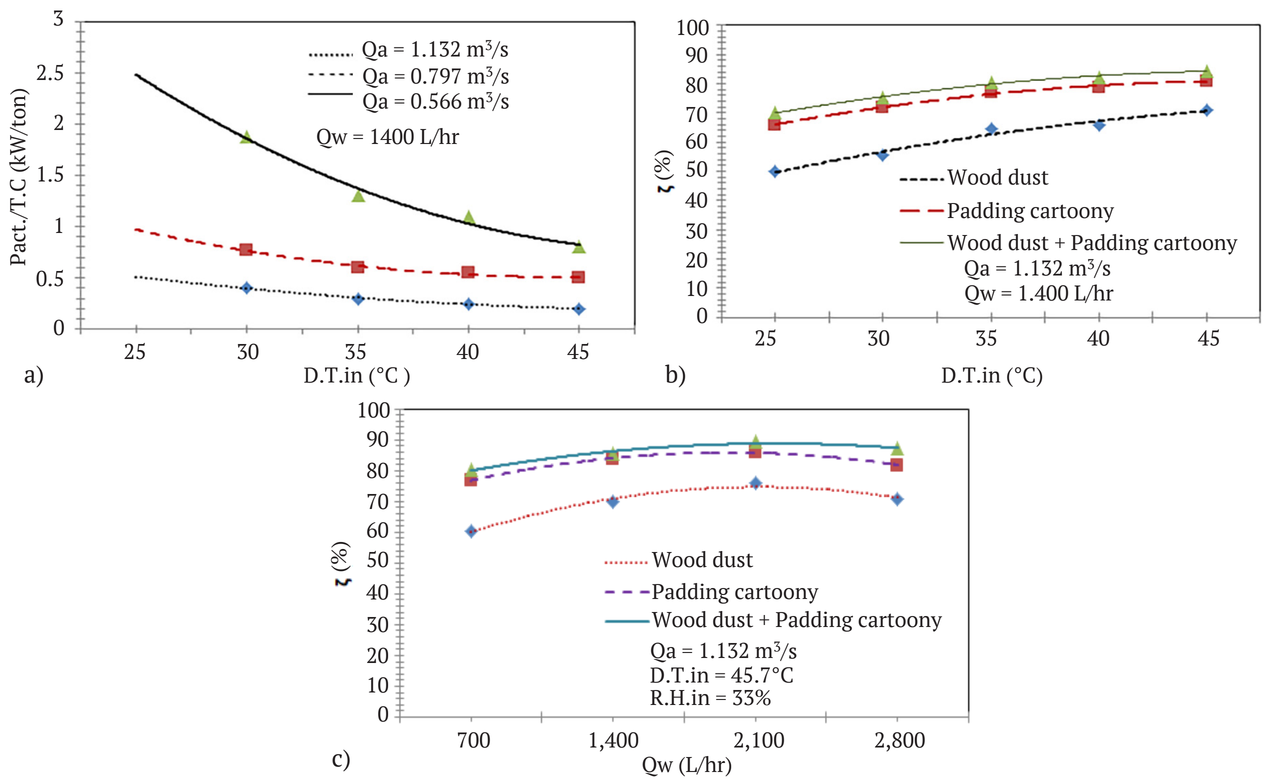

Figure 3. Influence of outdoor climatic and operating parameters on energy consumption and evaporative cooling efficiency

Note: a – effect of the temperature of the dry bulb outside air on real energy consumed per tonne of cooling; b – effect of the temperature of the dry bulb outside air on evaporative cooler efficiency; c – effect of the water mass flow-rate on evaporative cooler efficiency

Source: developed by the authors

Figure 4a showed the relation between the variation between the dry bulb inlet and outlet with time for varied paddings (wood dust, cardboard padding, and wood dust and cardboard padding). The results demonstrated that the temperature of the water and the air leaving the cooler was relatively decreased when using the second submersible pump, and the addition of the compression refrigeration cycle to the refrigerant reduced the air temperature of the coolant space. The use of a second submersible pump with the compression refrigeration cycle together led to a decrease in the space temperature. For mode (P1&P2&C), the comparison between Figure 4b, 4c showed that the reduction in the ambient air temperature is (9.7%), the reason for this reduction in temperature is conditioned by the delay in the passage of ambient air in the cardboard padding channels, and the occurrence of vortices of the incoming air, which leads to good contact of the incoming air with water droplets. The reduction ratio of the ambient air temperature may reach (16.3%) as Figure 5c compared with Figure 4a for mode (P1&P2&C). This reduction was because the padding channel contained (wood dust and cardboard padding) together.

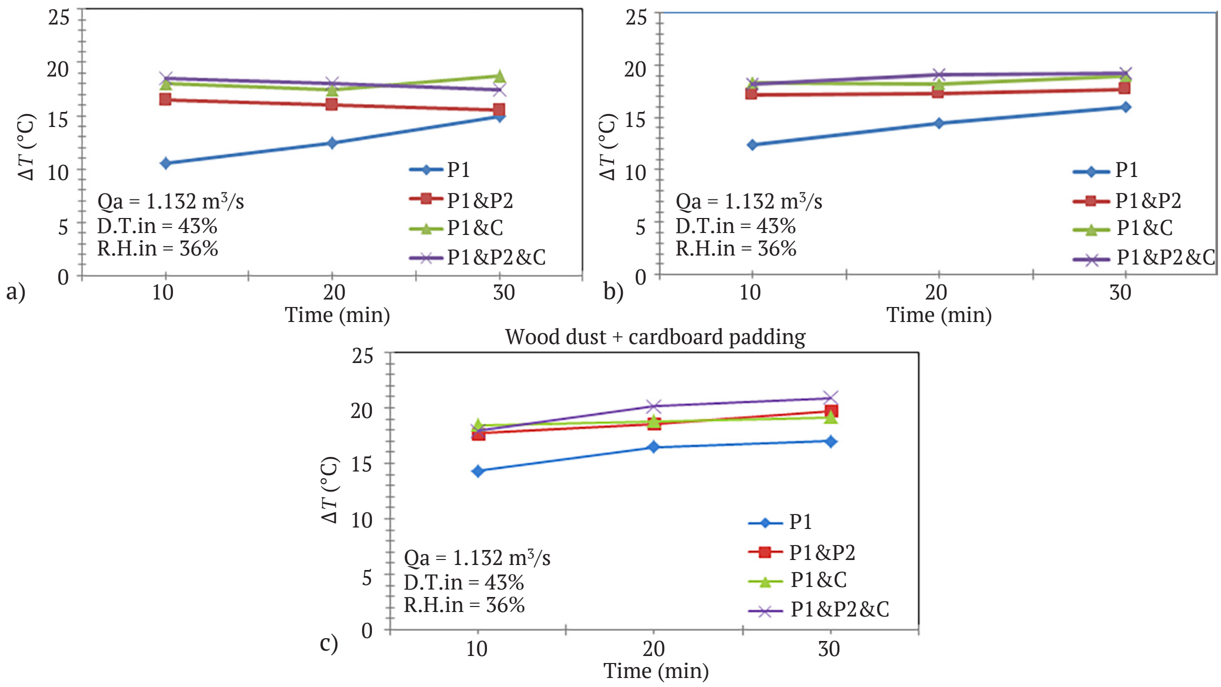

Figure 4. Time-dependent variation of dry-bulb temperature drop across evaporative pad materials (wood dust, cardboard, and their combination)

Note: a – relation between difference dry bulb inlet and outlet with time for wood dust paddings; b – relation between difference dry bulb inlet and outlet with time for cardboard padding; c – relation between difference dry bulb inlet and outlet with time for (wood dust and cardboard) paddings

Source: developed by the authors

Figure 5a, 5b shows the effect of the change in the padding types on the system on the evaporative cooler efficiency simultaneously. This change has been studied for three paddings (wood dust, cardboard padding, and wood dust and cardboard padding) with constant parameters air quantity (1.132 m^3/s), inlet dry bulb temperature at (47°C), and inlet relative humidity (27%). These Figures 5a, 5b show that the relationship is related directly to the constant air flow rate, whereby the increase in time increases efficiency. The reason for this relationship is conditioned by the evaporative quantity of basin water; it was carried out with the stability of the moisture content of the air approximately. In these Figures, there are different modes [only one pump (P1), only two pumps (P1&P2), one pump with refrigeration system (P1&C), and two pumps with refrigeration system (P1&P2&C)]. The temperature of the dry bulb outside air is almost constant during the test. The heat between entry and exit will increase because the susceptibility to heat and mass exchange of air and water increases when using wood dust and cardboard padding together with a constant air flow rate, and thus the efficiency increases. It also appears from Figure 6c that efficiency increases with the modes (P1&P2&C). The results show that maximum efficiency is (89%) at mode (P1&P2&C) with the presence of wood dust and cardboard padding together at the surfaces of the heat exchanger from the side of the humidified channels. Figure 5d depicted the relationship between the EER with the difference between dry bulb inlet and outlet for (wood dust and cardboard) paddings. Figure 6d showed that the EER is higher for evaporate coolers only, and it reaches 15 and decreases with the decrease in the variation between the dry bulb inlet and outlet. In addition, the EER is the lowest possible for (P1&C) mode.

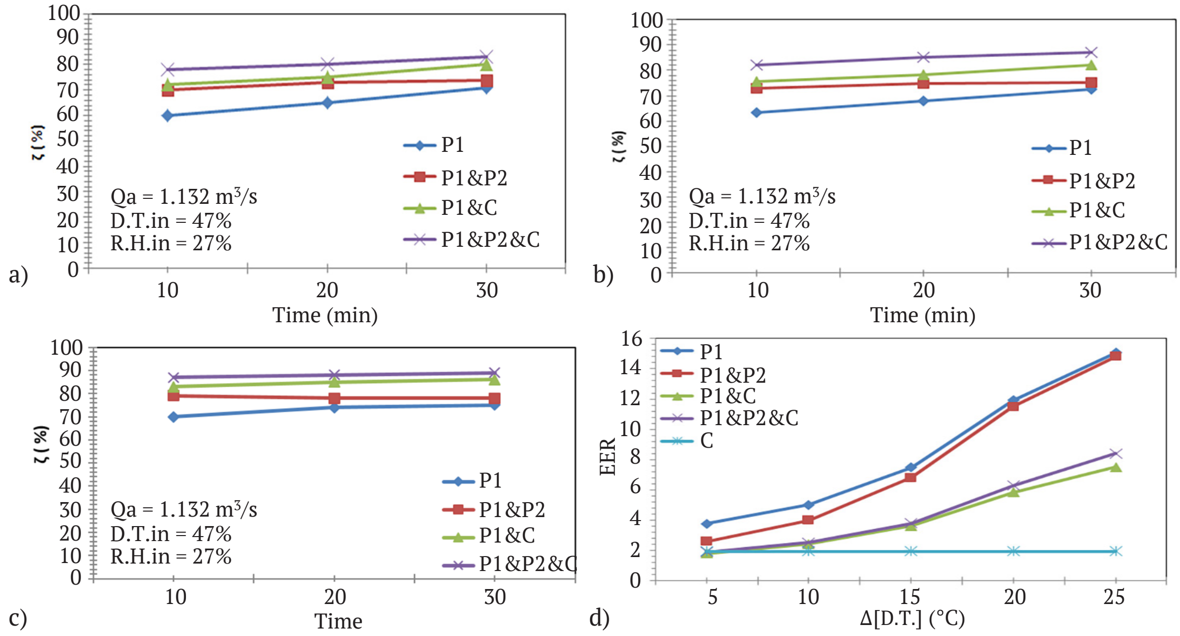

Figure 5. Time-dependent variation of evaporative cooler efficiency and EER for different pad materials (wood dust, cardboard, and their combination)

Note: a – relation between evaporative cooler efficiency with time for wood dust paddings; b – relation between evaporative cooler efficiency with time for (wood dust and cardboard) paddings; c – relation between evaporative cooler efficiency with time for cardboard padding; d – relation between EER with different dry bulb inlet and outlet for (wood dust and cardboard) paddings

Source: developed by the authors

The proposed (P1&P2&C) system is located slightly higher than (P1&C) mode and then from compression refrigeration mode (C). This means that the proposed system consumes less energy than compression cooling for the same cooling effect. Ultimately, the proposed mode (P1&P2&C) gives the best cooling effect when compared with other modes this results coincides with studies by S. Kumar *et al*. (2021), H. Sonawan *et al*. (2022), and S. Rasheed *et al*. (2025b). The analysis revealed that the efficiency and energy performance of the evaporative cooler depend significantly on both the temperature and humidity of the outside air and the design and type of the pad. As the dry-bulb temperature increases, the cooling capacity of the system and the efficiency of evaporation increase, particularly for combined fillers made of wood dust and cardboard. It was also found that optimising water flow is critical, as excessive flow does not improve efficiency but increases energy consumption. The combined configuration provides the highest efficiency and the best cooling performance compared to other operating modes. The results obtained confirm the feasibility of using hybrid systems to improve the energy efficiency of cooling.

CONCLUSIONS

By means of structural and operational changes, this study offered an experimental investigation aimed at improving the performance and energy efficiency of an evaporative cooling system. Under various operating conditions including: variations in airflow rate, water flow rate, and cooling pad materials; a hybrid cooling arrangement including an evaporative cooler with a vapour-compression refrigeration system was created and tested. The findings showed that operating conditions and design elements have a great impact on system performance. The ideal airflow rate was found to be 1.132 m^3/s with a related water flow rate of 1,400 l/hr, therefore providing a good compromise between energy use and cooling efficiency. Among the examined pad materials, wood dust and cardboard padding used together showed best thermal performance with a maximum cooling effectiveness of 89% under hybrid operating mode (P1&P2&C). Furthermore, increasing ambient air temperature inside the range under examination improved cooling efficiency as a result of increased evaporation capability. The combination of a second submersible pump and the integration of the refrigeration cycle helped to clearly lower outlet air temperature and generally improve the system. Moreover, the suggested hybrid system showed a much better EER than the traditional compression cooling system, therefore, validating its capacity to lower electricity consumption while keeping excellent cooling performance. The results show throughout that evaporative cooling efficiency may be greatly enhanced by careful selection of pad materials, water flow rate, and system arrangement. Particularly in hot and dry locations, the suggested hybrid system provides a sensible and energy-efficient answer for air conditioning applications.

Further research should focus on optimising padding material structure and composition (including alternative porous and nanostructured media), investigating advanced water distribution techniques to enhance evaporation uniformity, and integrating intelligent control systems for real-time optimisation under varying climatic conditions. In addition, more detailed thermodynamic and economic analyses are required to evaluate long-term performance, water consumption, and system scalability, particularly for large-scale and industrial applications in different climatic regions.

ACKNOWLEDGEMENTS

None.

FUNDING

None.

CONFLICT OF INTEREST

None.

REFERENCES

[1] Hasan, R.A., Abdulqader, M.A., Alias, A.B., Hussein, N.A., Ahmed, O.K., Keighobadi, J., Saleh, A.M., Hamad, Z.K., Saleh, N.M., & Mahmood, M.K. (2025). Advancements and performance of evaporative cooling technologies: Applications, benefits, and future prospects. *KHWARIZMIA*, 2025, 30-41. doi: 10.70470/KHWARIZMIA/2025/004.

[2] Kumar, S., Salins, S.S., Reddy, S.V.K., & Nair, P.S. (2021). Comparative performance analysis of a static & dynamic evaporative cooling pads for varied climatic conditions. *Energy*, 233, article number 121136. doi: 10.1016/j.energy.2021.121136.

[3] Rasheed, S., Ali, M., Ali, H., Sheikh, N.A., & Li, G. (2025a). Design evolution of indirect evaporative air-cooling system through multiple configurations for the enhancement of heat and mass transfer mechanism. *International Communications in Heat and Mass Transfer*, 160, article number 108393. doi: 10.1016/j.icheatmasstransfer.2024.108393.

[4] Rasheed, S., Ali, M., Ali, H., Sheikh, N.A., Imran, M., Xie, X., & Li, G. (2025b). Enhanced thermal efficiency in crossflow evaporative cooling systems: A comparative study of materials and flow patterns. *International Communications in Heat and Mass Transfer*, 167, article number 109252. doi: 10.1016/j.icheatmasstransfer.2025.109252.

[5] Romero-Lara, M.J., Comino, F., & Ruiz de Adana, M. (2023). Seasonal energy efficiency ratio of regenerative indirect evaporative coolers-simplified calculation method. *Applied Thermal Engineering*, 220, article number 119710. doi: 10.1016/j.applthermaleng.2022.119710.

[6] Salman, A.H., Jasim, J.A., Aljuboori, M.K.A., & Zaidan, A.A. (2024). Efficiency analysis of a two-stage evaporative cooling system with sustainable water pad. *International Journal of Heat and Technology*, 42(2), 679-687. doi: 10.18280/ijht.420235.

[7] Santos, A.F., Gaspar, P.D., & Souza, H.J.L. (2021). Measuring the energy efficiency of evaporative systems through a new Index-EvaCOP. *Energies*, 14(9), article number 2689. doi: 10.3390/en14092689.

[8] Sonawan, H., Sofia, E., & Ramadhan, A. (2022). Assessment of direct evaporative cooler performance with a cooling pad made from banana midrib and ramie fiber. *Smart and Sustainable Built Environment*, 11(3), 469-482. doi: 10.1108/SASBE-06-2020-0078.

Фуркан Хайдер Мохамед Алі
Магістр
Технічний інженерний коледж Кіркук
Північний технічний університет
36001, м. Кіркук, Ірак
https://orcid.org/0009-0004-5491-3224

Захраа Хайдер Мохамед Алі
Магістр
Кіркукський політехнічний коледж
Північний технічний університет
36001, м. Кіркук, Ірак
https://orcid.org/0009-0007-7034-5230

Мустафа Наозад Тайфор
Магістр
Центр досліджень відновлювальної енергетики
Північний технічний університет
36001, м. Кіркук, Ірак
https://orcid.org/0000-0001-7146-1160

Хусейн Хайдер Мохамед Алі
Доктор філософії
Технічний інженерний коледж Кіркук
Північний технічний університет
36001, м. Кіркук, Ірак
https://orcid.org/0000-0003-4264-400X

Експериментальне дослідження окремих параметрів підвищення ефективності випарного охолоджувача: технічні нотатки

Анотація. Як альтернатива традиційним системам кондиціонування повітря на основі парокомпресійного циклу, які суттєво збільшують пікове електричне навантаження та енергоспоживання, у цьому дослідженні розглянуто методи підвищення продуктивності та енергоефективності випарних систем охолодження. Було експериментально розроблено та оцінено гібридну дворежимну систему охолодження, що поєднує парокомпресійну холодильну установку з випарним охолоджувачем. Дослідження зосереджено на ключових модифікаціях, зокрема заміні традиційних наповнювачів із деревного пилу на картонний наповнювальний матеріал, використанні допоміжного занурювального насоса для підвищення циркуляції води, а також комбінованій роботі обох типів наповнювачів. Експериментальні результати продемонстрували суттєве покращення роботи системи внаслідок цих змін. Зокрема, гібридна система з комбінованим середовищем із деревного пилу та картонного наповнювача досягла найвищої ефективності охолодження – 89 %, що свідчить про значне покращення процесів тепло- та масообміну. Збільшення витрати води додатково сприяло кращому зволоженню наповнювачів і підвищенню ефективності випарного охолодження. З точки зору енергетичних характеристик, гібридна система продемонструвала коефіцієнт енергоефективності (EER) на рівні 8,3, що значно перевищує показник автономної парокомпресійної системи (EER = 1,95). Окрім того, незалежна випарна система досягла максимального EER 14,8 при ефективності охолодження 71 %, що підтверджує її високий потенціал енергозбереження за відповідних умов експлуатації. Результати також показали, що оптимізація характеристик наповнювачів і розподілу води відіграє ключову роль у підвищенні ефективності охолодження при мінімізації енергоспоживання. Отримані дані підтверджують, що інтеграція випарного охолодження з традиційними системами, разом із належним вибором матеріалів і вдосконаленням гідравлічних параметрів, дозволяє істотно зменшити загальне енергоспоживання, зберігаючи належний рівень теплового комфорту. З практичної точки зору, запропонована гібридна система є економічно вигідним, енергоефективним і сталим рішенням для жарких і сухих кліматичних умов, що передбачає використання доступних місцевих матеріалів і простих модифікацій для зниження енергоспоживання та викидів, а також сприяє розвитку перспективних технологій охолодження

Ключові слова: гібридне кондиціонування повітря; термодинамічний аналіз; деревний пил; картонний наповнювач; енергоефективність

MACHINERY & ENERGETICS

Scientific Journal

Volume 17, No. 1. 2026

Founded in 2010. Published four times per year

Managing editor:
N. Shevchenko

Signed for print of February 26, 2026.
Format 60*84/8
Conventional printed pages 9.7
Circulation 100 copies

Publisher's address:
National University of Life and Environmental Sciences of Ukraine
03041, 15 Heroiv Oborony Str., Kyiv, Ukraine
Tel.: +38(044)-258-42-63
E-mail: me@technicalscience.com.ua
https://technicalscience.com.ua/en

ТЕХНІКА ТА ЕНЕРГЕТИКА

Науковий журнал

Том 17, № 1, 2026

Заснований у 2010 р. Виходить чотири рази на рік

Відповідальний редактор:
Н. Шевченко

Підписано до друку 26 лютого 2026 р.
Формат 60*84/8
Умов. друк. арк. 9,7
Наклад 100 прим.

Адреса видавництва:
Національний університет біоресурсів і природокористування України
03041, вул. Героїв Оборони, 15, м. Київ, Україна
Тел.: +38(044)-258-42-63
E-mail: me@technicalscience.com.ua
https://technicalscience.com.ua/uk